Effect of Defects on High-Temperature Mechanical Properties of Welded Water Walls

by

Suvan Dev Choudhury

A thesis submitted in partial fulfillment of the requirements for the degree of

Doctor of Philosophy

in

Materials Engineering

Department of Chemical and Materials Engineering
University of Alberta

Abstract

Water walls play a crucial role in the operation of refineries, industrial plants, and power plants. However, the repeated start-ups and shutdowns of boilers lead to in-phase thermo-mechanical fatigue failure of the water walls with fatigue cracks often initiating from pre-existing weld defects. There is a lack of comprehensive research on the fatigue failure mechanisms specific to water walls. Most existing studies primarily focus on failure modes related to microstructural degradation and oxide formation, not on fatigue crack propagation under harsh loading conditions. By investigating the fatigue failure mechanism, this thesis sheds light on the formation and progression of blow holes, which is a critical failure mode for the membranes of water walls.

Subjecting defect-containing water walls to hydrostatic preloading at 1.5 times the maximum allowable working pressure (MAWP) results in localized plastic deformation near the pre-existing weld defects. This leads to significant strain hardening and strain aging effects, altering the mechanical properties of the welded membrane specimens. To mitigate such changes, it is recommended to maintain the hydrostatic pressure at approximately 110% of the MAWP to minimize the occurrence of significant mechanical property alterations caused by strain hardening and strain aging at stress concentration points within defect-containing water wall membranes.

An extensive three-dimensional characterization of pre-existing weld defects in welded membrane specimens has been conducted. The defects are analyzed based on their size, shape, and position within the specimens. Parameters such as sphericity, circularity, and aspect ratio are effective in quantifying defect sharpness. Sharper defects significantly reduce fatigue life compared to rounder defects. Stress intensity

factors (SIF) are calculated at each defect location, pointing at potential fatigue crack initiation sites. In the absence of defects, the weld fusion zone is found to be the most susceptible location for fatigue crack initiation. This susceptibility is attributed to the coarse dendritic microstructure in the weld fusion zone, which is less ductile than the base material. The coarse microstructure is prone to the formation of micro-cracks, contributing to the initiation of primary fatigue cracks.

Finite element modeling is conducted to quantify the fatigue damage and crack propagation and to establish crucial parameters describing experimental results. The fatigue damage parameters are extracted from experimental results to simulate the accumulation and progression of damage. These crack propagation parameters measure blowhole formation, tracking crack initiation and propagation. The cracks are found to have originated from fusion defects, causing membrane disconnection which may have caused localized thermal hotspots and membrane rupture, leaving molten slag residues on the airside of water walls.

Preface

The materials included in this thesis are the result of research projects conducted under the supervision of Dr. Leijun Li and funded by the Mitacs Accelerate Program. Some of the findings have been published in peer-reviewed journals.

Chapter 4 of this work has been published as Dev Choudhury, S., Saini, S., Lyu, Z., Kopparthi, R., Tervonen, Z., Li, L., "Effects of hydrostatic preload on strain hardening and strain aging of boiler tubes", International Journal of Pressure Vessels and Piping, 200 (2022) 104806.

Chapter 5 of this work has been published as Dev Choudhury, S., Li, L., Saini, S., Khan, W., Kopparthi, R., Lyu, Z., "3D characterization of internal defects for fatigue performance of welded SA192 steel water walls", International Journal of Pressure Vessels and Piping 202 (2023) 104922.

Chapter 6 of this work has been published as Dev Choudhury, S., Khan, W.N., Lyu, Z., Li, L., "Failure Analysis of Blowholes in Welded Boiler Water Walls", Engineering Failure Analysis (2023).

Chapter 6 of this work is to be submitted as Dev Choudhury, S., Khan, W.N., Li, L., "Fatigue Damage Investigations on Welded Boiler Water Walls" to International Journal of Fatigue.

Acknowledgements

I am deeply grateful and would like to express my sincere appreciation to my supervisor, Dr. Leijun Li, for his invaluable guidance and unwavering support throughout the completion of this thesis. Over the past four years, Dr. Li's belief in my abilities has been a constant source of motivation. His unwavering support and encouragement have been instrumental in overcoming challenges and achieving significant milestones in my research. I am truly thankful for his mentorship, which has not only shaped my academic and professional growth but has also fostered a profound passion for the field. This thesis would not have been possible without his expertise, guidance, and unwavering faith in me.

I am deeply grateful and would like to express my heartfelt appreciation to Dr. Hani Henien, Dr. Douglas Ivey, Dr. Weixing Chen, and Dr. Hao Zhang for their unwavering support in providing lab equipment and engaging in valuable discussions regarding my coursework, research, and career development. Their guidance and expertise have been invaluable throughout my academic journey. I would also like to extend my gratitude to the NanoFAB staff, particularly Dr. Shihong Xu and Mr. Peng Li, for their technical assistance, which has greatly contributed to the success of my research endeavours. Their dedication and expertise have been crucial in conducting experiments and obtaining meaningful results.

I would like to express my sincere thanks to my esteemed colleagues in our group: Dr. Nitin Saini, Dr. Waris Nawaz Khan, Dr. Nitin Sharma, Mr. Zhe Lyu, Mr. Ravikiran Kopparthi, Mr. Jason Li, and Mr. Zachary Tervonen. They have not only been my colleagues but also my valuable collaborators and friends. I am grateful for

their contributions and the enriching experiences we have shared together.

I am truly grateful for the support and friendship I received from my dear friends, Ms. Anantha Srujana Ealeswarapu, Mr. Adil Karimov, and Mr. Kapil Gangwar. The memories we created during our time together in Edmonton are cherished and hold a special place in my heart. Their presence and encouragement have made my journey more enjoyable and meaningful.

Lastly, I want to express my utmost appreciation to my parents Mr. Ashok Kr. Dev Choudhury, and Mrs. Dipannita Dev Choudhury and my sister Ms. Niharika Dev Choudhury for their unconditional love and unwavering support.

Table of Contents

1 Introduction **1**

1.1 Research gaps 2
1.2 Objectives of the thesis 3
1.3 Outline of the thesis 3

2 Literature Review **6**

2.1 Water walls and classification 6
2.2 Failures in water walls 8
2.3 Hydrostatic preloading 10
2.4 Fatigue failure in water walls 11
2.5 Fatigue failure 13
2.5.1 Low cycle fatigue failure 14
2.5.2 Thermo-mechanical fatigue 16
2.5.3 Mechanical metallurgy of fatigue failure 19
2.5.4 Stress Intensity Factor 19
2.5.5 Notch effect on the fatigue life 21
2.6 Fatigue crack propagation models 24
2.6.1 Paris model 25
2.6.2 Walker model 26
2.6.3 Forman model 27
2.6.4 Elber model 27
2.7 Numerical methods for fatigue crack growth modeling 28
2.8 Analysis of internal defects 31

3 Materials and Methodology **33**

3.1 Materials 33
3.2 Sampling and Characterization 33
3.2.1 Specimen Extraction 34
3.2.2 Non-Destructive Testing 35

3.2.3 Tensile Testing . . . 35
3.2.4 Fatigue Testing . . . 38
3.2.5 Hardness Testing . . . 39
3.2.6 Optical Microscopy . . . 40
3.2.7 Scanning Electron Microscopy (SEM) . . . 40
3.2.8 Energy Dispersive X-ray Spectroscopy (EDS) . . . 40
3.2.9 Electron Backscatter Diffraction (EBSD) . . . 41
3.3 Finite Element Analysis (FEA) . . . 41
3.4 Summary . . . 42

4 Effects of hydrostatic preload on strain hardening and strain aging of water walls 43
4.1 Introductiion . . . 43
4.2 Experimental and Simulation Methodology . . . 44
4.3 Results . . . 47
4.4 Discussion . . . 55
4.5 Summary . . . 67

5 3D characterization of internal defects for fatigue performance of welded SA192 steel water walls 69
5.1 Introduction . . . 69
5.2 Experimental and Analysis Methodology . . . 70
5.3 Results . . . 76
5.4 Discussion . . . 88
5.5 Summary . . . 104

6 Low cycle fatigue damage and crack propagation simulation of welded membranes 106
6.1 Introduction . . . 106
6.2 Theoretical background . . . 107
6.2.1 Nonlinear kinematic hardening . . . 107
6.2.2 Damage initiation . . . 108
6.2.3 Damage evolution . . . 110
6.2.4 Extended finite element formulation . . . 112
6.3 Finite element results and discussion . . . 114
6.3.1 Geometry of FE models . . . 114
6.3.2 Cyclic softening and stabilization parameters . . . 115
6.3.3 Damage initiation and evolution parameters . . . 116

6.3.4 Fatigue damage results 120
6.3.5 Fatigue damage results for specimen with lack of fusion defect 124
6.3.6 Fatigue crack propagation for water wall section with lack of fusion defect 127
6.3.7 Failure analysis of blowholes in water walls 129
6.4 Summary 135

7 Conclusion and Future work **136**
7.1 Conclusion 136
7.2 Future work 138

Bibliography **140**

Appendix A: Fatigue damage and crack propagation simulation **154**

List of Tables

3.1 Chemical composition of ASME SA-192 steel (wt %) 33

4.1 Test matrix to study the effects of preload on strain hardening and strain aging 48
4.2 Tensile properties of base material and welded membrane at room temperature 51
4.3 Mechanical properties of welded membrane specimens. 52
4.4 Mechanical properties of smooth and notched water wall specimens. . 63

5.1 Mechanical properties of water walls tested at 300°C. 80
5.2 Fatigue test matrix and results 85
5.3 Various defect parameters calculated from XCT scans 97

6.1 Chaboche nonlinear kinematic hardening model parameters of welded membranes 116
6.2 Fatigue damage value from experimental data 119
6.3 Fatigue damage parameters 120
6.4 Paris constants used in water wall section 127

List of Figures

2.1 Schematic of water walls different water wall construction (a) Tube and Tile Water Wall, (b) Tangent Tube Water Wall, (c) Studded Tube Water Wall, and (d) Membrane Water Wall [1] 9
2.2 Hysteresis loop for constant strain cycling [37] 15
2.3 Phase orientation of Thermo Mechanical Fatigue [40] 18
2.4 Three modes of cracking that can be applied to a crack [50] 21
2.5 Crack initiation from an inclusion [54] 23
2.6 Schematic representation of crack growth curve [55] 24

3.1 Schematic of water walls with the location of test specimens (all dimensions are in mm) 34
3.2 Dimensions of the notched tensile base material specimens extracted from water walls (all dimensions are in mm) 36
3.3 Dimensions of round tensile welded membrane specimens (all dimensions are in mm) 36
3.4 (a) Section of water walls showing extraction locations of round tensile specimens for welded membrane samples and (b) Macrograph of extraction site for welded membrane specimens 37
3.5 (a) Dimensions of fatigue specimen extracted from water walls (all dimensions are in mm) and (b) An image showing the fatigue specimen 39

4.1 Ludwik–Hollomon hardening law fitted to measured true stress-strain curve of the base material 44
4.2 Cross-section of water wall welded membrane tensile specimen. 46
4.3 Water wall base material specimen and welded membrane specimen tested at room temperature 49
4.4 Stress-strain curves treated according to the rule of mixtures. The base material and weld material stress-strain curves served as input to the finite element simulation as material properties 50
4.5 Mesh study for von Mises stress in water wall section 52

4.6 (a) Equivalent von Mises stress with 150% of maximum allowable working pressure and (b) Equivalent von Mises stress with 100% of maximum allowable working pressure 53
4.7 Stress-strain curves of the welded membrane specimens 54
4.8 Mesh study for plastic strain in notched water wall specimen 56
4.9 (a) Ansys simulation of notched water wall sample with 95 MPa room temperature preload. Maximum 1.7% plastic strain was generated. Equivalent plastic strain at the (X-Z) cross-section, (b) equivalent plastic strain at the (Y-Z) cross-section at the notch, (c) Ansys simulation of notched water wall sample with 53 MPa room temperature preload. Maximum 0.05% plastic strain was generated. Equivalent plastic strain at the (X-Z) cross-section and (d) equivalent plastic strain at the (Y-Z) cross-section at the notch. 57
4.10 (a) Optical microstructure of 95 MPa preloaded notched water wall specimen near the notch, (b) near the center, (c) optical microstructure of 53 MPa preloaded notched water wall specimen near the notch and (d) near the center. 58
4.11 Grain orientation spread and grain boundary map of 95 MPa preloaded specimen with misorientation distribution of the EBSD images, (a) near the notch and (b) at the center of specimen cross-section. 59
4.12 (a) Stress-strain curves of the smooth water wall specimens and (b) stress-strain curves of the notched water wall specimens 62
4.13 Mesh study for plastic strain in weld membrane specimen 64
4.14 (a) Welded membrane sample with defects (Sample WC-95 PL #1) and (b) model of the sample with defects at 10° relative to loading direction 65
4.15 Strain distribution in water wall welded membrane specimen (Sample WC-95 PL #1) loaded to 95 MPa at room temperature. A maximum 2.8% plastic strain was generated near the weld defect. 66

5.1 Operating temperature and steam pressure of water walls over a span of 2 years 71
5.2 Mesh study for plastic strain in Z-direction 73
5.3 Stress-strain curves for Tube Base, Membrane, and Weld. The weld and tube base properties served as input parameters for finite element simulation 77

5.4 Coefficient of thermal expansion as a function of temperature for weld and base metals 78
5.5 ANSYS simulation of water walls: (a) equivalent stress, and (b) total strain in Z-direction (i.e., tube axial direction) 79
5.6 Cross-sectional macrographs of fatigue test specimens: (a) and (b): left and right ends of Specimen A; (c) and (d) left and right ends of Specimen B; (e) and (f) left and right ends of Specimen C; (g) and (h) left and right ends of Specimen D; (i) and (j): left and right ends of Specimen E; (k) and (l): left and right ends of Specimen F; (m) and (n): left and right ends of Specimen G; (o) and (p): left and right ends of Specimen H 81
5.7 X-ray computed tomography scans for (a) Specimen A, (b) Specimen E, (c) Specimen B, and (d) Specimen F 83
5.8 X-ray computed tomography scans for (a) Specimen G, and (b) Specimen H 84
5.9 Maximum and minimum stresses vs number of cycles to failure curves for fatigue tested specimens at 0.4% peak strain 86
5.10 Maximum and minimum stresses vs number of cycles to failure curves for fatigue tested specimens at 0.7% peak strain 87
5.11 Fractography of specimens with defects: (a) the entire fracture surface Specimen A (b) fatigue striations in Specimen A, (c) the entire fracture surface Specimen B, and (d) fatigue striations in Specimen B 89
5.12 Fractography of defect-free specimens: (a) the entire fracture surface Specimen C (b) fatigue striations in Specimen C, (c) the entire fracture surface Specimen D, and (d) fatigue striations in Specimen D 90
5.13 Fractography of specimens with defects: (a) the entire fracture surface Specimen E (b) fatigue striations in Specimen E, (c) the entire fracture surface Specimen F, and (d) fatigue striations in Specimen F 91
5.14 Fractography of defect-free specimens: (a) the entire fracture surface Specimen G (b) fatigue striations in Specimen G, (c) the entire fracture surface Specimen H, and (d) fatigue striations in Specimen H 92
5.15 (a) macrograph of Specimen C shows fatigue crack initiation, (b) hardness map of Specimen C, and (c) macrograph of Specimen D 93
5.16 Distribution of defect size throughout the gauge length; (a) for Specimen A, (b) for Specimen B, and (c) for Specimen E 95
5.17 Mean excess (ME) plot for (a) Specimen A, (b) Specimen B, and (c) Specimen E 99

5.18 Dimensional heat map from XCT scans, showing height and width of defects: (a) and (b) are for Specimen A, (c) and (d) are for Specimen B, and (e) and (f) are for Specimen E 101
5.19 The shape parameters of defects: (a) aspect ratio vs. sphericity, and (b) aspect ratio vs. circularity. 102

6.1 Estimation of N_o from max. and min. stress versus cycle number . . 110
6.2 FE model for damage initiation and evolution in ABAQUS 115
6.3 FE model for fatigue crack propagation in ABAQUS 116
6.4 Experimental and simulation comparison of max-min stress evolution (a) max-min stress evolution under $\epsilon = 0.4\%$, (b) max-min stress evolution under $\epsilon = 0.6\%$, and (c) max-min stress evolution under $\epsilon = 0.7\%$ 117
6.5 Calculation of damage initiation parameter at 300°C 119
6.6 Calculation of damage evolution parameter at 300°C 120
6.7 Experimental data and FE model's prediction of max. and min. stress versus cycle number for (a) $\Delta\epsilon_t = 0.4\%$, (b) $\Delta\epsilon_t = 0.6\%$, and (c) $\Delta\epsilon_t = 0.7\%$ 122
6.8 Fatigue life predictions of the welded membrane specimens 123
6.9 X-ray tomography results for a specimen with lack of fusion slit . . . 124
6.10 FE simulation of a welded specimen with lack of fusion slit 125
6.11 Experimental data and FE model's prediction of max. and min. stress versus cycle number for specimen with lack of fusion slit 126
6.12 FE model with different crack locations: (a) at the weld toe region, (b) at the lack of fusion defect 128
6.13 Crack propagation simulation when the crack is placed at weld root: (a) crack propagation status at t = 0 cycles, (b) crack propagation status at t = 117 cycles, (c) crack propagation status at t = 180 cycles, and (d) crack propagation status at t = 182 cycles. 130
6.14 Crack propagation simulation when the crack is placed at lack of fusion slit: (a) crack propagation status at t = 0 cycles, (b) crack propagation status at t = 99 cycles, (c) crack propagation status at t = 112 cycles, and (d) crack propagation status at t = 129 cycles. 131
6.15 Mesh study for temperature in water wall section 132
6.16 (a) Fireside of the water wall section, and (b) Airside of the water wall section 133

6.17 (a) FE simulation of temperature gradient in the presence of lack of fusion defects and fatigue cracks, (b) FE simulation of temperature gradient without the presence of lack of fusion defects and fatigue cracks 133
6.18 (a) Blow hole from the fireside, (b) Polished section of the blow hole, (c) macrostructure at the right edge of the blow hole, and (d) macrostructure at the left edge of the blow hole. 134

List of Symbols

ϵ_a	Total Strain Amplitude (mm/mm)
ϵ_b	True Strain (mm/mm)
ρ	Density (kg/m^3)
σ_b	True Stress (MPa)
$\sigma_f^{'}$	Fatigue Strength Coefficient
σ_{ij}	Cauchy Stress Tensor (Pa)
σ_{max}	Maximum Stress (MPa)
A_b	Cross-sectional area of Base Metal (m^2)
A_w	Cross-sectional area of Weld (m^2)
b	Fatigue Strength Exponent
E_b	Young's Modulus of Base Metal (GPa)
E_w	Young's Modulus of Weld (GPa)
$E_{composite}$	Young's Modulus of Composite (GPa)
K	Strength Coefficient
K_f	Fatigue Strength Reduction Factor
K_I	Stress Intensity Factor in Mode I Cracking $(MPa.m^{1/2})$
n	Strain Hardening Exponent
$2a$	Minor Axis of Ellipse (mm)
$2c$	Major Axis of Ellipse (mm)
$2N_f$	Number of Strain Reversals
α	Back Stress Tensor (Pa)
α^{dev}	Deviatoric Part of Stress Tensor (Pa)

$\bar{\epsilon}$	Equivalent Plastic Strain (mm/mm)
$\bar{\sigma}$	Equivalent Stress (MPa)
β	Inclination Angle of Defect $(^{\circ})$
$\Delta\epsilon_p$	Plastic Strain Amplitude (mm/mm)
ΔK_I	Stress Intensity Factor Range $(MPa.m^{1/2})$
ΔW_o	Accumulation of Inelastic Hysteresis Energy per Cycle (Mj/m^3)
$\Delta\sigma$	Stress Range (MPa)
$\epsilon_f^{'}$	Fatigue Ductility Coefficient
γ	Shape Parameter
λ	Slip Distance (m)
ϕ	Elliptical Integral
σ	Scale Parameter
σ^o	Radius of Yield Surface (MPa)
A_d	Defect Area (mm^2)
a_i	Acceleration in i-direction (m/s^2)
b_i	Body Force in i-direction (N)
b_i^k	Nodal Enriched Degree of Freedom Vector
c	Fatigue Ductility Exponent
E	Young's Modulus (GPa)
F	Total Load (kN)
$F_k(x)$	Elastic Asymptotic Crack-Tip Function
$H(x)$	Heaviside Function
L	Characteristic Length of Elements (m)
$N(t)$	Number of Solute Atoms that Diffuses to Dislocations
N_o	Dislocation Density (m^{-2})
N_o	Number of Cycles to Damage Initiation
n_o	Initial Concentration (m^{-1})
$N_i(x)$	Nodal Shape Function
Q_∞	Maximum Change in the Size of Yield Surface (MPa)

T	Aging Temperature (K)
u	Threshold Value (μm)
u_i	Nodal Displacement Vector (m)
Y	Geometry Factor

Abbreviations

BSE Backscattered Electron.

CDM Continuous Damage Mechanics.

CTOA Crack Tip Opening Angle.

CZM Cohesive Zone Model.

DCA Direct Cyclic Analysis.

DSA Dynamic Strain Aging.

EBSD Electron Backscatter Diffraction.

EDS Energy Dispersive Spectroscopy.

EVS Extreme Value Statistics.

FEA Finite Element Analysis.

FE-SEM Field Emission Scanning Electron Microscopy.

GOS Grain Orientation Spread.

GPD Generalized Pareto Distribution.

ICP Inductively Coupled Plasma.

ID Inner Diameter.

LCF Low Cycle Fatigue.

LEFM Linear Elastic Fracture Mechanics.

MAWP Maximum Allowable Working Pressure.

MCD Modified Crystal Orientation.

ME Mean Excess.

MERR Maximum Energy Release Rate.

NDT Non Destructive Testing.

PU Partition Unity.

ROI Region of Interest.

SCC Stress Corrosion Cracking.

SE Secondary Electrons.

SEM Scanning Electron Microscopy.

SIF Stress Intensity Factor.

TMF Thermo Mechanical Fatigue.

UTS Ultimate Tensile Strength.

XCT X-ray Computed Tomography.

XFEM Extended Finite Element Method.

Chapter 1

Introduction

The escalating global energy demand has facilitated a paradigm shift towards the enhancement of power plant and refinery productivity. Central to this endeavour is the optimization of individual components and assemblies within power plants which is crucial for the comprehensive enhancement of operational efficiency. Power production facilities are intricate ensembles comprising diverse components and assemblies, each functioning under distinct temperature and pressure regimes. The synergistic impact of these components' performances provides an overall enhancement in structural integrity and performance.

Water walls hold a crucial and essential role in the operation of power plants. These structures are subject to demanding and harsh environments characterized by extreme temperature and pressure variations. They are exposed to high-temperature fire, low-temperature steam, and surrounding air on the internal, middle, and external sides, respectively. This exposure imposes severe thermo-mechanical strains on these components, accompanied by substantial oxidation on the fire-side surfaces due to the corrosive flue gases. Consequently, over the course of their service life, water walls experience gradual deterioration.

The degradation of water walls, particularly on the water-facing side, is primarily attributed to two key factors: water quality and the dynamic pressure and temperature of water. These factors collectively contribute to the development of issues like

scaling and fouling, which reduce the efficiency of the water walls and can become significant causes of failure at later stages. Notably, mechanical and thermal loading-induced fatigue, accompanied by creep and overheating, is a key contributor to water wall failures. The detrimental effects of corrosion further compound the failure mode.

Additionally, the fabrication of water walls can also become a source of early failure. These structures are often constructed from multiple tubes parallelly welded together. Unfortunately, the welding process sometimes introduces defects such as a lack-of-fusion and porosity. These defects typically arise due to poor workmanship and the selection of inappropriate welding parameters. These weld defects within water walls create localized areas of stress concentration, facilitating the initiation and propagation of fatigue cracks under operational conditions.

1.1 Research gaps

Existing research on water wall failures has predominantly concentrated on studying microstructural degradation and oxide formation on water walls, overlooking the significance of pre-existing weld defects as potential sites for crack initiation during plant start-ups and shutdowns. This research gap emphasizes the necessity for a more profound comprehension of the contribution of these defects during hydrostatic testing and fatigue failure in water walls. A comprehensive investigation that explores the effects of weld defects on the properties and performance of water walls is noticeably lacking in the existing literature. Based on the literature review the following gaps were identified:

1. Effect of weld defects during hydrostatic testing of service-exposed water walls.
2. A detailed characterization of these weld defects to understand the most critical defect parameters for fatigue failure.
3. Effect of these pre-existing weld defects on the thermo-mechanical fatigue failure of water walls.

To address these research gaps, this thesis investigates the impact of defects on the mechanical properties of welded water walls under high-temperature conditions. This study employs a combination of experiments and simulation to gain a deeper understanding of these failure mechanisms.

1.2 Objectives of the thesis

The motivation for this thesis is to gain a fundamental understanding of the premature failure observed in defect-containing water walls. The presence of pre-existing weld defects has been found to have a detrimental impact on the performance of water walls, particularly during hydrostatic preload prior to being put into service and thermo-mechanical loading during operation. The thesis aims to achieve the following objectives:

1. Investigate the effect of hydrostatic preload on the strain hardening and strain aging of defect-containing water walls.

2. Perform a comprehensive 3-dimensional characterization of internal weld defects in water wall membranes and establish a fatigue test methodology to assess their impact on low-cycle fatigue performance.

3. Develop a predictive model for fatigue damage and Paris law parameters, that can determine the fatigue life and crack propagation path of defect-containing welded water walls.

1.3 Outline of the thesis

This thesis comprises 7 chapters, each serving a specific purpose within the scope of study. Chapters 2 and 3 lay the foundation by providing a concise literature review on the chosen topic and detailing the materials and methodology employed to address the research objectives. A brief outline of each chapter is listed below:

1. Chapter 4 focuses on examining the impact of hydrostatic preload on strain hardening and strain aging of defect-containing water walls. This chapter utilizes a combination of numerical simulation and multi-scale characterization techniques, such as scanning electron microscopy (SEM) and electron backscatter diffraction (EBSD), to investigate the occurrence of local plasticity near stress concentration regions induced by hydrostatic pressure. The aim is to gain a deeper understanding of the effects of hydrostatic preload on the mechanical behaviour of water wall structures and the associated strain-related phenomena.

2. Chapter 5 delves into the 3-dimensional characterization of internal weld defects in water wall membranes, with the aim of understanding their influence on the low-cycle fatigue performance. A key aspect of this chapter involves establishing a fatigue test methodology specifically designed to evaluate the effects of these defects. Numerical simulation techniques are employed to extract crucial strain conditions experienced during thermo-mechanical loadings. Furthermore, a comprehensive assessment of the weld defects is conducted, considering factors such as defect size, shape, and position, to predict the most favourable sites for crack initiation. By examining these aspects, the chapter aims to provide an understanding of the internal defect parameters that impact the fatigue behaviour of water wall membranes.

3. Chapter 6 is dedicated to the development of a predictive model aimed at determining the fatigue life and crack propagation path of defect-containing welded water walls. To achieve this, a comprehensive investigation is conducted, combining experimental testing with numerical analysis. The chapter focuses on the establishment of fatigue damage and Paris law parameters, which play a crucial role in predicting the fatigue performance of water walls. By integrating experimental data and numerical simulations, the chapter aims to provide an

assessment of the fatigue behaviour and crack propagation characteristics of defect-containing welded water walls.

Chapter 2

Literature Review

2.1 Water walls and classification

Water walls in boilers are crucial components in many combustion systems, consisting of a series of interconnected tubes that form the walls of the boiler's combustion chamber. These tubes are typically welded together tangentially or connected by membrane bars to create a strong and secure structure. The primary function of the water walls is to contain the majority of the water in liquid form, which gradually evaporates and rises within the boiler during the combustion process. The combustion of fuels takes place inside the furnace, while the tubes act as a barrier between the hot gases generated by the combustion and the water inside them. One of the key advantages of water wall panels is their ability to minimize air leakage, ensuring efficient combustion within the chamber. This feature significantly reduces energy losses and helps maintain optimal combustion conditions. Water wall panels also play a vital role in cooling the combustion chamber and other boiler accessories. The design of the panels helps to prevent coking, a process where carbon deposits accumulate on the heating surfaces. By limiting coking, the panels contribute to the overall efficiency and longevity of the boiler. Furthermore, the water wall panels facilitate rapid heating and cooling of the combustion chamber. This quick response time can significantly reduce the start-up and shutdown periods of the furnace, enhancing the overall operational efficiency of the boiler.

Water walls were initially developed to enable the utilization of higher firing rates and elevated furnace heat release rates, concurrently mitigating heat losses and minimizing maintenance requirements [1]. The construction of water wall tubes necessitates the use of high-quality supporting components, including casing, tubes, and fins. A well-executed construction approach significantly reduces heat loss and maintenance needs. Generally, the construction of water wall tubes can be categorized into four types (Figure 2.1):

1. **Tube and Tile Water Wall**: During the initial development of steam boilers, a particular type of construction was commonly used due to limitations in the capabilities of factories or workshops to fabricate tubes that could be rolled into headers, water drums, or steam drums. As a result, the spacing between the tubes was not optimally designed for practical purposes. This construction approach had a significant impact on the heat transfer surface available in the furnace. The inadequate spacing between the tubes in this type of construction resulted in a reduced heat transfer surface area within the furnace. Insufficient heat transfer surface area adversely affected the boiler's performance and efficiency. The restricted surface area impeded the efficient transfer of heat from the combustion gases to the water or steam circulating through the tubes. Consequently, the furnace could not achieve the desired heat transfer rates and overall thermal efficiency.

2. **Tangent Tube Water Wall**: The tubes are welded together in a tangential arrangement, facilitating efficient heat transfer. However, a limitation of this design, as well as the tube and tile water wall type, is the challenge of providing protection to the refractory material due to its direct contact with the burner or combustion process. In boilers utilizing tangent tube wall or tube and tile water wall configurations, the refractory material is exposed to high temperatures, combustion gases, and potential abrasion from the combustion process. This

direct contact can lead to increased wear and tear on the refractory lining, reducing its effectiveness and longevity.

3. **Studded Tube Water Wall**: Studded tube water walls were developed to increase the heat transfer surface area, resulting in improved thermal performance. This approach is commonly utilized in boilers that require enhanced heat transfer efficiency and compact design. However, corrosion attacks can lead to leakage when flue gases flow through the water walls.

4. **Membrane Water Wall**: In the membrane wall construction method, the tubes are interconnected by membrane bars, forming a structure that resembles a membrane. This configuration offers several advantages in terms of structural integrity and separation between the combustion chamber and waterside in boilers. One of the key benefits of the membrane wall configuration is its ability to enhance the overall structural integrity of the water wall. The interconnected tubes and membrane bars distribute the load evenly, providing strength and stability to withstand high pressures and temperatures. This robust construction ensures the integrity of the water wall even under demanding operating conditions. Additionally, the membrane wall design effectively separates the combustion chamber from the waterside. This separation is crucial in high-pressure and high-temperature boilers to prevent direct contact between the combustion gases and the water or steam. The membrane acts as a barrier, allowing for efficient heat transfer while maintaining the integrity and purity of the water or steam circulating through the tubes.

2.2 Failures in water walls

The importance of water walls in industrial plants and refineries cannot be overstated [2]. Operating in environments with harsh flue gases, these tubes endure significant thermal-mechanical fatigue and oxidization due to the extreme conditions

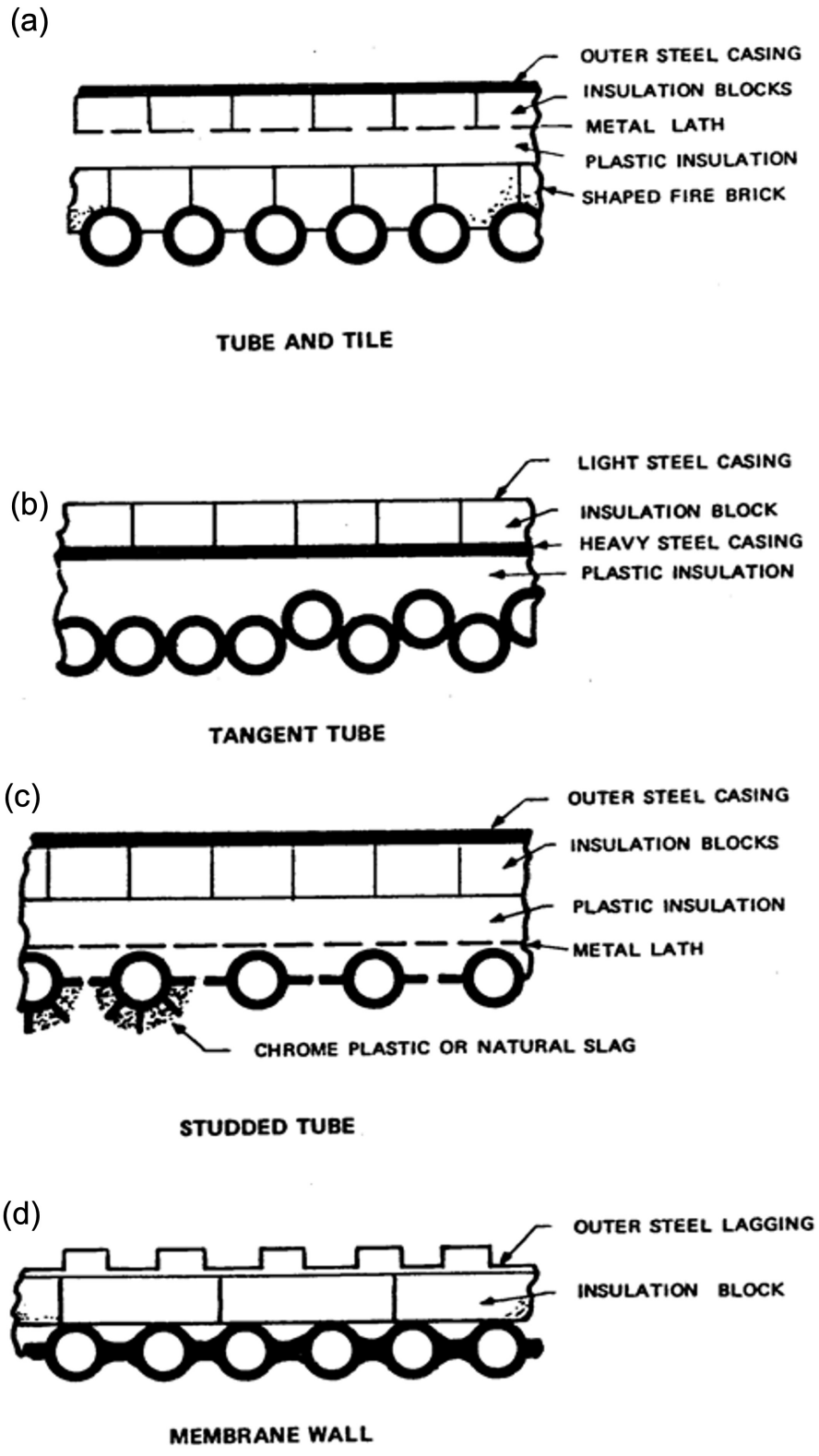

Figure 2.1: Schematic of water walls different water wall construction (a) Tube and Tile Water Wall, (b) Tangent Tube Water Wall, (c) Studded Tube Water Wall, and (d) Membrane Water Wall [1]

they face—exposed to fire on one side and water on the other [3][4]. The corrosive gases present on the fireside gradually contribute to damage over the tubes' service life. Simultaneously, the waterside conditions, influenced by factors like water quality, pressure, and temperature parameters, also subject the tubes to challenging conditions [5][6]. Moreover, discontinuous water flow can lead to localized heating, further increasing the likelihood of damage and failure [7]. Water walls are susceptible to various failure mechanisms, including mechanical fatigue [8], thermal fatigue [9], creep [10], overheating [11], pitting corrosion [12], corrosion fatigue [13], and stress corrosion cracking (SCC) [14].

2.3 Hydrostatic preloading

After prolonged service exposure, water walls often require frequent weld repairs and, in some cases, replacement. As per the CSA boiler code [15], following the repair, hydrostatic testing is mandatory. This testing involves applying and maintaining a pressure of 1.5 times the design pressure for a duration of 10 to 15 minutes before returning the water walls to service. The purpose of this hydrostatic test is to ensure that the water walls are free from critical defects, thereby ensuring their safe and reliable operation.

Hydrostatic testing provides numerous benefits, not only for new boiler components but also for in-service components that have undergone repair. By subjecting the water walls to higher pressures during testing, any existing defects or weaknesses can be identified and addressed [16]. However, it is important to note that service-exposed water walls with degraded sections are more susceptible to fracture, and this susceptibility can potentially lead to failure during the test.

During high-pressure hydrostatic testing, the growth of near-critical defects can occur through mechanisms such as ductile tearing or plastically-induced crack growth, particularly in typical pipeline steels [17]. These defects, if present, may cause structural integrity concerns and compromise the long-term reliability of the water walls.

It is worth noting that leakage during hydrostatic testing is typically only evident if the defects in the boiler tube are sufficiently large. In the case of a repaired service-exposed boiler tube, there may be defects that are not large enough to cause leakage during the hydrostatic test [18]. However, it is important to be cautious about overloading water walls containing defects during hydrostatic testing, as this can result in local plasticity near the defect sites, leading to unintended detrimental effects due to stress concentration at the crack tips [19] [20]. Additionally, the life of service-exposed water walls that have passed hydrostatic testing may be shortened due to the excessive loading applied during the tests.

Excessive overloading during hydrostatic testing, even if the boiler tube passes the test, can potentially lead to local hardening damage. Similar observations have been reported in the literature, such as the occurrence of plastic deformation near SCC tip regions during hydrostatic testing of microalloyed steel pipelines [20]. Although these weld defects may initially appear insignificant, there have been numerous reported failure cases of water walls attributed to the presence of such defects.

One phenomenon resulting from the presence of local plastic zones near crack tips is strain hardening and strain aging. Research by Zhao et al. [21] examined the effects of strain aging on pipeline steels and demonstrated significant alterations in tensile properties with as little as 3% plastic pre-strain. To ensure the reliability and longevity of water walls, it is crucial to thoroughly assess the presence of defects, properly manage the hydrostatic testing process, and consider the potential impact of excessive loading.

2.4 Fatigue failure in water walls

Failures in water walls can occur due to various factors during their production and service [22]. Issues such as improper welding parameters and poor workmanship can lead to the creation of weld defects, which can ultimately result in failure during the operation of the boiler. Analyzing failures in low alloy steel water walls has indicated

that incomplete fusion due to improper welding processes or parameters can be a significant contributing factor [23] [24]. Water walls operate in harsh environments, and their failure can be a major cause of power plant shutdowns. At operating temperatures below 623K, the effects of creep on water walls are minimal, making Low-cycle Fatigue (LCF) failure one of the dominant failure modes [25]. Himarosa et al. [26] conducted a study on failure mechanisms in superheater tubes, water wall tubes, and seal pot plates. They found that the water wall exhibited incomplete penetration weld defects. The failure was suspected to be caused by crack propagation from these weld defects under thermal fatigue conditions. Similarly, Ghosh et al. [27] reported a case of failure in water walls attributed to mechanical fatigue. The fatigue crack originated from the weld defects, indicating that the presence of such defects can serve as potential stress concentrators, leading to failure over time.

It is well known that welded joints generally exhibit inferior fatigue strengths compared to the base material due to the as-cast microstructure of the weld and possible defects that serve as crack initiation sites [28][29]. To enhance the fatigue life of welded joints, reducing the stress concentration factor at the weld toe is crucial [30]. Ottersbock et al. compared defect-free weld specimens with defective specimens and observed a significant decrease in the fatigue strength of the defective specimens, with the lack of fusion defects being a primary factor contributing to the inferior fatigue life of the welded components [31][32].

To mitigate the risk of failures related to weld defects in water walls, it is crucial to ensure proper welding processes, including accurate parameter selection and adherence to established welding standards. Qualified and skilled welders should be employed to carry out the welding operations with attention to detail and strict adherence to quality control procedures. Furthermore, conducting regular inspections, including non-destructive testing techniques, can help identify and address any weld defects or anomalies early on. Implementing a comprehensive inspection and maintenance program can significantly contribute to the prevention of failures related to

weld defects and extend the service life of water walls.

2.5 Fatigue failure

Failures occurring under conditions of dynamic loadings are referred to as fatigue failures, which typically happen after a significant number of service cycles [33]. Various industries utilize fatigue tests to estimate the life cycle of their components. The fatigue properties of a material are assessed through fatigue tests conducted at different temperatures in accordance with the ASTM E606 [34] standard. There are three fundamental factors that can potentially contribute to fatigue failure:

1. **Applied Stress**: The magnitude of the cyclic stress applied to a material plays a crucial role in fatigue failure. If the stress exceeds the material's endurance limit or fatigue strength, cracks may initiate and propagate, leading to failure.

2. **Number of Load Cycles**: The number of load cycles experienced by a component significantly affects its fatigue life. Fatigue failure is more likely to occur as the number of cycles increases, even if the applied stress is below the material's endurance limit.

3. **Material Properties**: The inherent properties of the material, such as its fatigue strength, ductility, and resistance to crack propagation, influence its resistance to fatigue failure. Materials with higher fatigue strength and better fracture toughness are more resistant to fatigue damage.

The total fatigue life of components can be divided into four distinct stages [35]:

1. **Crack Initiation**: In this stage, a small crack forms due to high-stress concentration at a specific location within the component. This stress concentration can be caused by various factors, such as geometrical irregularities, material defects, or external loads.

2. **Slip-band Crack Growth**: Also known as stage I crack growth, this stage involves the propagation and deepening of the initial crack along the planes of higher shear stresses. The crack grows incrementally as the component undergoes cyclic loading and unloading, resulting in the formation of slip bands and the advancement of the crack.

3. **Crack Growth on Planes of High Tensile Stress**: Referred to as stage II crack growth, this stage occurs when the crack transitions from propagating along shear planes to growing on planes of high tensile stress. The crack extends perpendicular to the direction of the applied tensile load, gradually increasing in length.

4. **Final Fracture**: The final stage occurs when the crack reaches a critical length at which the cross-section of the component can no longer support the applied load. At this point, the component experiences a catastrophic failure, resulting in fracture.

2.5.1 Low cycle fatigue failure

The fatigue life of a component can be characterized using either a strain-life approach or a stress-life approach. Depending on the strain amplitude and the number of cycles, fatigue tests can be further categorized into high-cycle fatigue tests and low-cycle fatigue tests.

LCF failure occurs when a component experiences relatively large plastic strains and a low number of load cycles ($N < 10^5$) until failure. This type of failure is particularly important in the design of power machinery, such as steam turbines and nuclear power vessels [36].

During a low-cycle fatigue test, stresses greater than the material's yield strength are applied, resulting in significant plastic deformation. The test is typically represented by plotting the plastic strain range ($\Delta\epsilon_p$) against the number of cycles (N) on

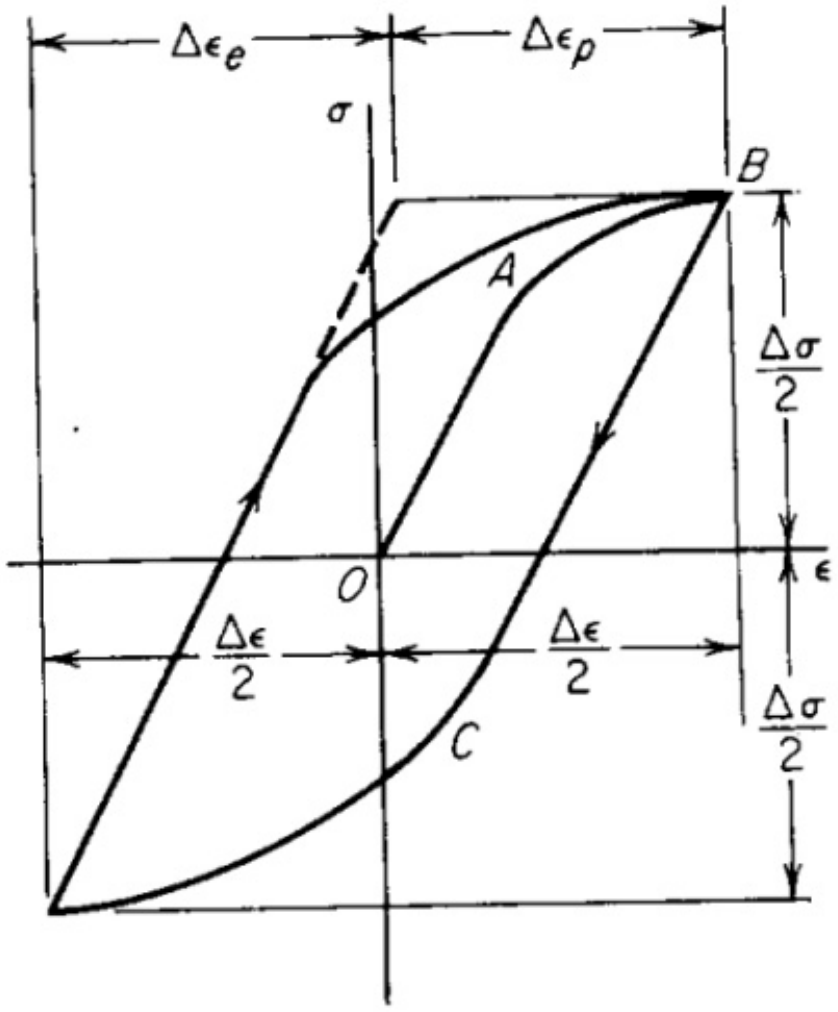

Figure 2.2: Hysteresis loop for constant strain cycling [37]

a logarithmic scale. Figure 2.2 depicts a stress-strain loop observed during a strain-controlled low-cycle fatigue test. The stress-strain curve follows a path O-A-B during the initial loading phase. Upon unloading, yielding initiates in compression at a lower stress level C, a phenomenon attributed to the Bauschinger effect. Subsequent reloading in tension results in the development of a hysteresis loop. The dimensions of this hysteresis loop are defined by its width, represented by $\Delta\epsilon$, which is the total strain range, and its height, denoted as $\Delta\sigma$, corresponding to the stress range. The total strain range $\Delta\epsilon$ encompasses both an elastic strain component and a plastic strain component.

The behaviour of low-cycle fatigue can be described using the Coffin-Manson relation (equation 2.1), which provides a relationship between the plastic strain amplitude and the number of cycles to failure:

$$\frac{\Delta\epsilon_p}{2} = \epsilon_f^{'}(2N_f)^c \tag{2.1}$$

where, $\frac{\Delta\epsilon_p}{2}$ is the plastic strain amplitude, $\epsilon_f^{'}$ is the fatigue ductility coefficient, $2N_f$ is the number of strain reversals to failure, c is the fatigue ductility exponent which varies from -0.5 to -0.7. The Basquin-Manson-Coffin equation is frequently adopted (which is a modification of equation 2.1) under fully reversed strain-controlled uniaxial loading ($R_\epsilon = -1$) which is expressed as:

$$\epsilon_a = \frac{\sigma_f^{'}}{E}(2N_f)^b + \epsilon_f^{'}(2N_f)^c \tag{2.2}$$

where ϵ_a is the normal strain amplitude, $\sigma_f^{'}$ is the fatigue strength coefficient, E is Young's Modulus, and b is defined as the fatigue strength exponent which varies from -0.05 to -0.12. To encompass the detrimental effects of a non-zero mean stress, Smith-Watson-Topper (SWT) [38] parameter has been incorporated into the Basquin-Manson-Coffin equation:

$$\epsilon_a\sigma_{max} = \frac{\sigma_f^{'\,2}}{E}(2N_f)^{2b} + \sigma_f^{'}\epsilon_f^{'}(2N_f)^{b+c} \tag{2.3}$$

where σ_{max} is the maximum normal stress.

2.5.2 Thermo-mechanical fatigue

Thermo-mechanical fatigue (TMF) arises from the combination of varying thermal and mechanical loads, with both stresses and temperatures changing over time. This kind of loading can induce significantly greater damage to the components compared to isothermal fatigue at maximum operating temperatures. Such loading conditions are commonly encountered during the start-up and shut-down cycles of high-

temperature components and equipment.

Thermo-mechanical fatigue loading is typically categorized as in-phase or out-of-phase as shown in Figure 2.3. In out-of-phase loading, the material experiences compression at elevated temperatures and tension at lower temperatures. Out-of-phase loading is more likely to induce oxidation damage, as an oxide film can develop during compression at elevated temperatures and then fracture during subsequent low-temperature tensile loading, given the increased brittleness of the oxide film in that phase of the cycle. The TMF test is considered to be in phase when the maximum tensile strain coincides with the peak temperature and the maximum compressive strain aligns with the minimum temperature [39]. Such in-phase conditions render the component more susceptible to propagating creep damage during tensile stresses experienced at elevated temperatures.

A key distinguishing factor between isothermal and thermo-mechanical fatigue is constraint. As structures heat up, thermal gradients form due to expansion. Regions close to stress concentration points can be constrained by cooler surroundings, leading to the conversion of thermal strain into mechanical strain and consequent fatigue damage. Complete constraint occurs when all thermal strain transforms into mechanical strain.

Nagesha et al. [41] conducted a study on stainless steel's behavior under both in-phase and out-of-phase thermo-mechanical fatigue (TMF) conditions . They observed that TMF cycling induced significant mean stresses and resulted in shorter lifespans compared to LCF conditions. Additionally, the study successfully used an isothermal database and a modified damage function to predict TMF life. In a separate work by Li et al. [42], TMF tests were performed under in-phase and out-of-phase conditions for stainless steels. The study highlighted dynamic strain aging (DSA) and oxidation as the primary deformation and damage mechanisms. It was found that oxide layers preferentially formed along persistent slip markings on the surface, accelerating microcrack initiation and propagation, ultimately leading to oxidation-assisted trans-

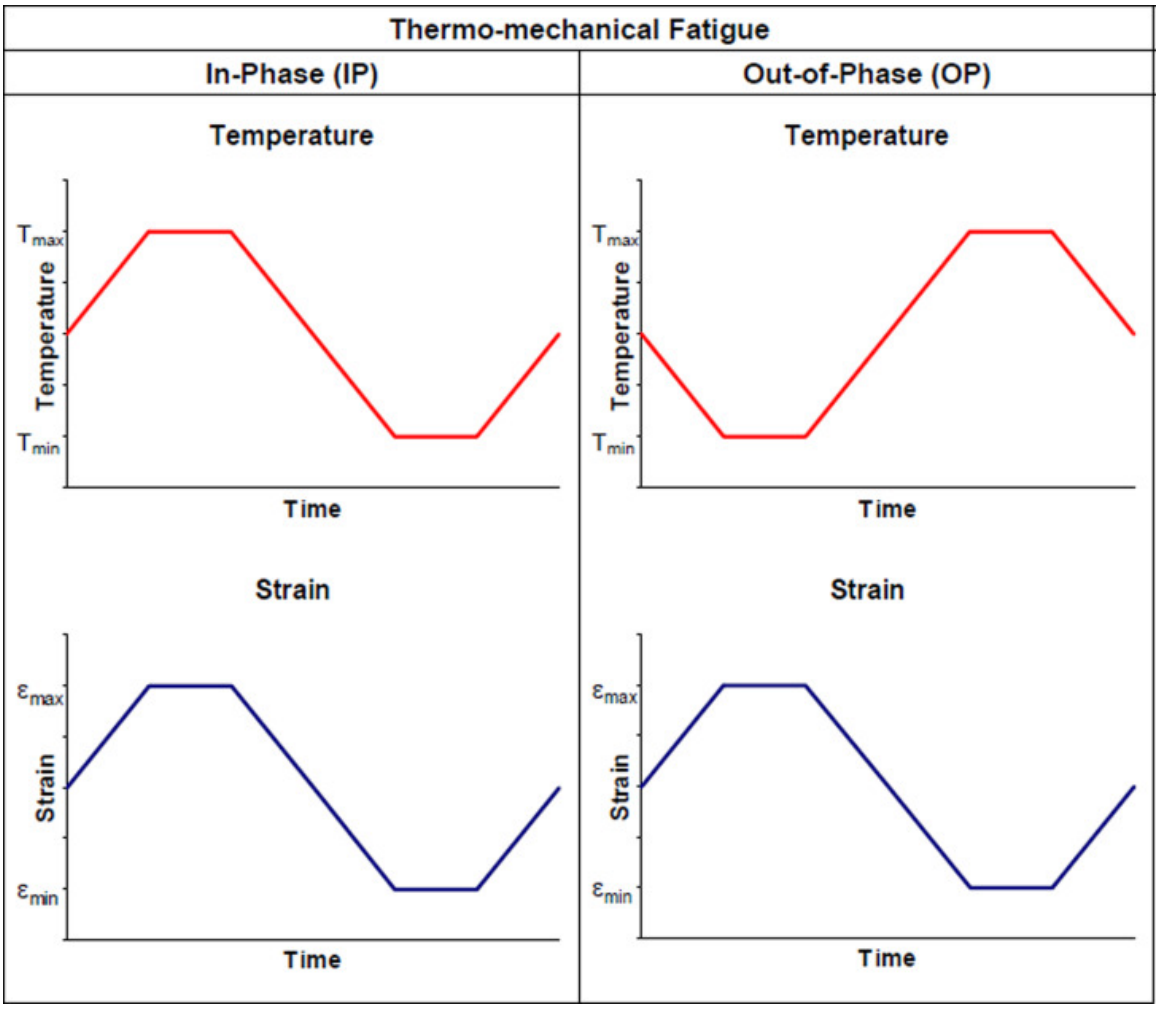

Figure 2.3: Phase orientation of Thermo Mechanical Fatigue [40]

granular failure. Sun et al. conducted a study [43] that delved into multiaxial TMF effects on IN718. The study introduced a novel model designed to accurately account for the impact of changing temperatures and non-proportional loads during the TMF process.

2.5.3 Mechanical metallurgy of fatigue failure

LCF failure in water walls is characterized by the formation of parallel or intersecting slip lines, which are primarily caused by dislocation sliding under shear stresses [44]. These slip bands persist during cyclic inelastic deformation and act as stress concentrators, leading to crack initiation [38]. They are formed by micro-plastic deformation and accumulate in grains to minimize the total free energy. The surface markings formed by intrusions and extrusions of persistent slip bands provide sites for crack initiation [45].

Studies conducted on austenitic stainless steel have shown that fatigue cracks initiate from persistent slip bands at the surface [44]. Crack initiation from the surface has been observed even in pure ductile metals without any intrinsic defects. The fatigue transient fracture zone exhibits a typical dimple structure with a sharp periphery (appearing brighter) and a flat bottom (appearing darker). Well-developed striations, which are characteristic markings perpendicular to crack growth, are also observed [46]. These striations indicate a transgranular mode of crack growth, which is commonly observed in fatigue cracking. Similar observations have been made by Wang et al. during LCF tests on TA19 samples [47].

2.5.4 Stress Intensity Factor

The stress intensity factor (K) serves as a tool for estimating the stress conditions near the tip of a crack or notch that arises due to an external force or residual stress [48]. This theoretical approach is applied to materials that are homogeneous and linearly elastic, primarily serving as a failure criterion for brittle substances. Additionally, it

is relevant for materials that experience small-scale yielding at the tip of a crack. The stress distribution at the crack tip for a thin plate elastic solid is expressed as [49]:

$$\begin{aligned}
\sigma_x &= \sigma \left(\frac{a}{2r}^{1/2}\right) \left(cos\frac{\theta}{2}\left[1 - sin\frac{\theta}{2}sin\frac{3\theta}{2}\right]\right) \\
\sigma_y &= \sigma \left(\frac{a}{2r}^{1/2}\right) \left(cos\frac{\theta}{2}\left[1 + sin\frac{\theta}{2}sin\frac{3\theta}{2}\right]\right) \\
\tau_{xy} &= \sigma \left(\frac{a}{2r}^{1/2}\right) \left(cos\frac{\theta}{2}sin\frac{\theta}{2}sin\frac{3\theta}{2}\right)
\end{aligned} \tag{2.4}$$

Irwin pointed out that local stresses near the crack depend on the product of nominal stress σ and the square root of the half-flow length. This relationship is called as stress intensity factor K. The magnitude of K depends on variables like the applied load's strength, the shape of the specimen, and the size and position of the crack or notch. Mathematically, K can be expressed as:

$$K = \sigma\sqrt{\pi a} f(a/W) \tag{2.5}$$

where σ is the applied stress, a is the crack length, and $f(a/W)$ is a specimen geometry function.

There are various modes of deformation that can be applied to a crack, each defining how stress affects the crack as shown in Figure 2.4. In Mode I, which is the crack opening mode, a tensile stress is applied perpendicular to the crack's surfaces. This mode is commonly used in tests to measure fracture toughness and the critical stress intensity factor (K_{IC}). Critical Stress Intensity Factor (K_{IC}) is the material resistance to crack extension in mode I loading. In Mode II, known as the forward shear mode, a shear stress is applied perpendicular to the crack's front edge but within the plane of the crack. Mode III, called the parallel shear mode, involves shearing stresses applied parallel to the crack's leading edge. Among these modes, Mode I loading is the most significant.

Within Mode I loading, there are two distinct scenarios. When dealing with thin plate-like specimens, the stress condition is categorized as plane stress. On the other

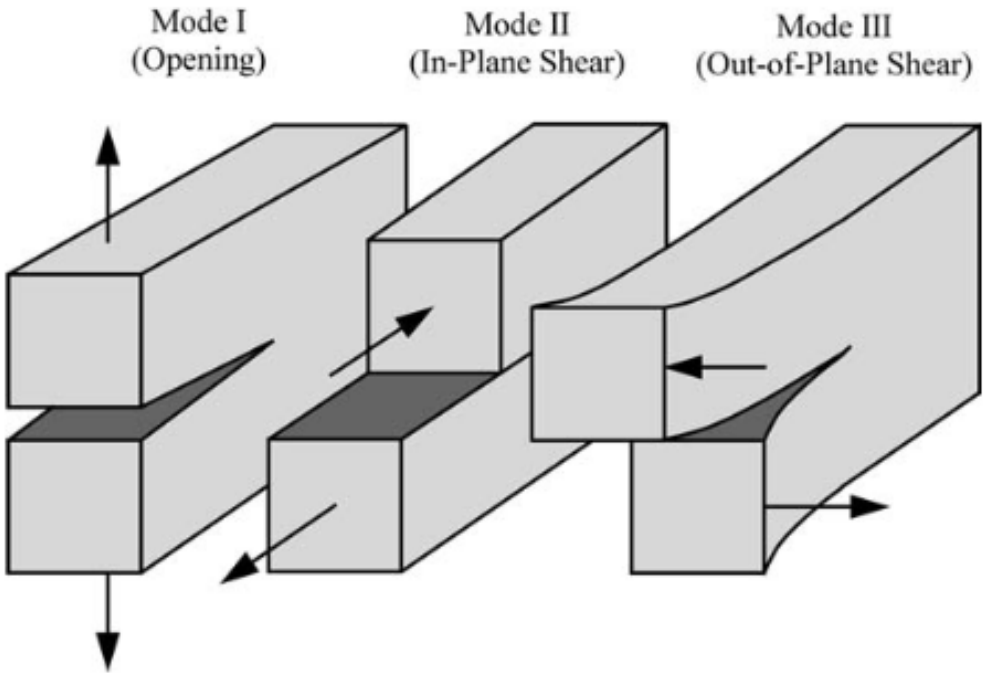

Figure 2.4: Three modes of cracking that can be applied to a crack [50]

hand, for thick specimens, a plane-strain condition prevails. The plane-strain condition represents a more intense stress state, leading to lower values of the stress intensity factor (K) compared to those seen in plane-stress specimens. The critical stress intensity factor (K_{IC}) values observed under the plane-strain condition serve as valid material properties, remaining unaffected by the thickness of the specimen.

2.5.5 Notch effect on the fatigue life

The fatigue strength of material gets reduced to a great extent with the increase of stress due to the existence of a notch or a hole. It is not surprising to see fatigue cracks taking place in machine elements containing stress risers like keyways, fillets, screw threads and holes [37][51][47]. Usually, specimens with a V-notch or a circular-notch are used to study the effect of stress raisers on the fatigue behaviour of the samples. The introduction of a notch leads to the following 3 effects:

1. Triaxial state of stress is produced.

2. There is a concentration of stress at the root of the notch.

3. A stress gradient is set up from the root of the notch to the centre of the specimen.

The fatigue-strength reduction factor (K_f) is a parameter used to measure the impact of a notch on reducing the fatigue limit of a specimen. It is defined as the ratio of the fatigue limit of an unnotched specimen to that of a notched specimen.

The published values of K_f can vary significantly, showing considerable scatter. However, there is a general trend observed for completely reversed loading conditions: the elastic stress concentration factor (K_t) is typically larger than the fatigue strength reduction factor (K_f) [52]. This is because fatigue crack initiation is influenced not only by the maximum stress but also by the stress distribution in the vicinity of the notch tip.

The effect of the notch on fatigue failure is strongly dependent on the size of the notch. For a given stress concentration factor, as the notch size decreases, the impact of the notch on fatigue failure decreases as well. Furthermore, below a certain notch size, the notch has no effect on the fatigue limit of the specimen [53].

Inclusions, which are foreign particles or impurities present in a material, can also act as stress concentrators and potential crack initiation sites (Figure 2.5). Tanaka et al. [54] proposed a crack propagation model specifically for cracks initiated from inclusions within a specimen. The propagation process is divided into three stages:

1. **Stage 1**: The crack propagates within the region surrounding the inclusion, which is characterized by a fine-granular facet area.

2. **Stage 2**: The crack propagates outside the inclusion region, extending through the bulk of the material. It should be noted that in this stage, crack propagation occurs without any significant environmental effects.

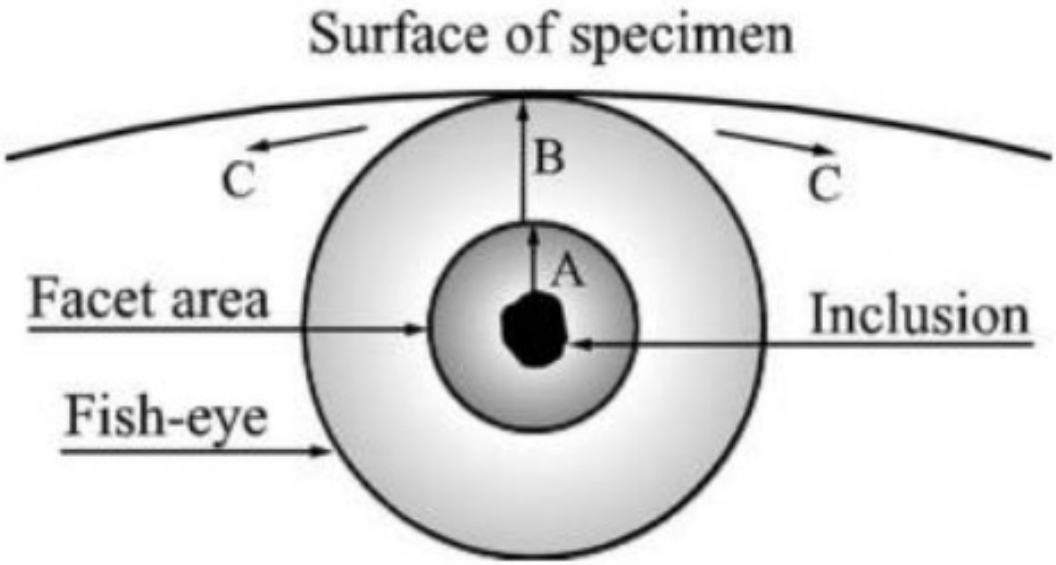

Figure 2.5: Crack initiation from an inclusion [54]

3. **Stage 3**: The crack reaches the surface of the specimen and continues to propagate as a surface crack.

To calculate the stress intensity factor (K_I) when a crack initiates from an inclusion, Murakami's equation can be employed (Equation 2.8). The stress intensity factor is a parameter that describes the stress state at the crack tip and is useful for assessing crack growth behaviour and predicting fatigue life. By determining the stress intensity factor, the critical conditions for crack initiation and propagation can be evaluated, providing insights into the material's fracture mechanics properties.

$$K_I = 0.5\sigma_{max}\sqrt{\pi\sqrt{area_{inclusion}}} \tag{2.6}$$

where σ_{max} is the maximum stress.

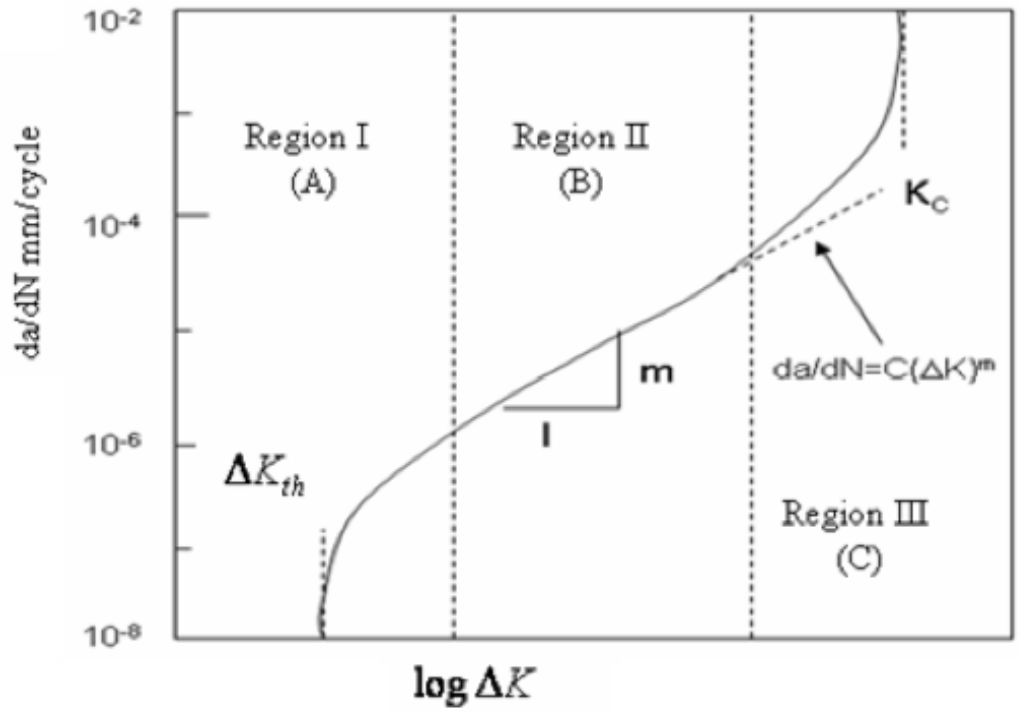

Figure 2.6: Schematic representation of crack growth curve [55]

2.6 Fatigue crack propagation models

A fatigue crack growth curve expressed as da/dN versus ΔK is illustrated in Figure 2.6. The curve has a sigmoidal shape that can be divided into three regions referred to as Region I, Region II, and Region III.

Region I

Region I characterizes the initial progression of fatigue crack initiation and propagation. In this phase, susceptibility to microstructural variations, environmental influences, and mean stress are particularly pronounced. An important characteristic of this region is the presence of a stress intensity factor range blow which the advancement of fatigue cracks is constrained. This critical threshold is termed the fatigue crack growth threshold, designated by the symbol ΔK_{th}.

Region II

Region II is a phase characterized as an intermediate stage of crack propagation. Within this domain, the length of the plastic zone preceding the crack tip is notably longer in comparison to the mean grain size, although significantly shorter than the actual crack length. This region is marked by a linear association between the logarithm of the rate of crack growth ($\log \frac{da}{dN}$) and the logarithm of the stress intensity factor range ($\log \Delta K$). This correspondence signifies a state of stable crack growth within the material. Notably, the influence exerted by environmental factors, microstructural attributes, and mean stress is relatively subdued in this phase.

Region III

Region III corresponds to the phase of fatigue crack growth characterized by exceedingly high rates, where the rate of crack propagation ($\frac{da}{dN}$) exceeds 10^3 mm per loading cycle. This accelerated growth arises due to rapid and unpredictable crack advancement that transpires just prior to ultimate failure. Within this region, the curve depicting the relationship between $\frac{da}{dN}$ and the stress intensity factor range (ΔK) displays a steep incline, signifying the involvement of high-stress levels. Consequently, a substantial plastic zone emerges in close proximity to the crack tip.

The applicability of Linear Elastic Fracture Mechanics (LEFM) becomes insufficient during this phase. The complexity of fatigue crack propagation analysis escalates significantly in Region III due to the unpredictable and rapid nature of crack advancement. Nonetheless, this phase is often relegated to a lower priority or ignored, mainly because its significance is limited in most fatigue scenarios.

2.6.1 Paris model

The Paris model represents the linear segment observed in the log-log graph of crack growth rate ($\frac{da}{dN}$) versus stress intensity factor range (ΔK), corresponding to Region II [56]. This formulation marks the initial application of fracture mechanics principles

to the realm of fatigue, and is represented by the following equation:

$$\frac{da}{dN} = A(\Delta K)^p \tag{2.7}$$

Here, the parameter p represents the slope of the curve, and A represents the intercept. The Paris Law is characterized by its simplicity, necessitating the determination of only two curve-fitting constants, which can be readily acquired. This model finds utility as long as the data aligns with a linear relationship, typically evident within Region II. However, it should be noted that the Paris Law's applicability is constrained to this specific region. In cases where the data displays a threshold behaviour (Region I) or accelerated growth (Region III), the Paris Law falls short of accurately describing these regions. Depending on the precise nature of the analysis, this approximation may not suffice. Furthermore, the Paris Law does not encompass the influence of the stress ratio; its applicability is reliant on the material under consideration. The value of p is typically around 3 for steels and ranges from 3 to 4 for aluminum alloys.

2.6.2 Walker model

A significant drawback of the Paris law lies in its incapability to accommodate variations in stress ratio. Walker [57], addressed this limitation by refining the Paris model and introducing the parameter R, which is the stress ratio. The equation governing crack propagation is represented as follows:

$$\frac{da}{dN} = A\left(\frac{\Delta K}{(1-R)^{1-\gamma}}\right)^p \tag{2.8}$$

In this formulation, γ stands as a material-specific factor that signifies the impact of the stress ratio on the rate of fatigue crack growth. γ is often assigned a value of approximately 0.5. It is presumed that the compressive phase of the loading cycle ($R < 0$) doesn't substantially influence crack growth since the crack tends to close at zero load and does not behave as a crack during compressive forces. This refined model takes into account the interaction between stress ratio and crack growth, thereby

enhancing the Paris law's accuracy in predicting fatigue behaviour in a wider range of real-world scenarios.

2.6.3 Forman model

Both the Paris model and the Walker model were devised to address the crack growth curve's Region II, yet neither accounted for the instability observed in crack growth as the stress intensity factor approached its critical value. Forman, building upon these models, aimed to encompass the characteristics of Region III, which incorporates the stress ratio's impact [58].

The improved Forman model is described by the equation:

$$\frac{da}{dN} = A\left(\frac{\Delta K}{(1-R)K_C - \Delta K}\right)^p = A\left(\frac{\Delta K}{(1-R)(K_C - K_{max})}\right)^p \tag{2.9}$$

where, A and p represent material-specific properties, while K_c stands for the fracture toughness of the material at a given thickness. K_{max} is the stress intensity factor at maximum stress during a loading cycle. K_{min} is neglected as the crack does not propagate during the compression part of the loading cycle. Equation 2.9 indicates that as K_{max} gets closer to K_c, the crack growth rate ($\frac{da}{dN}$) increases significantly. This implies that as the stress intensity factor reaches a critical level, the crack propagation rate tends toward infinity. As such, the Forman equation demonstrates the capacity to model both stable intermediate growth (Region II) and the rapid acceleration of crack growth rates (Region III). This refined model thus offers a comprehensive framework that addresses various phases of crack propagation, better aligning with real-world fatigue behaviour in a wider spectrum of conditions.

2.6.4 Elber model

Elber highlighted the potential for a crack to close under externally applied tensile stress due to the presence of compressive residual stress at the crack tip [59]. Elber refined the Paris equation to accommodate this phenomenon by introducing the con-

cept of crack closure, characterized by the opening stress intensity level (K_{op}). Below this threshold, the crack tip remains immobile, impeding growth. To facilitate this, he introduced an effective stress intensity ratio (U), mathematically defined as:

$$U = \frac{\Delta K_{eff}}{\Delta K} = \frac{K_{max} - K_{op}}{K_{max} - K_{min}} \tag{2.10}$$

Drawing on this concept, Elber adapted the Paris equation:

$$\frac{da}{dN} = A(\Delta K_{eff})^p = A(U\Delta K)^p \tag{2.11}$$

However, certain limitations accompany this model. The relationships governing U and K_{op} necessitate determination specific to the material, type of loading, and the fatigue rate curve's region. Moreover, defining the closure load remains somewhat arbitrary, an aspect that remains under ongoing research scrutiny. Elber's model introduces a more meticulous understanding of crack behaviour by accounting for closure effects, yet its applicability relies on accurate characterization and comprehensive comprehension of material behaviour and loading conditions.

2.7 Numerical methods for fatigue crack growth modeling

Numerical modeling provides a swift and economical approach to comprehending failure mechanisms, particularly in cases involving crack propagation. This method proves effective when dealing with loading conditions that are sufficiently gradual, permitting the application of equilibrium assumptions at each loading step, a scenario often referred to as quasi-static conditions Among the diverse array of methodologies embraced for numerical crack growth modeling, the Cohesive Zone Model (CZM) emerges as a prominently favoured choice [60]. Initially conceptualized by Dugdale [61] and later refined by Barenblatt [62], the CZM concept revolves around focusing the entirety of the fracture process within a narrow cohesive zone. Within this zone,

localized fracture occurs as stress attains its threshold, subsequently causing stress to diminish to zero. The material behaviour within this region is defined by a localized constitutive law, known as the Traction Separation Law, linking the transferred traction across the cohesive zone with the displacement jump, or separation.

CZMs have found extensive application in simulating the fracture processes across diverse material systems such as metallic materials, polymers, ceramics, and composites. Ren et al. [63], utilized CZM to model the dynamic fracture toughness of API X80 line pipe steel. The FEA simulation results: loading-displacement curves, fracture speeds, and crack tip opening angles (CTOA), were compared with experimental outcomes, revealing notable agreement. Ghandriz et al. [64], adopting an anisotropic CZM, studied the fracture of additively manufactured polymer materials with varying layer orientations. Distinct fracture behaviours within additively manufactured ABS samples featuring differing layer orientations were effectively captured. Hillerborg et al. [65] used CZM for concrete fracture modeling. These instances underscore CZM's versatility and efficacy in simulating intricate fracture behaviours across diverse material systems.

An alternative approach employed to simulate crack growth is the utilization of the Extended Finite Element Method (XFEM), which was initially introduced by Belytschko et al. [66]. XFEM has been gaining traction, especially for addressing engineering problems characterized by discontinuities. Given the resource-intensive nature of fatigue simulations, often leading to prolonged processing times, XFEM has emerged as a prominent numerical technique for simulating fatigue-induced fracture. A distinctive advantage of XFEM lies in its capability to model cracks independently of the actual structural mesh, imparting the flexibility of requiring minimal or no re-meshing. By virtue of XFEM, the modeling of cracks can be achieved without necessitating significant modifications to the mesh, eliminating the need for intricate mesh adjustments and facilitating the simulation process. This attribute makes XFEM a potent tool for fatigue analysis, offering a practical solution to the challenges

posed by crack propagation simulations.

Singh et al. [67] used XFEM to assess the fatigue life of plates featuring multiple discontinuities, including cracks. Similarly, Wang et al. [68] explored the behaviour of cracks within a catapult joint using XFEM. Xiao et al. [69] delved into fatigue crack initiation and growth in a steel pipeline, encompassing 3D coplanar and non-coplanar semi-elliptical surfaces and embedded elliptical cracks, utilizing XFEM. They found that XFEM's predictions matched well with experimental outcomes documented in the open literature.

A notable prospect for fatigue simulation lies in the amalgamation of Continuous Damage Mechanics (CDM) theory with cyclic plasticity models. Building on this, Song et al. [70] and Biglari et al. [71] adopted the CDM numerical framework to simulate fatigue life for 10CrNi3MoV steel/weldments and 9Cr steel, respectively. Zhang et al. [72] harnessed XFEM for LCF analysis concerning offshore pipeline housing with embedded semi-elliptical cracks exposed to cyclic tension loads. A comparison of experimental and simulation results indicated a favourable concurrence within the studied scenarios.

The integration of the direct cyclic approach with the XFEM for fatigue damage modeling is predicated on the assumption that the behaviour of elastic-plastic structures, subjected to repetitive cyclic loading, may eventually attain a state of stability. This stabilized state is characterized by a consistent stress-strain relationship across successive cycles, mirroring that of previous cycles. In the direct cyclic algorithm a customized Newton method, complemented by Fourier-based solution representation and residual vector analysis, is utilized to directly derive the stabilized cyclic response.

In the context of Abaqus XFEM, this approach finds application in LCF analysis, correlating the rate of fatigue crack propagation with the fracture energy release rate (or strain energy release rate) at the enriched elements' crack tips. The onset of fatigue crack initiation occurs when the energy release rate surpasses predefined threshold values, in accordance with a governing equation:

$$\frac{N}{c_1 \Delta G^{c_2}} > 1 \tag{2.12}$$

where, N signifies the number of cycles, c_1 and c_2 are material properties and ΔG is the energy release rate at the corresponding load cycle. The trajectory of fatigue crack propagation is governed by the Paris law in energy terms, presented as:

$$\frac{da}{dN} = c_3 \Delta G^{c_4} \tag{2.13}$$

where, $\frac{da}{dN}$ is the rate of fatigue crack growth per loading cycle; c_3 and c_4 are fatigue properties of the material; ΔG is the range of relative energy release rate when a structure undergoes loading, spanning from the minimum to maximum load conditions.

2.8 Analysis of internal defects

Traditional cross-sectional and bulk-density analysis methods have limitations in quantitatively characterizing welding defects [73]. Cross-sectional analysis may not capture the spatial distribution of defects, while density-based methods may not provide detailed information on defect morphology and distribution [74]. X-ray computed tomography (XCT) has emerged as a valuable technique for characterizing defects in welds and additively manufactured components [75][76]. XCT can offer high-resolution imaging and provide insights into the spatial distribution of defects [77]. However, its application is currently limited to small material volumes, often requiring the sectioning of parts due to the dependence on specimen size for accuracy.

Researchers utilize various defect parameters such as size, shape, position, and stress intensity factor to quantify defects and assess their impact on fatigue life [78] [79] [80]. Methods like extreme value statistics (EVS) based on the Gumbel distribution, as implemented by Murakami, have been used to estimate the largest defect in cast steel structures [81]. Other approaches, like the implementation of the General-

ized Pareto Distribution (GPD) by Romano et al. [82], have been used to characterize defect size in XCT scans of additively manufactured parts, providing accurate predictions of maximum defect size.

Studies have shown that fatigue crack propagation is significantly slower for internal defects compared to surface defects, with surface or sub-surface defects with sharp topologies being the primary sites of fatigue crack initiation [80][83][84]. Various methodologies, including those proposed by Murakami, LEFM, and topology measurements, have been employed to measure stress intensity factors associated with defects [85][86][87].

The fatigue life and initiation site of defects are significantly influenced by their shapes [88]. Sharper defects tend to adversely impact fatigue performance due to elevated stress intensity factors in their proximity [89]. To provide a quantifiable measure of defect shapes, a global equivalent geometry is assigned to the local defect geometry [88]. In the context of three-dimensional analyses, defect shapes can be assessed using parameters like sphericity and aspect ratio [90]. Transitioning from highly irregular, interconnected, and elongated defects (representative of Lack of Fusion defects) to spherical pores, both defect sphericity and aspect ratio increase [90]. The aspect ratio is quantified by fitting a bounding ellipse onto the projected defect areas, with the aspect ratio being the ratio of the bounding ellipse's major axis to its minor axis [91].

In the work by Kabir et al. [92], complex pore geometries were approximated by overlapping spheres of varying sizes. This approach enabled an exploration of the correlations among process parameters, pore morphology, and subsequent mechanical properties through a finite-element-based simulation framework. Furthermore, Ziolkowski et al. [77] classified defects based on sphericity factors, and their three-dimensional findings revealed that a majority of the detected defects exhibited irregular shapes with sphericities significantly less than unity.

Chapter 3

Materials and Methodology

3.1 Materials

ASME SA-192 water walls are considered in this investigation. The chemical composition of the materials used in these water walls is determined using Inductively Coupled Plasma (ICP) analysis. The detailed chemical composition of the materials is tabulated in Table 3.1.

Table 3.1: Chemical composition of ASME SA-192 steel (wt %)

	C	**Mn**	**Cr**	**Mo**	**P**	**Si**	**S**	**Fe**
Base Metal	0.088	0.376	0.043	0.024	0.005	0.014	0.007	Balance
Weld	0.123	0.681	0.042	0.023	0.005	0.143	0.015	Balance
Membrane	0.135	0.678	0.045	0.027	0.004	0.229	0.031	Balance

3.2 Sampling and Characterization

This section discusses the methodologies adopted for various aspects of this study, including specimen extraction, non-destructive testing (NDT), mechanical testing, and metallurgical characterization. A description of the procedures and techniques utilized in each of these areas is provided in the subsequent sections.

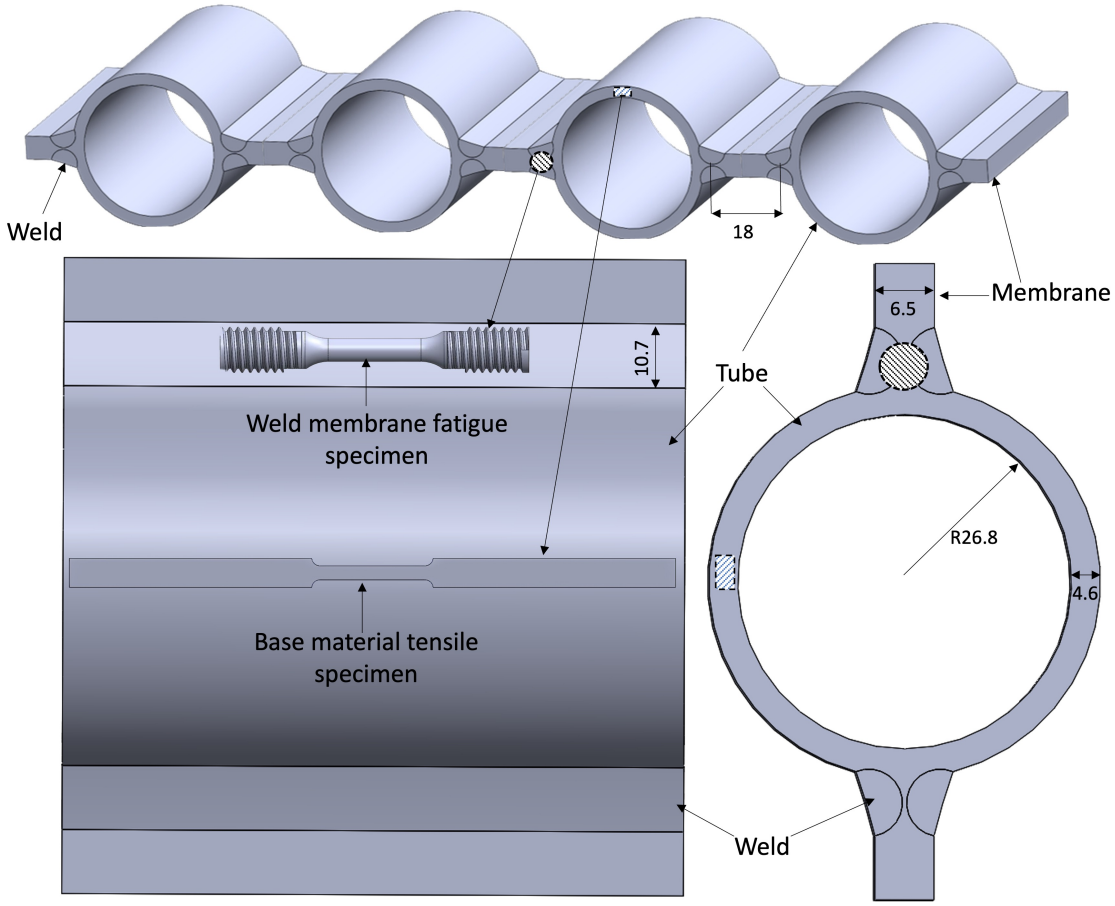

Figure 3.1: Schematic of water walls with the location of test specimens (all dimensions are in mm)

3.2.1 Specimen Extraction

In the present study, the water walls under investigation were constructed using tubes having an external diameter of 62.8 mm and a thickness of 4.6 mm. These tubes were interconnected by an 18 mm thick weld membrane. To evaluate the mechanical properties of the water walls, specimens were extracted from various locations in the axial direction. Tensile tests were conducted on the specimens obtained from both the tubular and welded membrane regions, while fatigue tests were conducted only on the specimens extracted from the welded membrane regions in the axial direction. Figure 3.1 provided a detailed description of the precise locations and orientations for all the specimens.

3.2.2 Non-Destructive Testing

A Zeiss Xradia Versa 620 X-Ray Microscope was used to perform XCT nano scans. XCT is a non-destructive imaging technique that utilizes X-rays to generate high-resolution 3D images of the test specimen. The resolution in an XCT scan referred to the smallest features that could be reconstructed from the 3D voxel data, and in this study, the smallest defect size observed in the water wall specimens was about 20 μm. Therefore, features greater than 20 μm in size were considered defects. The maximum volume that could be examined was 50 $\times$ 50 $\times$ 100 mm^3. DragonFly Pro software version 2021.3.0.1069 was used as a tool for the region of interest (ROI) segmentation. The ROI segmentation algorithm defined the material boundary by selecting the air pixels from the scan and subtracting those pixels from the overall scan to generate a model with internal defects. A meshed structure, which was a collection of small, interconnected polygons representing the surface of an object, was generated based on the refined ROI. The meshed structure was then exported in the STL (.stl) file format for further finite-element analysis. Post-processing and analysis of images were used to differentiate the test specimens as defective and defect-free specimens. This process involved analyzing the 3D images generated by the XCT scans to identify the presence of defects in the water wall specimens.

3.2.3 Tensile Testing

Tensile specimens were extracted from the axial direction of the water walls in accordance with ASTM E8/E8M [93]. Due to the limited thickness of the tube, flat dog-boned-shaped tensile specimens were machined to evaluate the properties of the base material. Additionally, another set of defect-free water wall specimens from the base material was machined with two notches of 45°-0.20 mm radius to evaluate the effect of the notch (Figure 3.2).

Furthermore, round tensile specimens were machined from the weld toe areas of the water wall membrane as shown in Figure 3.3. These specimens were composite

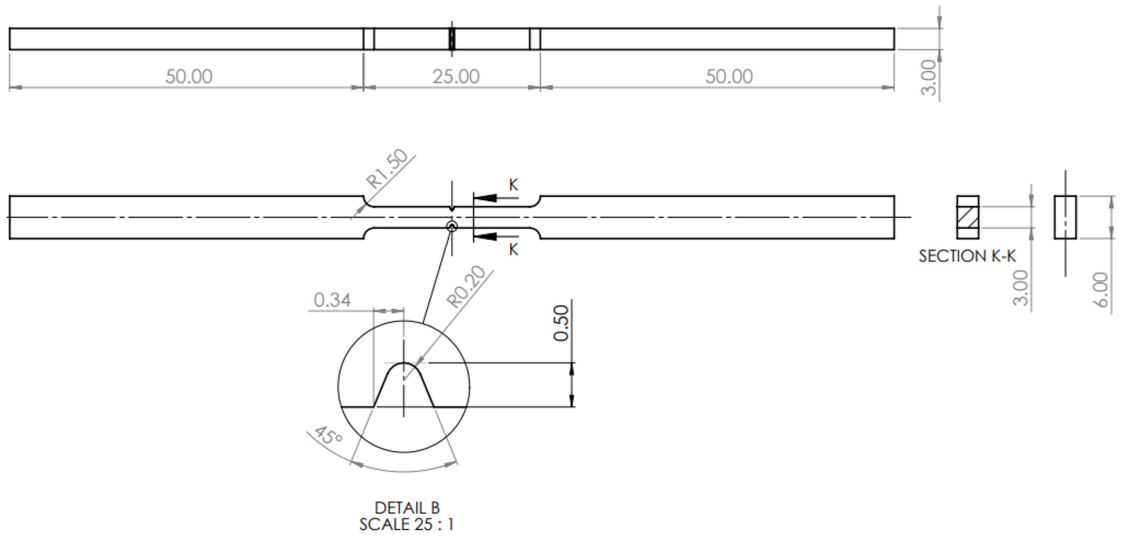

Figure 3.2: Dimensions of the notched tensile base material specimens extracted from water walls (all dimensions are in mm)

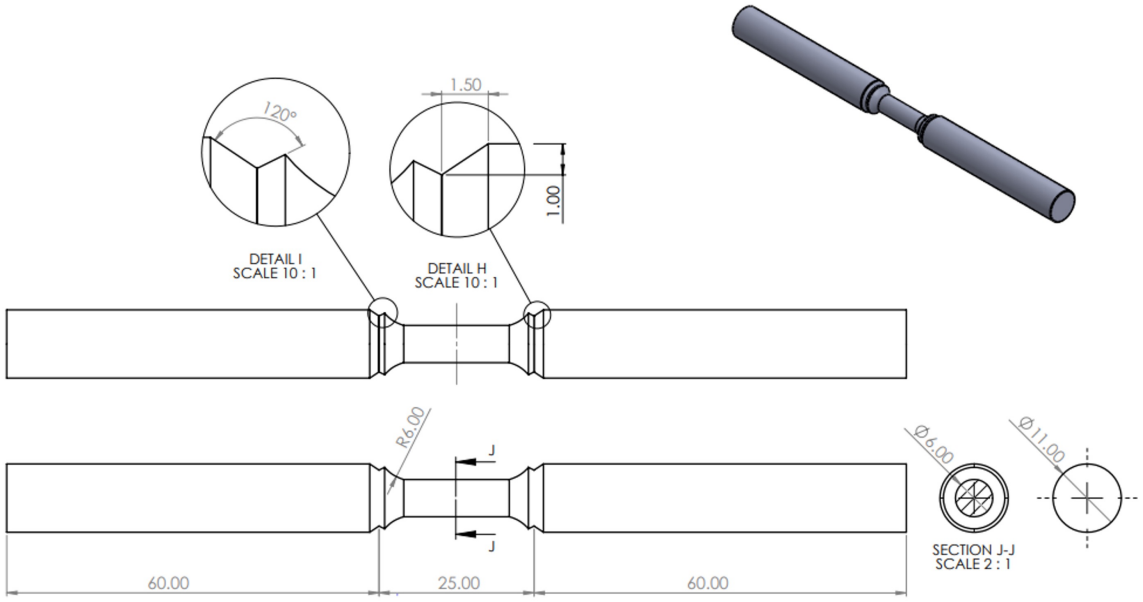

Figure 3.3: Dimensions of round tensile welded membrane specimens (all dimensions are in mm)

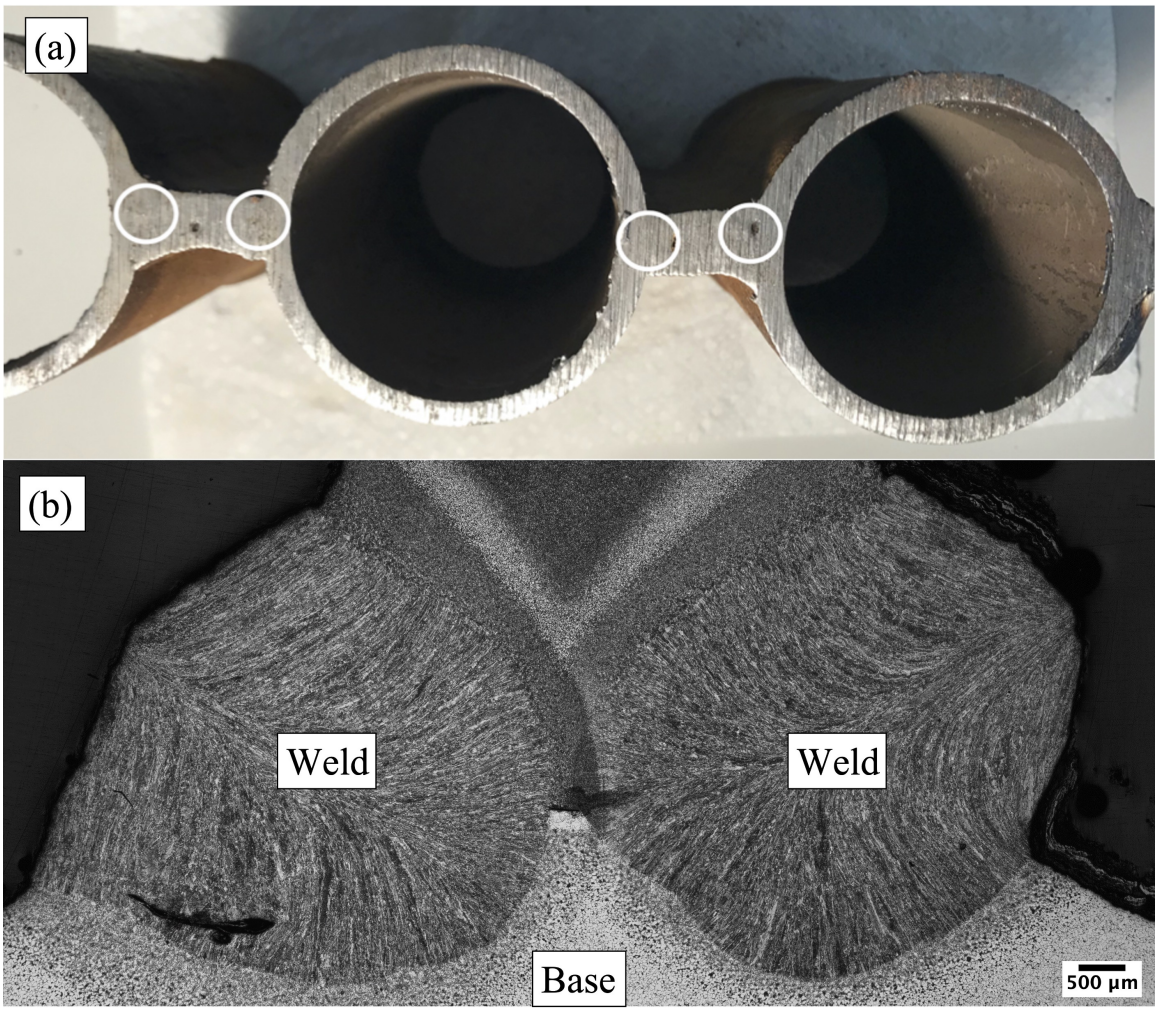

Figure 3.4: (a) Section of water walls showing extraction locations of round tensile specimens for welded membrane samples and (b) Macrograph of extraction site for welded membrane specimens

in nature and consisted partially of some welds, some tube substrates, and some membrane inserts as shown in Figure 3.4. All but one of the round tensile specimens contained lack-of-fusion and inclusion defects, with some of these defects exposed on the surface and some located internally.

To initiate preloading at room temperature, the specimens were loaded to the target stress level at a rate of 1 kN/min and subsequently unloaded. Following the preloading process, the specimens were tested to failure at 300°C, which corresponded to the operational temperature of the water walls during service. For the high-temperature testing, the specimens were gradually heated to 300°C at a rate of 5°C/sec using an MTS 653 Furnace and maintained at that temperature for 15 minutes for thermal stabilization before loading to fracture. All high-temperature tensile tests were conducted using a single ramp waveform with a displacement rate of 1 mm/min under displacement control. Data was recorded at a rate of 10 data points per second. The tensile properties such as Yield Strength (YS), Ultimate Tensile Strength (UTS), Young's Modulus (E), and Percentage Elongation were determined from the generated stress-strain curves. The YS was determined by the corresponding stress at 0.2% strain offset, while the maximum stress in the stress-strain curve was considered the UTS.

3.2.4 Fatigue Testing

Fatigue test specimens were obtained from the weld toe regions of the water wall membranes in accordance with ASTM E606 [34], as shown in Figure 3.5. These specimens were composite in nature, comprising welds, tube substrates, and membrane inserts. High-temperature low-cycle fatigue testing was carried out using an MTS Landmark servo-hydraulic test system coupled with a MTS-653 furnace. To prepare for fatigue testing, the circumferential surface of the specimens was smoothed using #1200 grit sandpapers. The fatigue tests were conducted at 300°C using a strain-controlled sinusoidal loading waveform with a frequency of 0.1 Hz. The heating rate

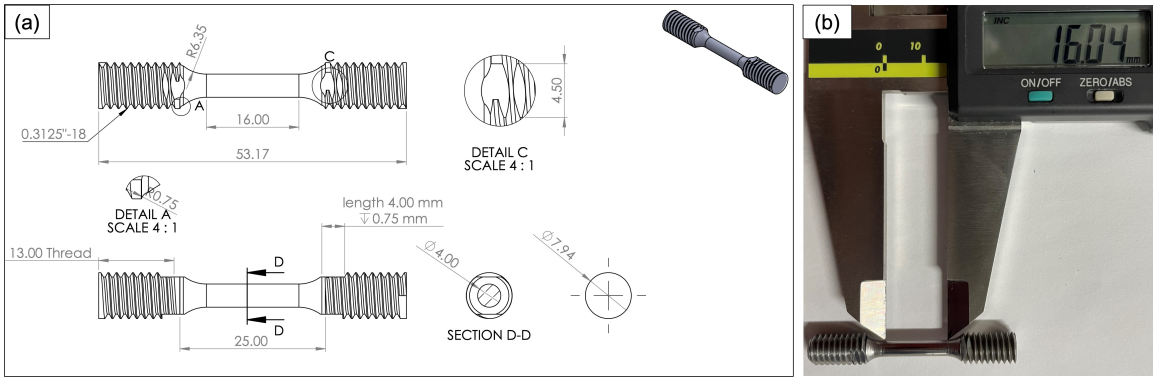

Figure 3.5: (a) Dimensions of fatigue specimen extracted from water walls (all dimensions are in mm) and (b) An image showing the fatigue specimen

was 5°C/sec using an MTS 653 Furnace, and the soaking time was 60 minutes to achieve thermal equilibrium. The strain levels were maintained between 0% and the target strain level. The termination criteria for the fatigue tests were defined as the peak and valley stress dropping by more than 20% compared to the stable cycle value.

3.2.5 Hardness Testing

Micro-hardness measurements were conducted on the cross-section of the weld membrane specimen to evaluate the local hardness variations. The micro-hardness measurements were performed using a Wilson VH3100 hardness tester with Minuteman software. The surface finish of the cross-section was prepared to 0.25 μm, and a 0.05 kgf load was applied to the indenter with a dwell time of 10 s. The spacing between hardness points was maintained at a minimum of 2.5 times the size of the indent to reduce measurement errors. The size of each micro-hardness indent was measured and converted into Vickers pyramid number (HV) using Minuteman software. To obtain an average hardness distribution, a hardness heat map was generated for each section of the weld composite specimen. These micro-hardness measurements provided local mechanical properties of the weld and were used to correlate with the macroscopic fatigue properties of the weld membrane specimen.

3.2.6 Optical Microscopy

To investigate the microstructure of the specimens, the tensile and fatigue specimens were mounted onto a sample holder and ground using SiC sandpapers with grit sizes of 80, 180, 320, 600, and 1200. Diamond and alumina suspensions of 3 μm, 1 μm, 0.5 μm, and 0.05 μm were used for polishing. A colloidal silica solution with a particle size of 0.02 μm was used for the final polishing step. The polished surface was etched with 4% Nital to reveal the microstructure. Optical examinations were performed using two different microscopes: the Nikon Eclipse MA200 Inverted Microscope and Olympus BX53 Upright Metallurgical Microscope.

3.2.7 Scanning Electron Microscopy (SEM)

Fractography analysis was carried out using a Vega3 Tescan SEM. The secondary electron (SE) imaging mode with an accelerating voltage of 20 kV and a working distance of 10 mm was used. For further analysis, a Zeiss Sigma field emission scanning electron microscopy (FE-SEM) with a 30 μm aperture and an accelerating voltage of 10–20 kV was used. The imaging modes used were in-lens secondary electron (in-lens), SE, and backscattered electron (BSE) imaging modes. For SEM with energy-dispersive spectroscopy (EDS), a surface finish of 0.25 μm was required, whereas a finish of 0.05 μm was needed for electron backscatter diffraction (EBSD).

3.2.8 Energy Dispersive X-ray Spectroscopy (EDS)

EDS was used for accurate phase identification and fast elemental/phase mapping. This was achieved by integrating the FE-SEM with an Oxford Instruments X-Max 150 detector and Oxford AztecSynergy software Version 2.4 for data acquisition and analysis. A 30 μm aperture and an accelerating voltage of 20 kV were applied for this application. A Zeiss Sigma FE-SEM equipped with an Oxford Instruments X-Max 150 detector and Oxford AztecSynergy Software Version 2.4 was used for data acquisition and analysis. The EDS analysis was performed at an accelerating voltage

of 20 kV, and a 30 μm aperture was used.

3.2.9 Electron Backscatter Diffraction (EBSD)

The study utilized EBSD for crystallographic misorientation characterization. This was accomplished by integrating the FE-SEM with an Oxford Instruments NordlysNano detector and Oxford AztecSynergy software Version 2.4 for data acquisition. For this application, a 60 μm aperture, an accelerating voltage of 20 kV, and a tilt of 70°were used. EBSD scans were taken at a step size of 0.5 μm at several locations and magnifications to obtain representative images of the microstructure. EBSD data processing, including reconstructed maps, was carried out using Channel5 data processing software.

3.3 Finite Element Analysis (FEA)

In this study, various finite element analyses were conducted to simulate different loading scenarios on the water walls. The first simulation involved hydrostatic pressure, which was used to determine the response of the material to the pressure exerted during the hydrostatic test. Preloading simulations were also conducted to simulate the stress-strain behavior of the material when subjected to a certain amount of load prior to actual loading. In-phase thermo-mechanical loading simulations were carried out to determine how the material behaved under the combined effects of temperature and mechanical loading.

Furthermore, fatigue damage simulation was performed to study the accumulation of fatigue damage on the material over time and predict the life cycle of the material. This was followed by a fatigue crack propagation simulation to determine how cracks propagated in the material under cyclic loading conditions. All these simulations were performed using ABAQUS® in conjunction with the ANSYS® Workbench simulation platform. It should be noted that all the units used in the simulations were in the metric system as part of the SI units.

3.4 Summary

This chapter provided a detailed account of the experimental techniques used for the extraction, machining, preparation, processing, and analysis of water wall specimens. It described the procedures for specimen extraction from the weld toe regions and their composite nature. Testing was conducted using a MTS Landmark servo-hydraulic test system coupled with an MTS-653 furnace for high-temperature tensile and fatigue testing.

Micro-hardness measurements were performed using a Wilson VH3100 hardness tester, and the resulting heat map was generated. The microstructure of the specimens was characterized using polishing, etching, and optical microscopes. Fractography analysis was conducted using SEM imaging, and EDS was used for phase identification and elemental mapping. EBSD was utilized for crystallographic misorientation characterization.

FEA was employed to analyze the water walls under different loading scenarios, establishing fatigue damage and crack propagation parameters for predicting fatigue life and crack propagation. The results obtained from these techniques were presented in subsequent chapters (Chapter 4, 5, and 6) of this research.

Chapter 4

Effects of hydrostatic preload on strain hardening and strain aging of water walls

4.1 Introductiion

In this chapter, the primary focus has been on investigating the influence of hydrostatic preload on water walls containing defects. The central objective is to establish a test methodology that could simulate hydrostatic preload within the context of uniaxial loading conditions. This methodology aims to assess the effects of hydrostatic testing on specimens that already contain defects. The approach integrates both experimental and numerical components to analyze the occurrence of strain hardening and strain aging at an operational temperature of 300°C for water walls. It aims to provide a better understanding of the impact of hydrostatic testing on water walls with weld defects and to develop a more effective testing methodology to prevent premature failures. The results of this study can contribute to the development of more effective hydrostatic testing protocols and can help ensure the safe operation of boilers in various industrial settings.

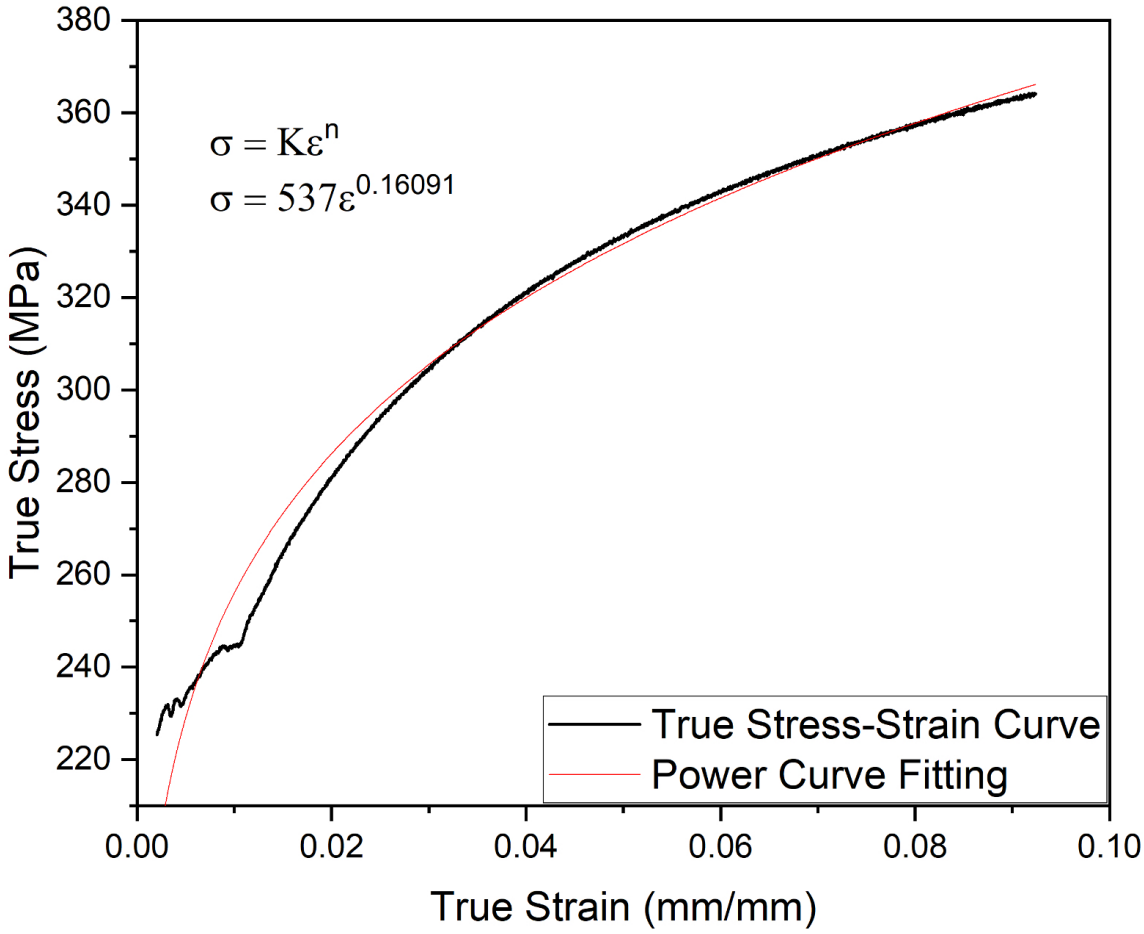

Figure 4.1: Ludwik–Hollomon hardening law fitted to measured true stress-strain curve of the base material

4.2 Experimental and Simulation Methodology

The focus of the study was on evaluating the properties of the base material, weld material, and welded membrane at room temperature. To achieve this, tensile tests were performed on the welded membrane and base metal, and the obtained stress-strain data was analyzed. To determine the properties of the weld material, the rule of mixtures was employed using stress-strain data from both the welded membrane and base metal. The Ludwik-Hollomon hardening law was utilized to fit the stress-strain data of the base metal, as shown in Figure 4.1

$$\sigma_{\mathrm{b}} = K\epsilon_{\mathrm{b}}^{\mathrm{n}}, \tag{4.1}$$

where σ_b, ϵ_b, K, and n are the *true stress*, *true strain*, *strength coefficient* and *strain hardening exponents* of the base metal, respectively. Engineering stress-strain was converted to true stress-strain. For the welded membrane, the total load on the specimen, F, can be represented as

$$F = \sigma_b A_b + \sigma_w A_w, \tag{4.2}$$

A_b and A_w are the cross-sectional areas of the base metal and the weld. As the hardening behaviour of the weld metal varies across its cross-section, so will the stress. Hence, average stress σ_w was used in equation 4.2. Rearranging equation 4.2 yields the following:

$$\sigma_w = \frac{F - \left(K\epsilon_b^n\right)A_b}{A_w} \tag{4.3}$$

Longitudinal strain is assumed to be uniform across the welded membrane for both weld and base material, such that

$$\epsilon_w = \epsilon_b, \tag{4.4}$$

Thus equation 4.3 can be rewritten as

$$\sigma_w = \frac{F - \left(K\epsilon_w^n\right)A_b}{A_w} \tag{4.5}$$

The Young's modulus was determined using the equation

$$E_w = \frac{E_{\text{composite}} - \left(1 - \frac{A_w}{A_w + A_b}\right)E_b}{\frac{A_w}{A_w + A_b}} \tag{4.6}$$

where, E_w, E_b , and $E_{\text{composite}}$ are Young's modulus of the weld, base, and welded membrane, respectively. The stress-strain relation of the weld is strongly dependent on the estimation of A_b and A_w which was accomplished using direct measurements of the metallographic sections, processed using ImageJ as shown in Figure 4.2. The

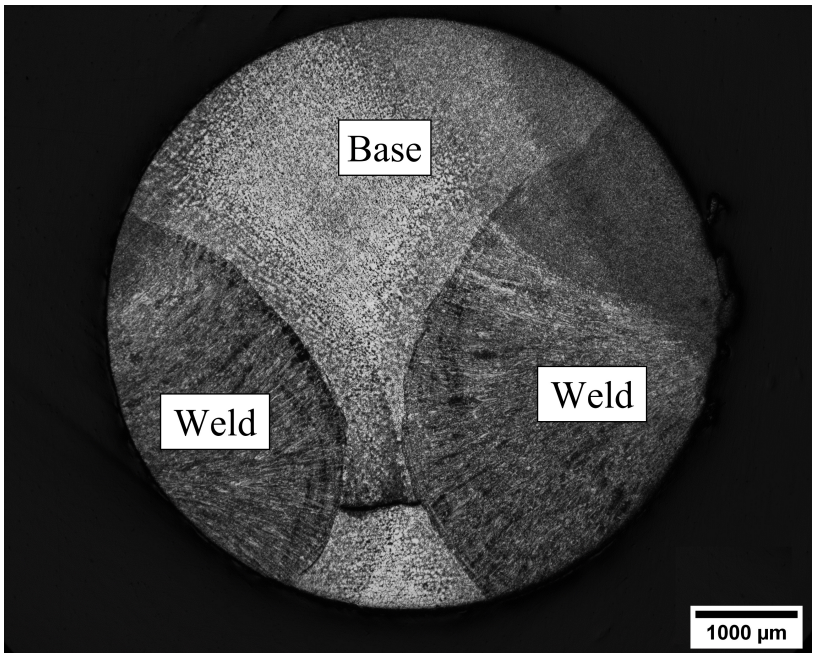

Figure 4.2: Cross-section of water wall welded membrane tensile specimen.

cross-sectional areas of the weld and base metal were estimated to be 15.7 mm^2 and 12.1 mm^2, respectively.

The ANSYS® Workbench simulation platform was used to model the equivalent stress in water walls for the purpose of simulating hydrostatic pressure through uni-axial tensile testing. The simulation was carried out using Ansys Static Structural simulation, with stress levels applied at 150% and 100% of the maximum allowable working pressure (MAWP), which were 1448 psi and 965 psi, respectively. Room temperature base and weld material properties were assigned to the 3-D water wall model. The simulations utilized a multi-linear plasticity hardening model, and the balance of the linear momentum equation of the 3-D model could be expressed as follows:

$$\frac{\partial \sigma_{\mathrm{ij}}}{\partial x_{\mathrm{j}}} + \rho b_{\mathrm{i}} = \rho a_{\mathrm{i}}, \tag{4.7}$$

where ρ is the density, σ_{ij} is the Cauchy stress tensor, b_{i} is the body force in the i-direction and a_{i} is the acceleration in the i-direction. During static analysis, a_{i} is considered as 0. For the elastic-plastic constitutive law, the material is assumed to be

isotropic and Hooke's law for isotropic materials is used. In ANSYS, the multi-linear isotropic hardening rule, also known as MISO, is a rate-independent plasticity model characterized by von Mises yield criteria and isotropic hardening, in which the yield surface remains centred in its centerline and expands when plastic strain develops [94][95]:

$$\bar{\sigma} = K(\bar{\epsilon} + \epsilon_{\mathrm{o}})^{\mathrm{n}} \tag{4.8}$$

where $\bar{\sigma}$ and $\bar{\epsilon}$ are the equivalent stress and equivalent plastic strain, respectively, and K, n and ϵ_{o} are material constants.

Based on the simulation results, a test matrix was developed to evaluate the effect of hydrostatic pressure on water walls containing defects. The purpose of that test matrix was to identify the critical pressure that could lead to the failure of water walls during hydrostatic testing. Table 4.1 outlined the different combinations of factors that were tested to achieve this objective.

4.3 Results

Figure 4.3 shows the engineering stress-strain curves. The tensile properties of the base and welded membrane at room temperature are shown in Table 4.2. Instrumental errors sometimes lead to the reporting of a slightly lower value of Young's Modulus. Hence for further analysis, a conventional value of 200 GPa which is in range with the obtained value has been used.

The tensile properties of the weld are calculated from the rule of mixtures [96][97][98]. Figure 4.4 is a visual representation of the tensile properties of the weld. Experimental stress–strain data for the base metal and the welded membrane are the lower two curves. The upper-most curve is the calculated stress–strain curve for the weld. The calculated properties of the weld have been used as input for the simulation of the water walls at 150% and 100% of MAWP.

Table 4.1: Test matrix to study the effects of preload on strain hardening and strain aging

Sample Type	**Sample ID**	**Test Condition**	**Defect Type**
Smooth (Base Material)	S-0 PL	No room temperature preload. Tensile tested at 300°C.	No defects
	S-53 PL	53 MPa room temperature preload. Tensile tested at 300°C.	No defects
	S-95 PL	95 MPa room temperature preload. Tensile tested at 300°C.	No defects
Notched (Base Material)	N-0 PL	No room temperature preload. Tensile tested at 300°C.	Notch
	N-53 PL	53 MPa room temperature preload. Tensile tested at 300°C.	Notch
	N-95 PL	95 MPa room temperature preload. Tensile tested at 300°C.	Notch
Welded Membrane (Base Material + Weld)	WC-0 PL	No room temperature preload. Tensile tested at 300°C.	Weld defect
	WC-53 PL	53 MPa room temperature preload. Tensile tested at 300°C.	Weld defect
	WC-95 PL #1	95 MPa room temperature preload. Tensile tested at 300°C.	Weld defect
	WC-95 PL #2	95 MPa room temperature preload. Tensile tested at 300°C.	No defects

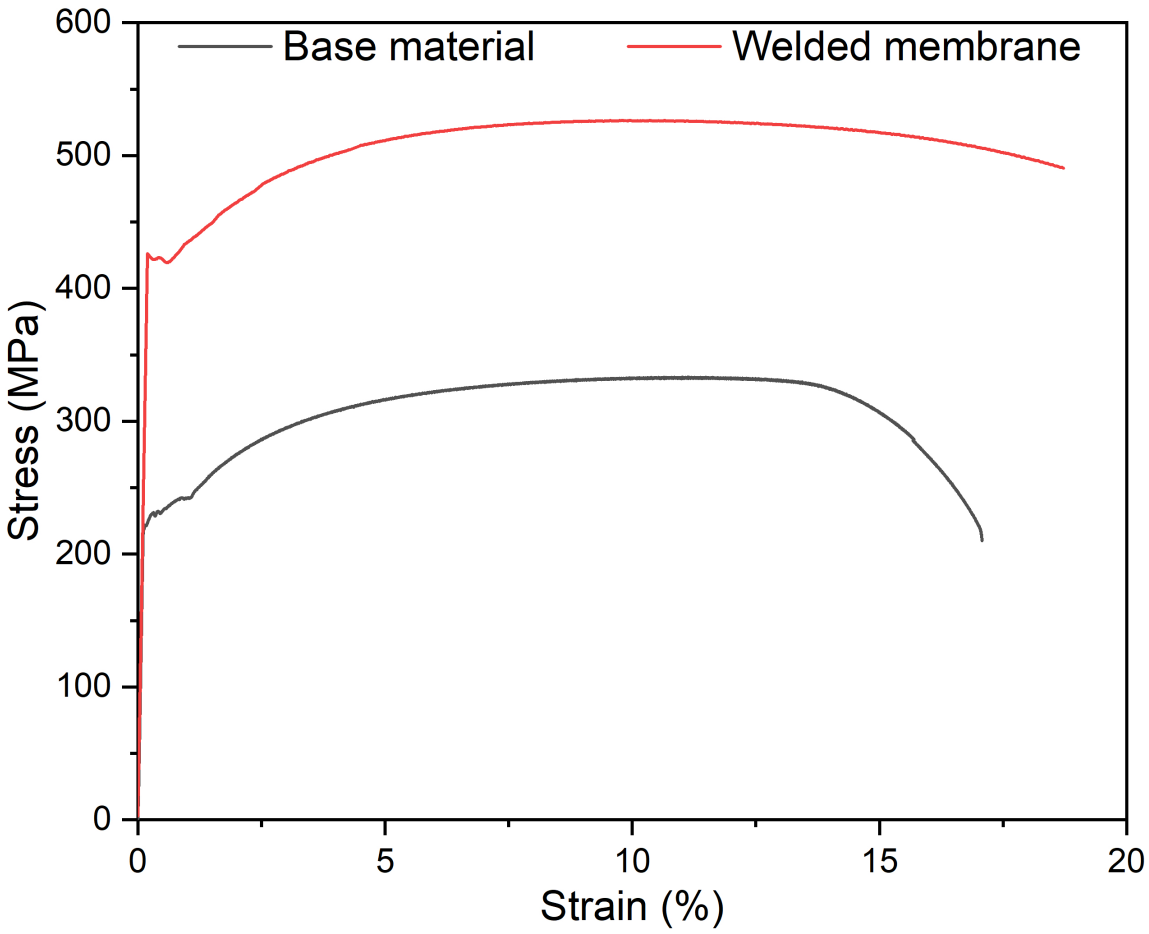

Figure 4.3: Water wall base material specimen and welded membrane specimen tested at room temperature

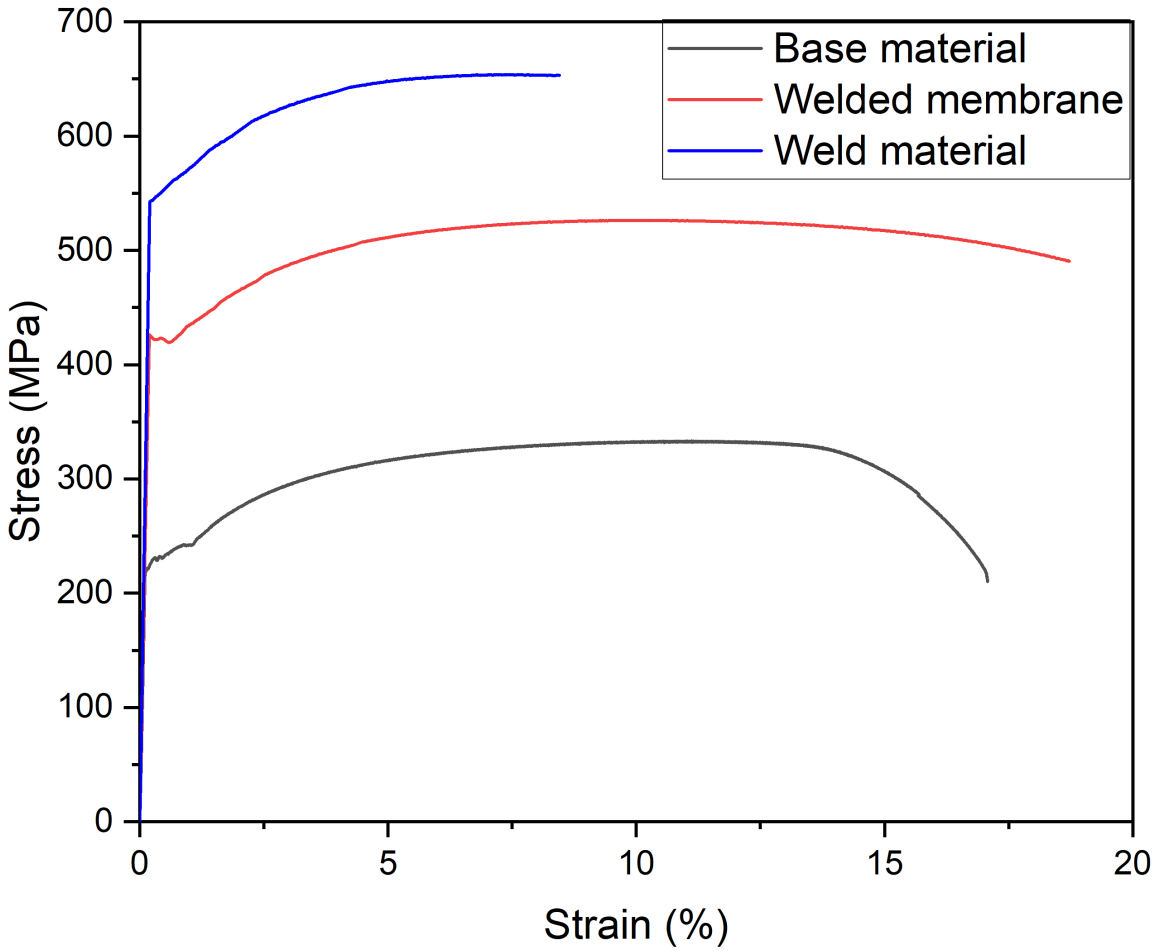

Figure 4.4: Stress-strain curves treated according to the rule of mixtures. The base material and weld material stress-strain curves served as input to the finite element simulation as material properties

Table 4.2: Tensile properties of base material and welded membrane at room temperature

	Yield Strength (MPa)	**Tensile Strength (MPa)**	**Young's Modulus (GPa)**
Base Metal	224	333	186 (Measured)
Welded Membrane	423	526	218

The ANSYS simulation is conducted with TET10 elements with a global size of 1 mm after performing a mesh independence study (Figure 4.5). Evaluation of the equivalent stress in the water walls near the weld toe regions at 150% and 100% of MAWP, results in 95 MPa and 53 MPa, respectively. The results of the equivalent von Mises stress are presented in Figure 4.6, where the color contours display the distribution of stress across the cross-section of the water walls, with the red regions indicating high-stress concentrations. The simulation outcomes reveal that the areas with the highest stress concentrations are located near the inner diameter (ID) and weld toe regions. To simulate the hydrostatic test loading, preloads of 95 MPa and 53 MPa are chosen to correspond to 150% and 100% of hydrostatic pressure, respectively.

Strain hardening and strain aging effects are produced during the room temperature hydrostatic preload. The results show that when the preload is too low to cause local plasticity in the specimen, no strain hardening and strain aging effects are observed. Sample WC-53 PL, which is preloaded to 53 MPa (100% of MAWP) at room temperature and tensile tested at 300°C, exhibits similar mechanical properties to Sample WC-0 PL, which is tested at 300°C without preload. Sample WC-95 PL #1, which is preloaded to 95 MPa (150% of MAWP) at room temperature and tensile tested at 300°C, shows significant strengthening. There is an increase in yield strength and tensile strength by 6.4% and 13%, respectively, when compared with the sample tested at 300°C without preload. However, elongation values don't show any significant changes as the plastic zone created by the preload is very localized and only exists near the pre-existing defects (Figure 4.7) (see Table 4.3).

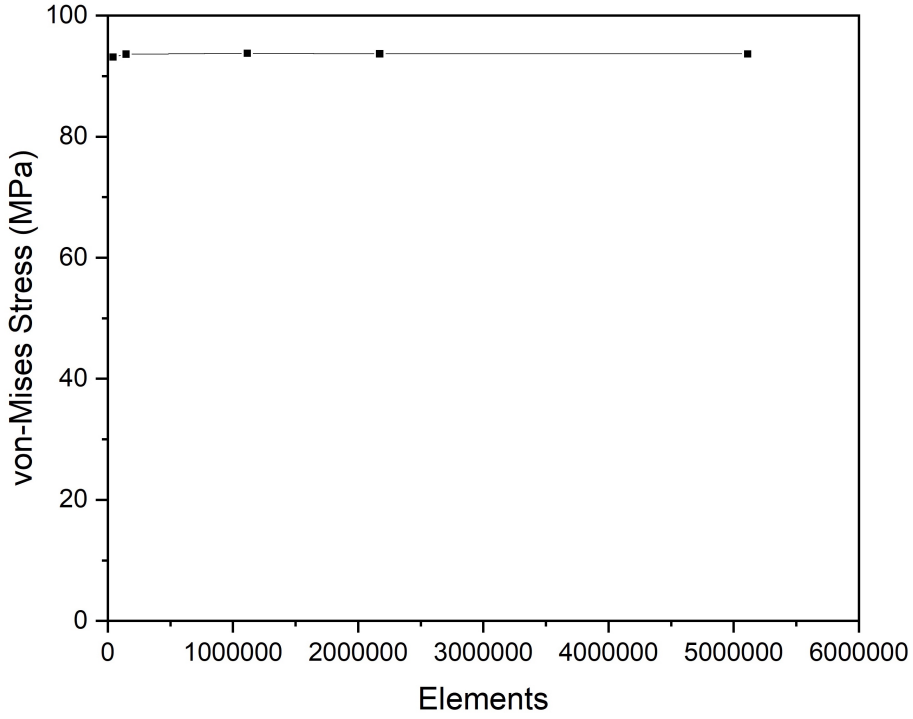

Figure 4.5: Mesh study for von Mises stress in water wall section

Table 4.3: Mechanical properties of welded membrane specimens.

Sample ID	Young's Modulus (GPa)	Yield Strength (MPa)	Tensile Strength (MPa)	Elongation (%)
WC-0 PL	212	420	509	16.0
WC-53 PL	211	370	514	14.2
WC-95 PL #1	208	447	576	16 .0
WC-95 PL #2	210	367	493	16.5

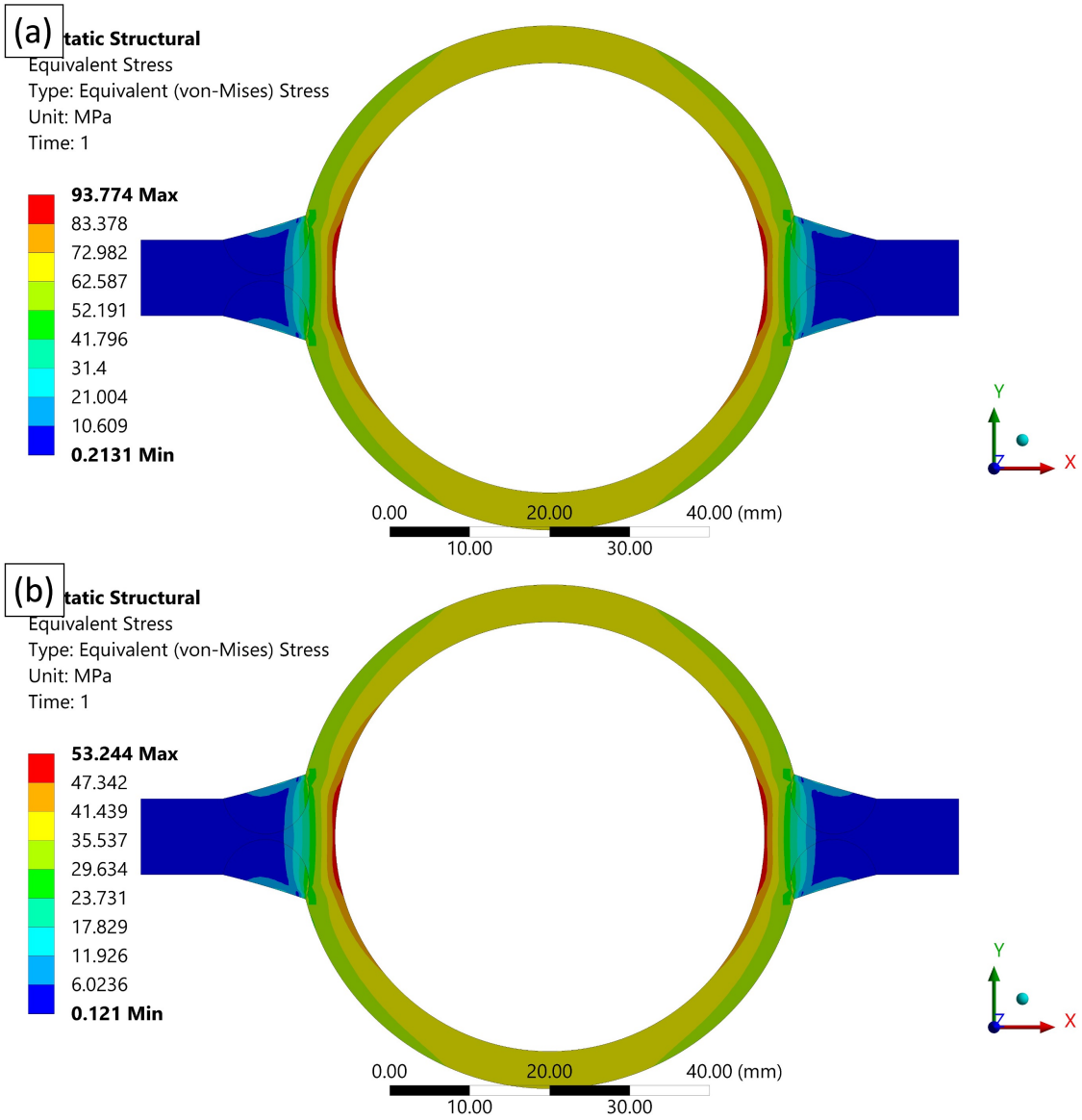

Figure 4.6: (a) Equivalent von Mises stress with 150% of maximum allowable working pressure and (b) Equivalent von Mises stress with 100% of maximum allowable working pressure

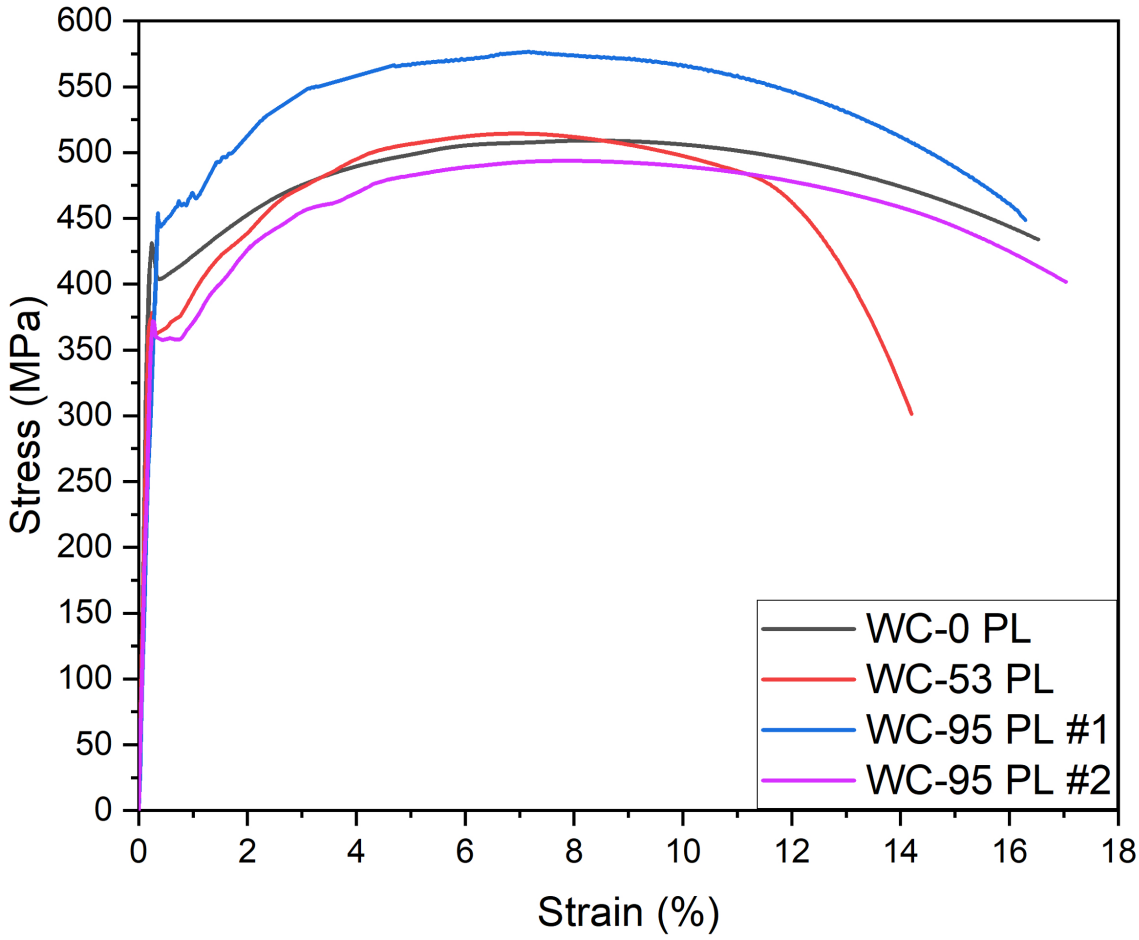

Figure 4.7: Stress-strain curves of the welded membrane specimens

The 95 MPa room temperature preload and subsequent 300°C tensile test are also performed on a welded membrane specimen without any defects (Sample WC-95 PL #2). The results of this test show that there are no significant strain hardening and strain aging effects observed, and the mechanical properties are similar to those of the sample tested at 300°C without preload. This indicates that the observed strengthening effect in Sample WC-95 PL #1 is mainly due to the presence of pre-existing defects in the specimen, and the plastic zone generated by the preload is localized around these defects.

4.4 Discussion

Experiments are conducted on notched water wall samples to understand the role of defects in generating yielding. A notch of 45° is introduced, and a similar testing methodology is implemented on these samples. ANSYS simulation is performed on these samples at 95 MPa and 53 MPa room temperature preloads. The material in the model is considered isotropic in nature with a uniform load applied to one of the ends, and the other end is considered as a fixed support. TET10 element type with a global mesh size of 0.3 mm is chosen after performing a mesh independence study (Figure 4.8). The study results in the generation of around 1.7% and 0.05% plastic strain near the notch, respectively. However, no plastic strain is observed at the center of the samples, as shown in Figure 4.9.

Microstructural examination of the 95 MPa and 53 MPa room temperature preloaded specimens does not reveal any evident grain distortion near the crack tip. The grains appear equiaxed in shape, as shown in Figure 4.10. The microstructures consist of a ferritic matrix with some lamellar pearlite scattered around the matrix. These findings suggest that the presence of defects, such as the 45° notch, plays a crucial role in generating yielding under the applied loads. The lack of evident grain distortion indicates that the yielding is confined to the local plastic zone near the notch.

The presence of local plasticity in a preloaded specimen was examined through

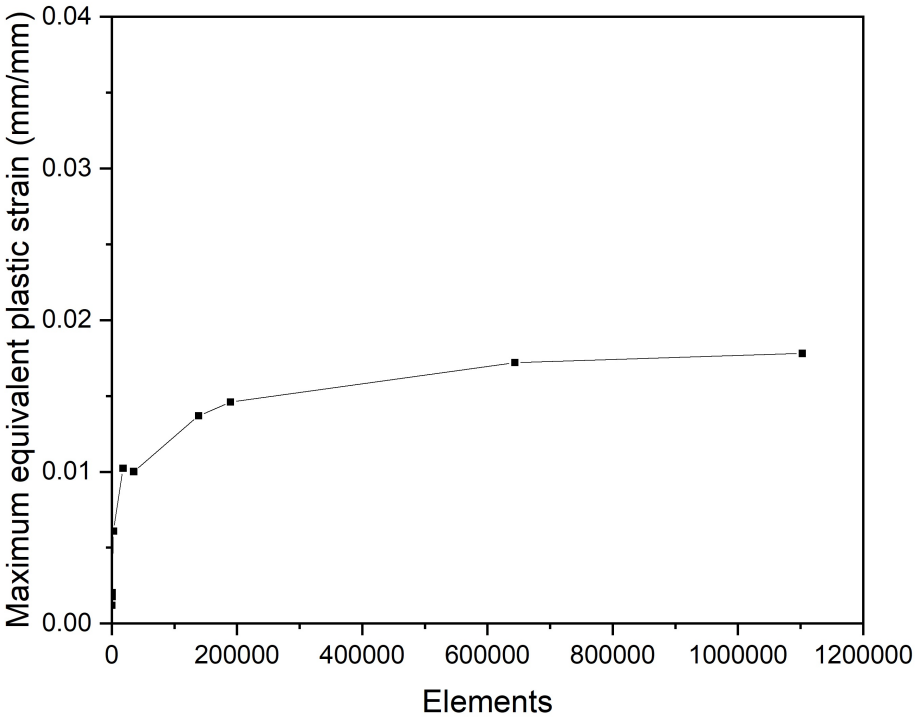

Figure 4.8: Mesh study for plastic strain in notched water wall specimen

EBSD analysis with a step size of 0.5 µm in two regions: one near the notch and the other near the center. The grain orientation spread (GOS) maps were generated using the Oxford Instruments HKL Channel 5 software for both regions. Initially, grain boundaries were determined between two points if the misorientation was greater than 5° between the points. Subsequently, the GOS maps and misorientation distributions of the regions were generated, as depicted in Figure 4.11. The misorientation distribution for both regions could be well characterized by a log-normal distribution. The mean of the log-normal distribution, referred to as modified crystal deformation (MCD), provided a qualitative assessment of the plastic strain in the respective regions [99][100][101][102]. The region near the notch exhibited an MCD value of 1.52°, while the region near the center displayed an MCD value of 0.25°. The substantial difference in the MCD values (a factor of 6) provided a clear indication of local plasticity near the notch, suggesting that plastic deformation was predominantly concentrated in this specific region.

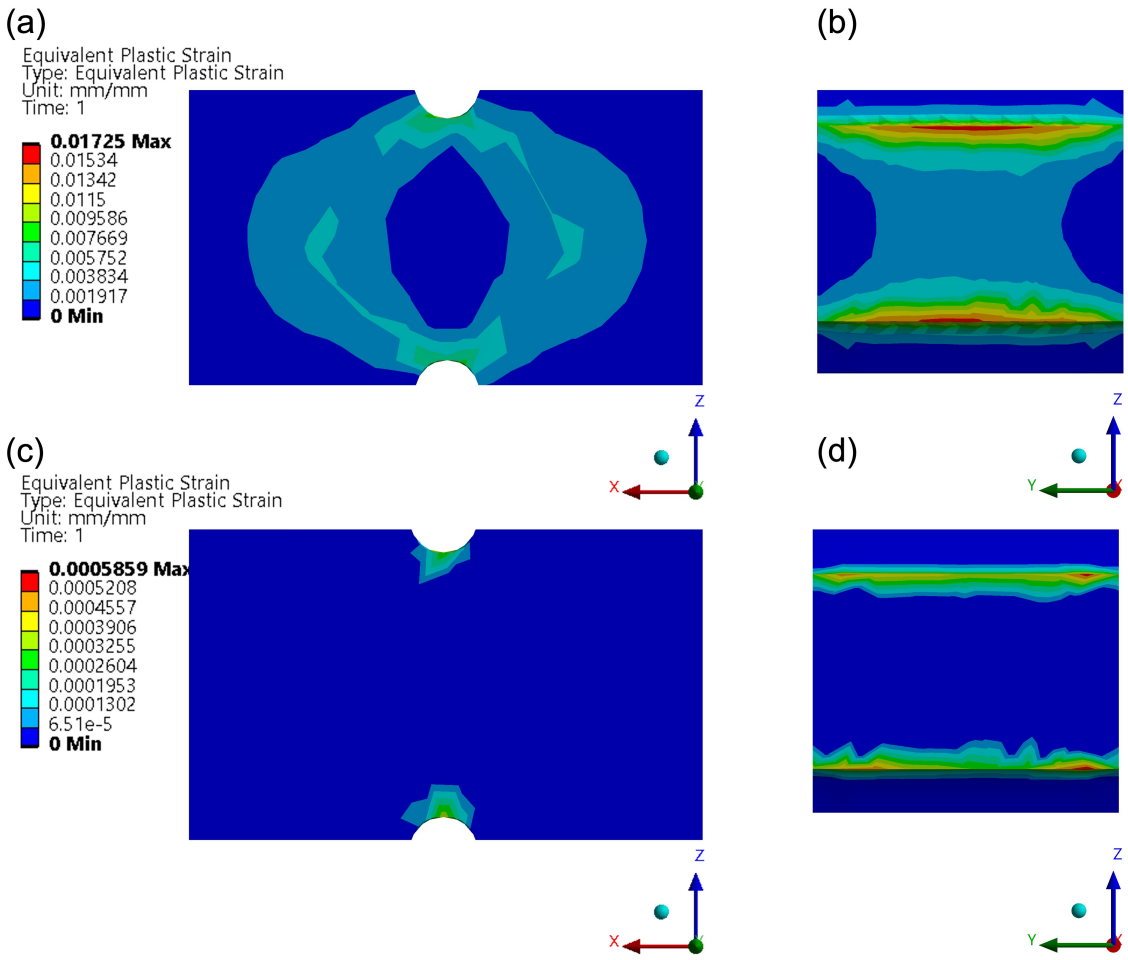

Figure 4.9: (a) Ansys simulation of notched water wall sample with 95 MPa room temperature preload. Maximum 1.7% plastic strain was generated. Equivalent plastic strain at the (X-Z) cross-section, (b) equivalent plastic strain at the (Y-Z) cross-section at the notch, (c) Ansys simulation of notched water wall sample with 53 MPa room temperature preload. Maximum 0.05% plastic strain was generated. Equivalent plastic strain at the (X-Z) cross-section and (d) equivalent plastic strain at the (Y-Z) cross-section at the notch.

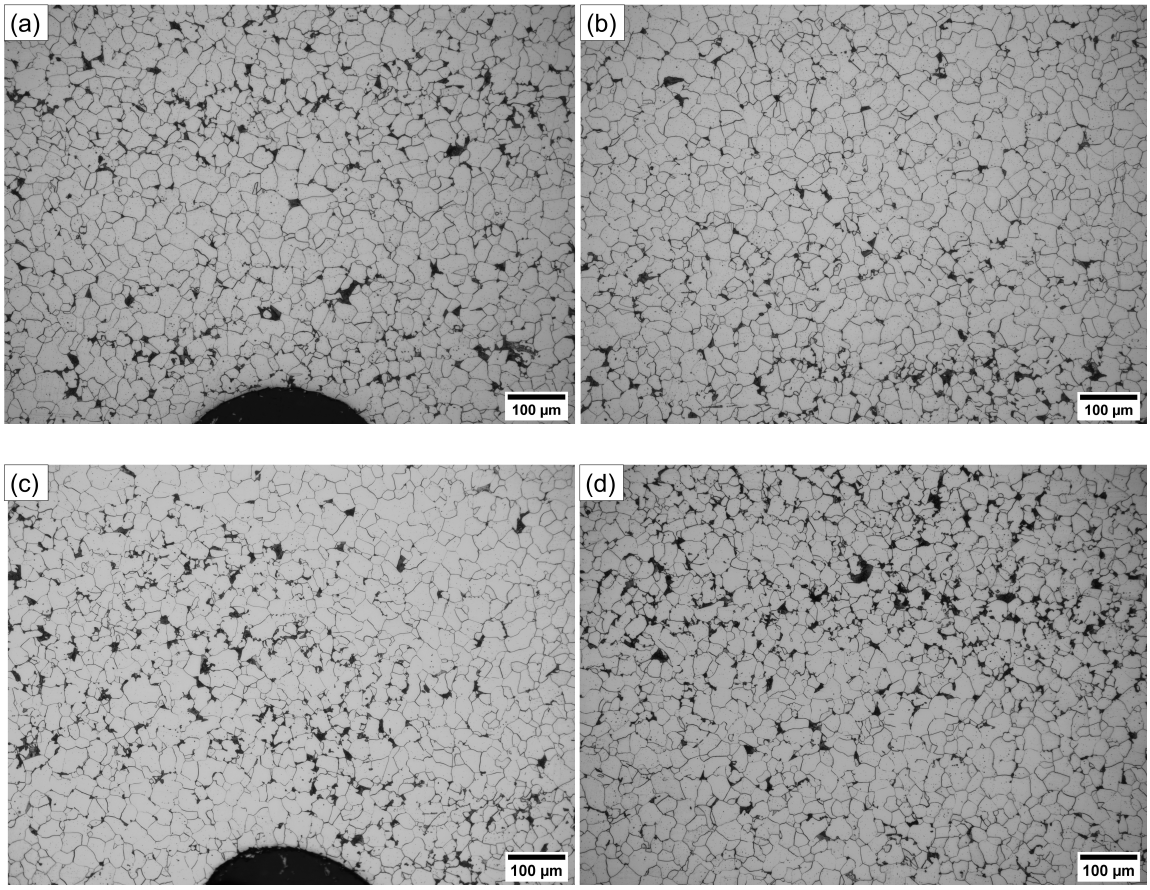

Figure 4.10: (a) Optical microstructure of 95 MPa preloaded notched water wall specimen near the notch, (b) near the center, (c) optical microstructure of 53 MPa preloaded notched water wall specimen near the notch and (d) near the center.

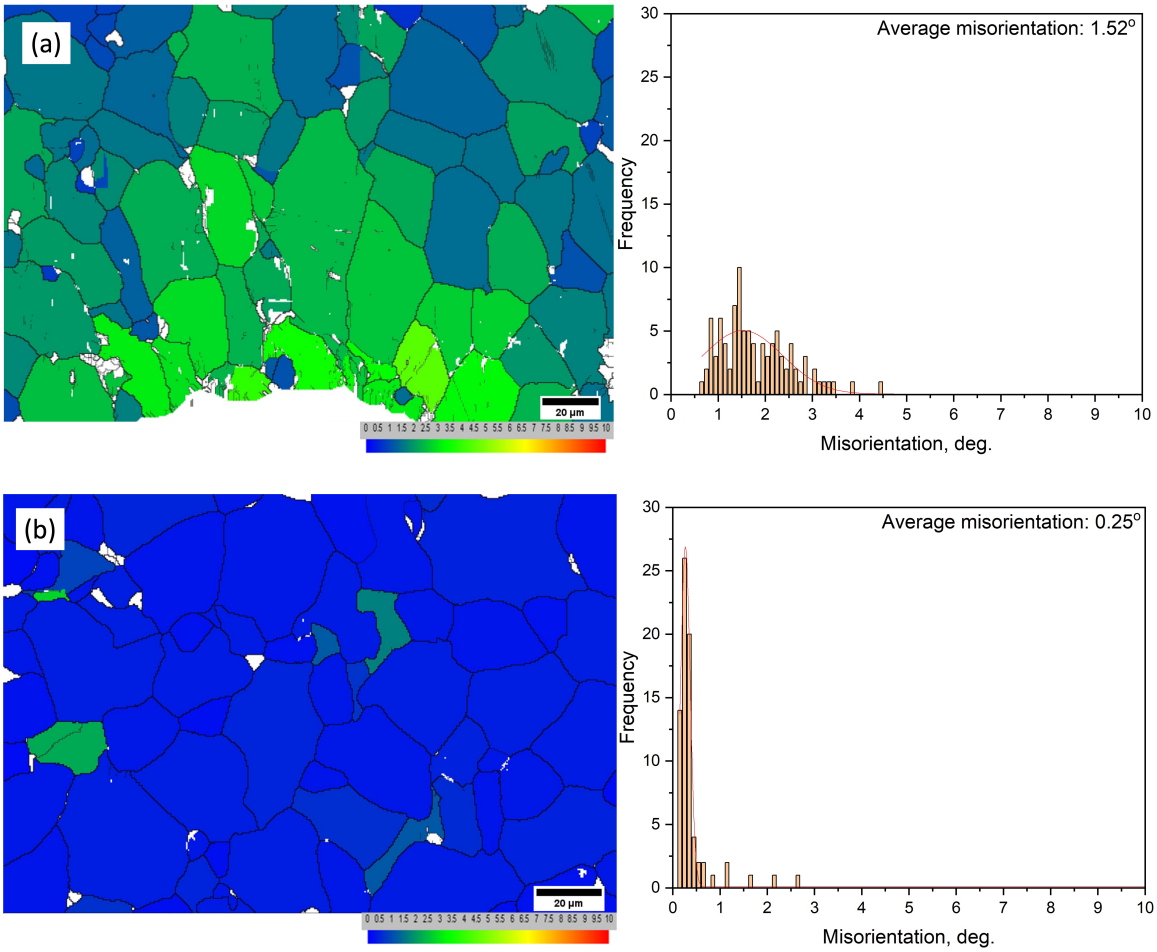

Figure 4.11: Grain orientation spread and grain boundary map of 95 MPa preloaded specimen with misorientation distribution of the EBSD images, (a) near the notch and (b) at the center of specimen cross-section.

The notched water wall specimens that underwent room temperature preload were heated to 300°C and subjected to tensile testing until fracture occurred. Results indicate an increase in tensile strength for Sample N-95 PL, as shown in Figure 4.12 (b). This increase in strength can be attributed to the plastic deformation that occurs during the preload stage, which generates dislocations in the material. As slip continues, high dislocation density regions or tangles are formed, resulting in the creation of a cellular substructure with cell walls containing high-density dislocation tangles.

As the material reaches a saturation point with dislocations, a resistance to the formation of dislocations is observed, leading to a resistance to plastic deformation. These cells eventually become sites for impurity segregation upon reheating, manifesting as strain aging [103][104]. Although strain-hardening effects can be eliminated by fully annealing the material, the operating temperature of water walls is insufficient for full annealing, resulting in the retention of the strain-hardening effects.

Aging of pre-strained material at 300°C facilitates the diffusion of interstitial solute atoms such as carbon and nitrogen to existing dislocations, forming Cottrell atmospheres [105], which are notably affected by aging temperature and time [106]. Cottrell atmospheres are regions of concentrated interstitial solute atoms, such as carbon and nitrogen, that surround a dislocation in a crystal lattice. These atmospheres result from the interaction between solute atoms and dislocations and create a pinning effect that impedes the movement of dislocations. This means that the presence of Cottrell atmospheres in a material makes it harder for dislocations to move and increases its resistance to plastic deformation. The Cottrell-Bilby model defines the rate of strain aging (Equation 4.9) [105].

$$\frac{N(t)}{N_{\mathrm{o}}} = 3n_{\mathrm{o}}\lambda\left(\frac{\pi}{2}^{1/3}\right)\left(\frac{AD}{kT}^{2/3}\right)t^{2/3} \tag{4.9}$$

$N(t)$ is number of solute atoms that diffuses to dislocations, N_{o} is the dislocation density, n_{o} is initial concentration, λ is slip distance of the dislocations, A is the

magnitude of solute-dislocation interactions, D is the diffusion coefficient of the solute atoms, and T is the aging temperature.

Literature states that the solubility limit of carbon in steel increases with an increase in manganese content [107]. This is significant because the formation of Cottrell atmospheres is enhanced by the presence of carbon atoms. Thus, a higher concentration of carbon in a material due to increased solubility can lead to the formation of stronger Cottrell atmospheres. This, in turn, can further increase the material's resistance to plastic deformation [105].

To overcome the resistance to plastic deformation caused by Cottrell atmospheres, new dislocations need to be generated. This requires an increase in the applied stress, which is necessary to break the bonds and create new dislocations. Therefore, the generation and propagation of new dislocations can only occur by increasing the applied stress beyond the yield strength of the material [21][108][109][110].

The tensile test results of Sample N-95 PL indicate a significant increase in tensile strength (Table 4.4), which is attributed to the combined effects of strain hardening and strain aging. The plastic deformation induced by the 95 MPa room temperature preload is inferred to generate dislocations within the material, leading to a dense accumulation of dislocation tangles. As the material becomes saturated with dislocations, a resistance to further plastic deformation becomes evident. This phenomenon gives rise to the formation of a cellular substructure, where cell walls harbour high-density dislocation tangles. These cellular structures later serve as sites for impurity segregation upon reheating.

However, there is no notable alteration in elongation observed in Sample N-95 PL, primarily due to the localized nature of the plastic zone, with dislocation generation confined near the notch. Conversely, Sample N-53 PL does not show any change in properties and exhibited similar properties to Sample N-0 PL. The application of a 53 MPa preload proves inadequate to induce localized plasticity substantial enough to trigger dislocation generation.

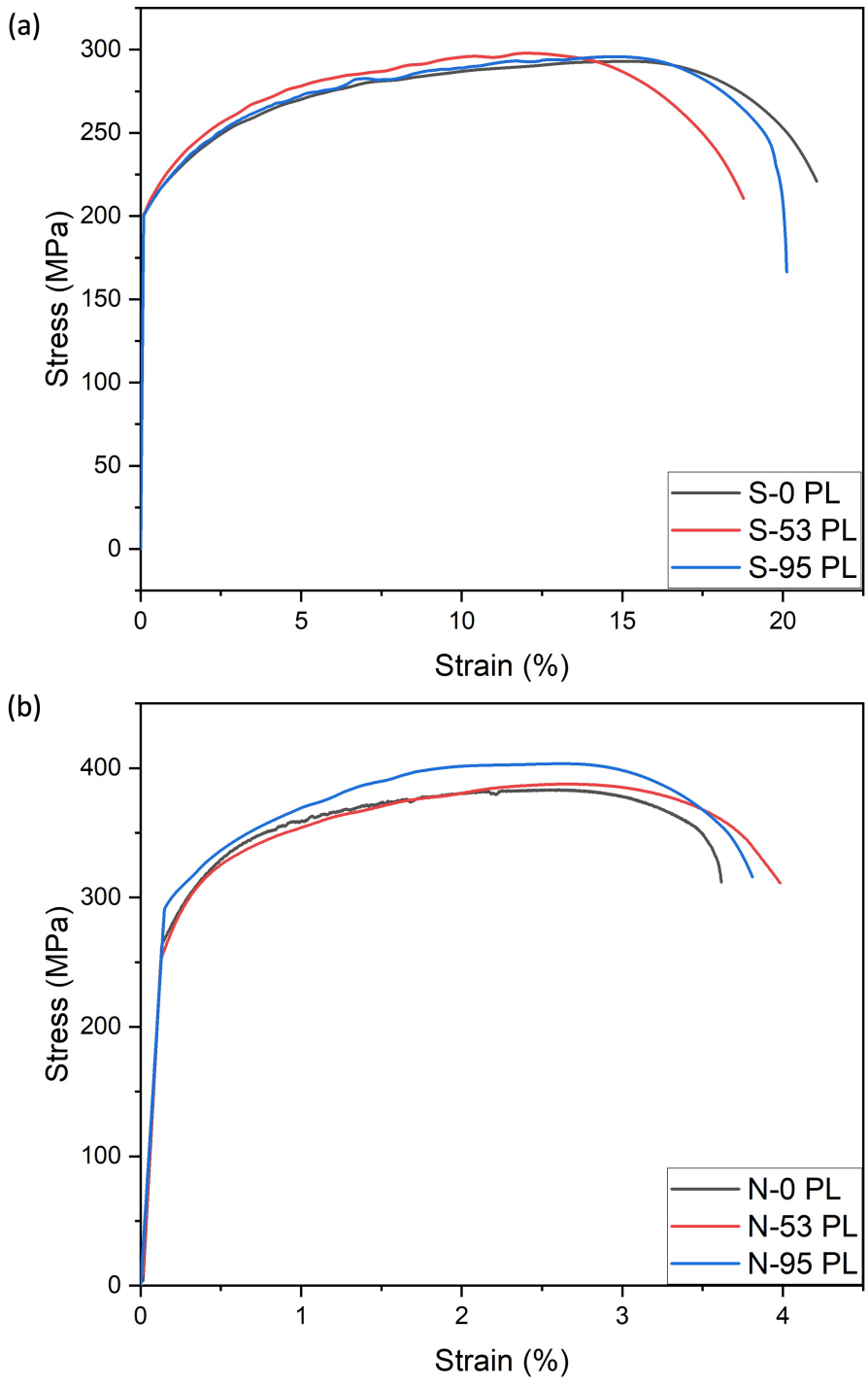

Figure 4.12: (a) Stress-strain curves of the smooth water wall specimens and (b) stress-strain curves of the notched water wall specimens

Table 4.4: Mechanical properties of smooth and notched water wall specimens.

Sample ID	**Yield Strength (MPa)**	**Tensile Strength (MPa)**	**Instrumented Elongation (%)**	**Measured Elongation (%)**
S-0 PL	201	293	21.0	22
S-53 PL	200	297	18.6	21
S-95 PL	200	295	20.1	21
N-0 PL	305	383	3.6	9.6
N-53 PL	306	387	4.1	9.2
N-95 PL	308	404	4	9.4

The smooth water wall samples were tested using the same methodology as the notched specimens. Since the smooth samples do not have a notch, no local plasticity is generated during the 53 MPa and 95 MPa room temperature preloads. These preloads are below the yield strength of the material and do not cause any dislocations in the specimens. Consequently, after the samples are heated to 300°C and subjected to tensile testing, no significant change in strength is observed, as depicted in Figure 4.12 (a). The yield strength and tensile strength are almost the same as the sample tested at 300°C without preload.

The welded membrane specimens used in this study have pre-existing lack-of-fusion defects, which are a result of prior repairs. These defects act as stress raisers during the room temperature hydrostatic preload, leading to the generation of local plasticity near the defects. The dislocations generated near these areas eventually lead to the creation of high-density dislocation tangles. After the sample is reheated to operating temperature and tensile tested to fracture, an increase in yield strength and tensile strength is observed due to the combined effects of strain hardening and strain aging, which are similar to the effects observed with the notched water wall specimens. The angle of these defects is randomly distributed between 0° to 15° relative to the loading direction.

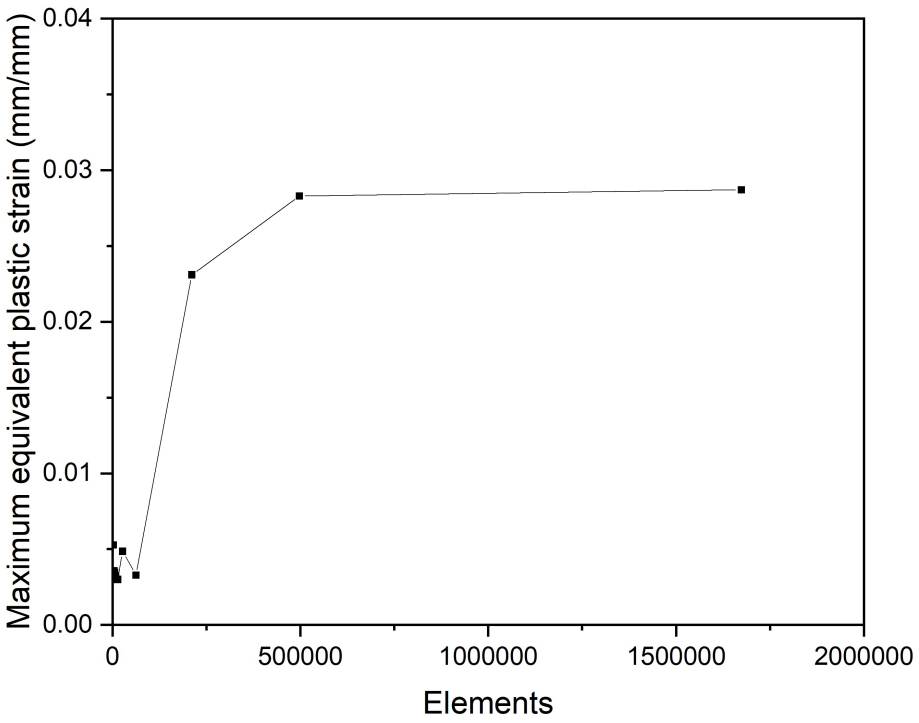

Figure 4.13: Mesh study for plastic strain in weld membrane specimen

From Figure 4.7, it can be observed that Sample WC-95 PL #1 exhibits an increase in both yield and tensile strength. The sample has a lack of fusion slit oriented at 10° to the loading direction, as shown in Figure 4.14. To investigate this behavior, FEA simulation is performed on a model with similar geometry. The input parameters for the model are the material properties of the room-temperature welded membrane. A uniform stress of 95 MPa is applied to one of the ends of the model while keeping the other end fixed. TET10 element type with a global mesh size of 0.15 is considered after performing a mesh independence study (Figure 4.13). The simulation results indicate that around 2.8% of plastic strain (Figure 4.15) is generated near the weld defect, which contributes to significant strain hardening and strain aging of the sample after it is tensile tested at 300°C. This suggests that the lack of fusion defect acts as a stress raiser during the room temperature hydrostatic preload and leads to the generation of local plasticity near the defect, which eventually contributes to the observed increase in strength.

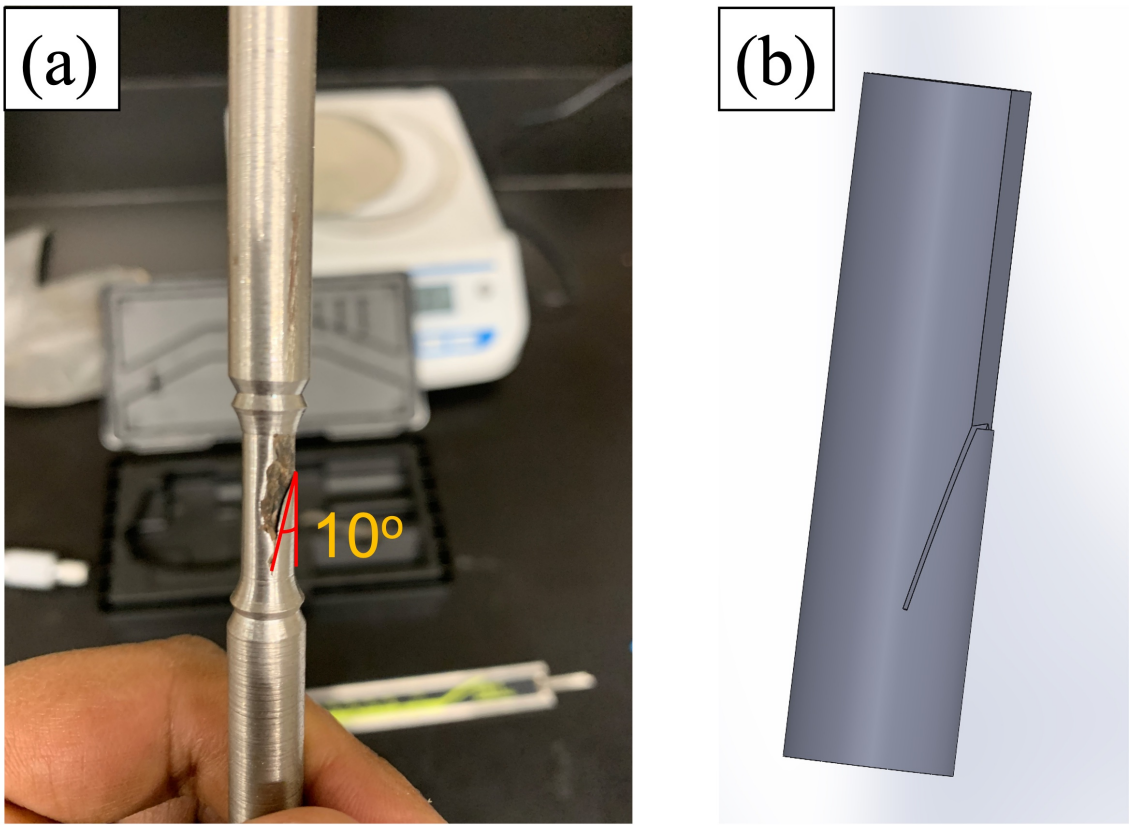

Figure 4.14: (a) Welded membrane sample with defects (Sample WC-95 PL #1) and (b) model of the sample with defects at 10° relative to loading direction

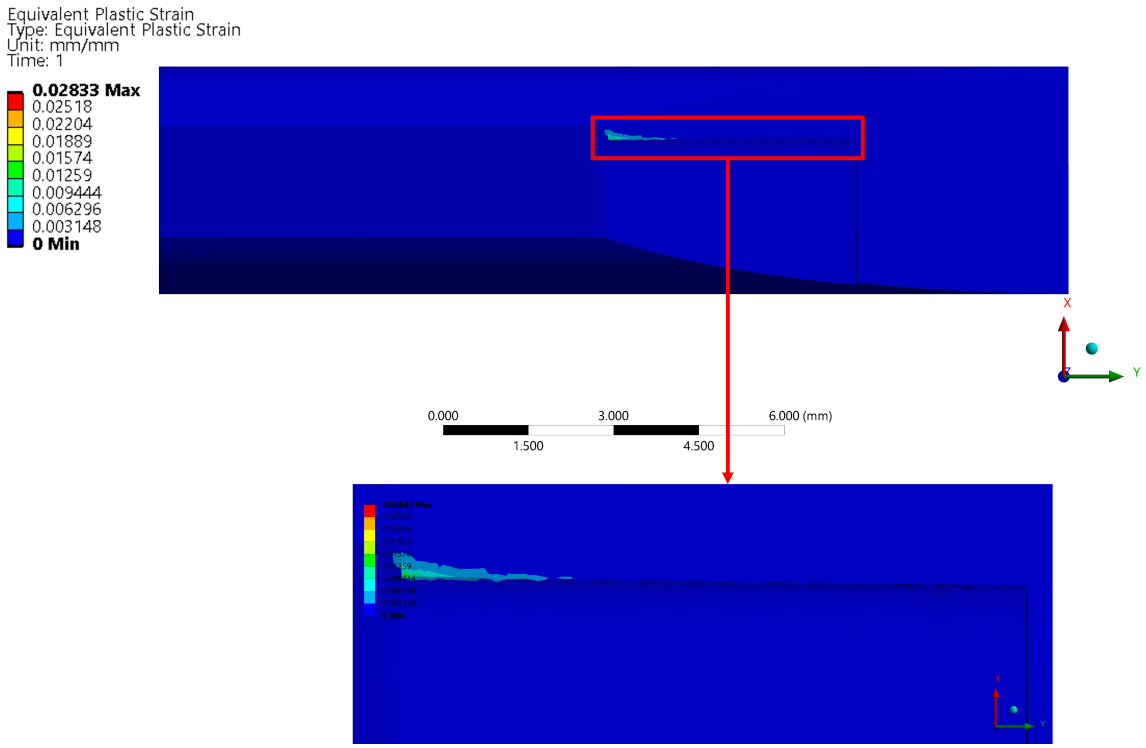

Figure 4.15: Strain distribution in water wall welded membrane specimen (Sample WC-95 PL #1) loaded to 95 MPa at room temperature. A maximum 2.8% plastic strain was generated near the weld defect.

Sample WC-95 PL #2 has no defects and does not show any change in mechanical properties after the room temperature preload of 95 MPa, as no local plasticity is generated in the sample. Similarly, Sample WC-53 PL, which also has defects, does not show any significant change in properties after a room temperature preload of 53 MPa, as the preload is not sufficient to generate local plasticity.

FEA simulations are performed to determine the critical preload value at which specimens reach the yield point. The results show that overloading the notched water wall specimens with a preload of 65 MPa, which is equivalent to 110% of the MAWP, generates 0.1% of plastic strain, while the welded membrane specimens generate 0.4% of plastic strain near the weld defect. This indicates that overloading the defect-containing water walls can give rise to local plastic zones near the cracks. Keeping the preload close to MAWP results in the generation of minor local plastic zones, which do not significantly alter the tensile properties of the water walls.

4.5 Summary

The test matrix involves subjecting samples to different room-temperature hydrostatic pressure preloads, followed by high-temperature tensile tests to evaluate mechanical properties. The following conclusions can be drawn from the testing:

Notched specimens exhibit strain hardening and strain aging effects when preloaded at 95 MPa, exceeding the material's yielding point. However, a preload of 53 MPa, below the yielding point, does not result in these effects. In weld membrane specimens, preloading to stresses around 53 MPa (equivalent to 100% of MAWP) does not cause significant strain hardening and strain aging, as the stress near defects remains below the yield strength. Significant effects of strain hardening and strain aging are observed in weld membrane specimens preloaded at 95 MPa (150% of MAWP) due to plastic deformation generated by loading lack of fusion defects beyond yielding. To avoid the effects of strain hardening and strain aging at stress concentration points in defect-containing boiler membranes, it is suggested to keep the hydrostatic pressure

at around 110% of MAWP.

Chapter 5

3D characterization of internal defects for fatigue performance of welded SA192 steel water walls

5.1 Introduction

This chapter focuses on the investigation of weld defects generated during water wall repairs observed in Chapter 3 and their impact on high-temperature LCF tests. Repaired water walls, subjected to rigorous in-phase thermo-mechanical loading conditions during start-ups and shutdowns, often face the challenge of LCF failures. These failures frequently initiate from stress-concentration areas, necessitating a comprehensive understanding of the weld defects to unravel the reasons behind shortened fatigue life in certain water walls.

The primary objective of this chapter is to provide a thorough assessment of the weld defects and their influence on fatigue crack initiation sites and the overall fatigue performance of water walls. A key aspect of this investigation involves the utilization of nano-XCT analysis to delve into the intricate details of the weld defects. A comprehensive characterization is achieved by considering variables such as defect size, shape, and position of internal defects within the water walls. By shedding light on the specific characteristics and locations of these defects, factors contributing to fatigue crack initiation have been identified.

5.2 Experimental and Analysis Methodology

The water walls investigated in this study had an operational history, having been in service for approximately 18 years. During their service life, these water walls were exposed to challenging operating conditions. On the waterside, temperatures reached around 300°C, while on the fireside, temperatures could reach as high as 850°C [111]. Furthermore, the steam pressure inside the tubes reached approximately 9.5 MPa.

One crucial factor that contributed to the fatigue loading experienced by the water walls was the frequent occurrence of shutdowns and start-ups. These water walls underwent approximately 10 shutdown and start-up cycles per year, as shown in Figure 5.1. Each cycle involved temporarily terminating the operation followed by subsequent reactivation, resulting in significant cyclic loading on the water walls. These low-cycle fatigue loading conditions could lead to the initiation and propagation of fatigue cracks, ultimately affecting the structural integrity and performance of the water walls.

Fatigue test specimens were carefully extracted from specific regions within the weld membranes of water walls. These specimens were extracted in accordance with the guidelines provided by ASTM E606, ensuring standardized procedures for reliable testing and analysis. Both defect-containing and defect-free sections of the water walls were targeted to provide a comprehensive assessment of the influence of internal defects on fatigue behaviour.

To begin the characterization process, the cross-sectional ends of the extracted specimens were initially examined using optical microscopy. This step aimed to identify any visible internal defects that could impact the fatigue performance of the water walls.

To further investigate and precisely quantify the presence and extent of internal defects, the specimens underwent XCT scanning. The XCT scans were performed using the Zeiss Xradia Versa 620 X-Ray Microscope, which offered high-resolution

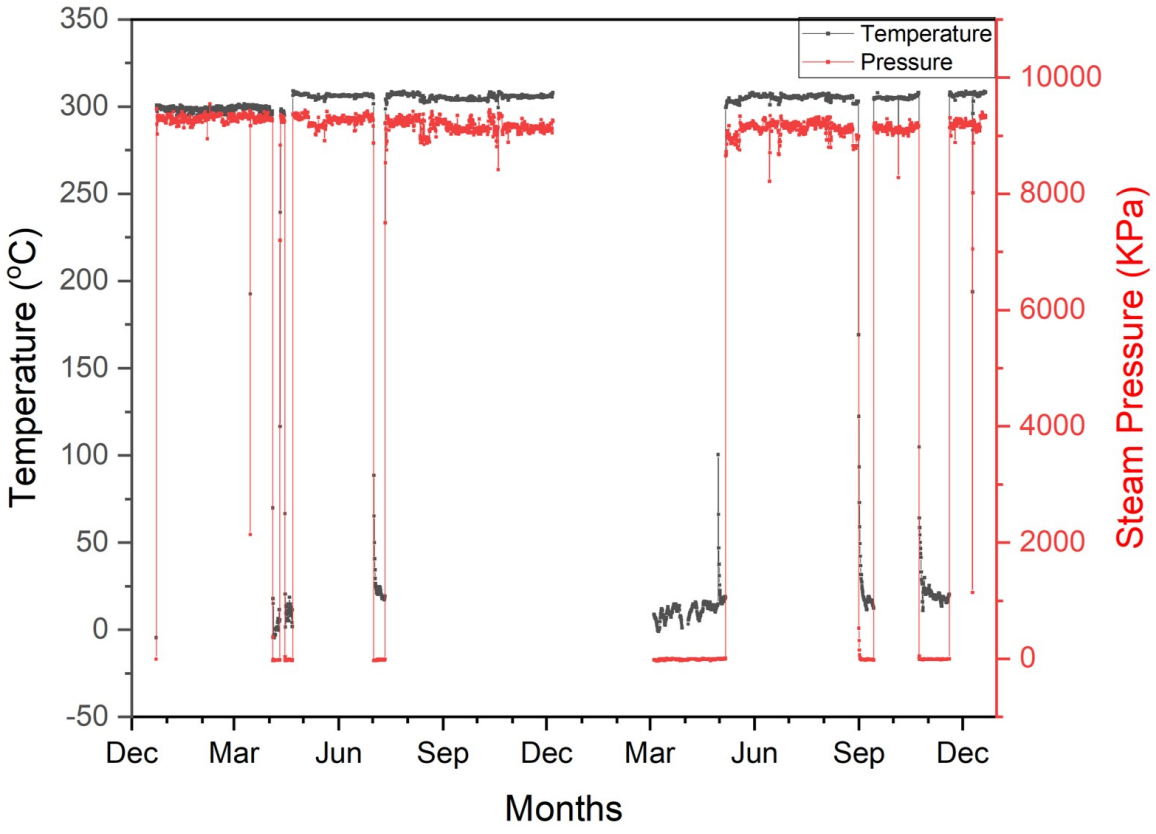

Figure 5.1: Operating temperature and steam pressure of water walls over a span of 2 years

imaging capabilities. The spatial resolution of the XCT scans was set at 500 nm, enabling detailed visualization of the internal structures and defects within the specimens. The acquired XCT data was processed to generate 3D images of the specimens, allowing for a comprehensive analysis of the internal defect characteristics.

In order to estimate the baseline tensile properties of the water wall components, three defect-free tensile specimens were extracted from both the base tube and the membrane. These specimens were then subjected to tensile testing at the operating temperature of the water wall (300°C). The collected stress-strain data from these tests were used to determine the mechanical properties of the weld.

To calculate the properties of the weld, the rule of mixtures was employed. This approach required stress-strain data from both the base metal and the welded membrane. The engineering stress-strain data obtained from the tests were converted to true stress-strain values, and the Ludwik-Hollomon hardening law was fitted to the data from the base metal. By assuming a uniform longitudinal strain across the welded membrane, Young's modulus and yield strength of the weld were calculated.

It is worth noting that the accuracy of the stress-strain curve for the weld was highly dependent on the estimation of the area of the base metal and the welded membrane. To accomplish this, direct measurements of the metallographic sections were utilized.

Additionally, the coefficient of thermal expansion (K^{-1}) of both the weld and the tube was determined as a function of temperature using Thermo-Calc, specifically utilizing the thermodynamic database TCFE10. This allowed for the calculation of the input parameters required for the finite element model.

The obtained baseline tensile properties, along with the thermal expansion coefficients, served as essential input data for the subsequent finite element analysis, enabling a comprehensive understanding of the mechanical behaviour of the water wall components under different operating conditions.

To accurately simulate the in-phase thermo-mechanical loading experienced by

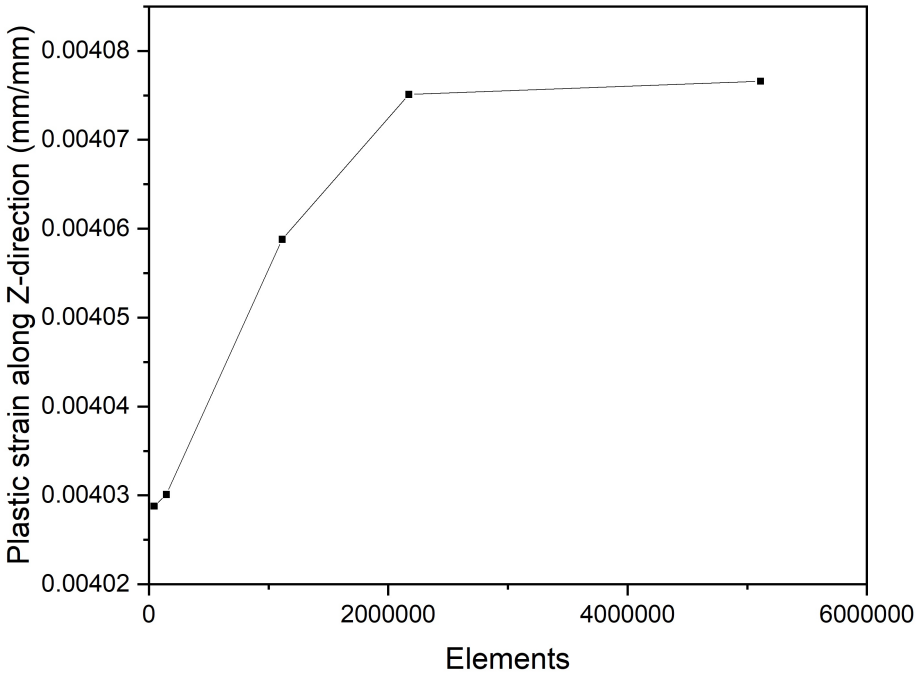

Figure 5.2: Mesh study for plastic strain in Z-direction

the water walls during start-ups and shutdowns, a FEA model was developed. The objective was to replicate the real service environment of the water walls and assess their structural behaviour.

The FEA model was created using ANSYS® Workbench software. It allowed for the simulation of the thermo-mechanical conditions and the analysis of the water walls' response. The focus of the analysis was on the axial direction, where the equivalent stress and plastic strain were of particular interest.

The boundary conditions in the FEA model were set to match the actual service environment of the water walls. The fireside boundary was assigned a temperature of 850°C, while the waterside boundary was set to 300°C. Additionally, a steam pressure of 9.5 MPa was applied to represent the internal pressure within the water walls.

To achieve accurate results, TET 10 elements were chosen for the FEA model. The element size was determined through a thorough mesh-dependent study to ensure appropriate resolution and convergence (Figure 5.2). Ultimately, a global element size of 1 mm was selected.

The ANSYS thermal-mechanical simulation employs a multi-linear plasticity hardening model to accurately capture the material behaviour of the water walls under thermo-mechanical loading conditions. The simulation is based on the balance of the linear momentum equation of the 3D model.

$$\frac{\partial \sigma_{\mathrm{ij}}}{\partial x_{\mathrm{j}}} + \rho b_{\mathrm{i}} = \rho a_{\mathrm{i}}, \tag{5.1}$$

where b_{i} and a_{i} are the body force and acceleration in the i-direction, respectively, which are assumed to be 0 during static analysis. σ_{ij} is the Cauchy stress tensor, and ρ is the density. The material was considered isotropic for the application of the elastic-plastic constitutive law. The multi-linear plasticity hardening model incorporated the concept of plastic deformation and accounted for the nonlinear material response under varying stresses. It considered the accumulation of plastic strain and its influence on the material's mechanical properties. The model was a rate-independent plasticity model that encompassed the von-Mises yield criteria and isotropic hardening. The von-Mises yield criteria were used to determine the onset of yielding in the material. It was based on the concept of equivalent stress, which took into account the combined effect of normal and shear stresses. When the equivalent stress exceeded the yield strength of the material, plastic deformation occurred. Isotropic hardening referred to the material's ability to undergo plastic deformation even after previous loading and unloading cycles. In this model, the yield surface remained centered along the centerline and expanded as plastic strain developed. This expansion reflected the material's capacity to sustain additional plastic deformation as it experienced more loading cycles.

$$\bar{\sigma} = K(\bar{\epsilon} + \epsilon_{\mathrm{o}})^{\mathrm{n}} \tag{5.2}$$

where $\bar{\sigma}$ and $\bar{\epsilon}$ are the equivalent stress and equivalent plastic strain, respectively, and K, n and ϵ_{o} are material constants.

Tensile and fatigue tests were carried out using an MTS Landmark servo-hydraulic test system, which was coupled with a MTS-653 furnace to provide the necessary temperature control. The fatigue test specimens were prepared by grinding the circumferential surface with #1200 grit sandpaper to ensure smoothness.

For the fatigue tests, a strain-controlled sinusoidal loading waveform was employed, with testing conducted at a temperature of 300°C. The strain levels applied during the tests were determined based on the findings from the finite element analysis (FEA) simulation. Two different strain ranges were selected, namely 0% to 0.4% and 0% to 0.7%. The tests were performed at a frequency of 0.1 Hz.

To determine the termination criteria for the fatigue tests, the peak and valley stresses were monitored. The tests were terminated when the peak and valley stresses dropped by more than 20% compared to the stable cycle value. This criterion helped identify the point at which the material exhibited significant fatigue damage, indicating a decrease in its load-carrying capacity.

Following the completion of fatigue testing, the fracture surfaces of the specimens were carefully examined using a Vega3 Tescan scanning electron microscope (SEM). The SEM analysis allowed for a detailed investigation of the nucleation sites and crack growth regions present on the fracture surfaces. During the analysis, an accelerating voltage of 20 kV was utilized, while maintaining a working distance of 10 mm.

To further analyze the fracture surfaces and obtain quantitative data, the image analysis software ImageJ was employed. This software facilitated the measurement of the critical defect size, specifically the square root of the defect area ($\sqrt{area}$) [112]. This measurement took into account the projection of the defect area onto a plane perpendicular to the applied loading direction.

The specimens underwent a preparation process involving grinding with progressively finer grit SiC sandpapers (#80 to #1200) and polishing with diamond suspensions (3 μm, 1 μm, and 0.25 μm). A 4% Nital etchant was then used to reveal the microstructure. Microhardness was measured using a Tukon 2500 Vickers microhard-

ness tester with a 0.05 kgf load and 10-second dwell time.

5.3 Results

Three defect-free tensile specimens have been tested at the operating temperature of the water wall (300°C) to determine their baseline tensile properties. The obtained data are summarized in the provided Table 5.1. Instrumental errors sometimes lead to the reporting of a slightly lower value of Young's Modulus. Hence for further analysis, a conventional value of 195 GPa which is in range with the obtained value has been used. The properties of the weld are derived from both the tube and the membrane using the rule of mixtures, which necessitates stress-strain tensile data from the base metal and welded membrane. To accurately assess the properties of the weld, the engineering stress-strain data are converted to true stress-strain values. The Ludwik-Hollomon hardening law is then fitted to the base metal data. Assuming uniform longitudinal strain across the welded membrane, Young's modulus and yield strength of the weld are calculated. The calculated values are illustrated in Figure 5.3.

The stress-strain behaviour of the weld exhibits a strong dependence on the accurate estimation of the base metal and welded membrane areas. To accomplish this, direct measurements of the metallographic sections are conducted. Additionally, Thermo-Calc, utilizing the thermodynamic database TCFE10, is employed to calculate the coefficient of thermal expansion (K^{-1}) for the weld and tube as a function of temperature shown in Figure 5.4. These values are crucial inputs for the finite element model.

Figure 5.5 depicts the equivalent stress and total strain experienced in the axial direction during the in-phase thermo-mechanical loading of the water walls. The strain levels obtained from the finite element analysis (FEA) model represent the cumulative impact of both thermal gradient and steam pressure within the actual service environment of the water walls.

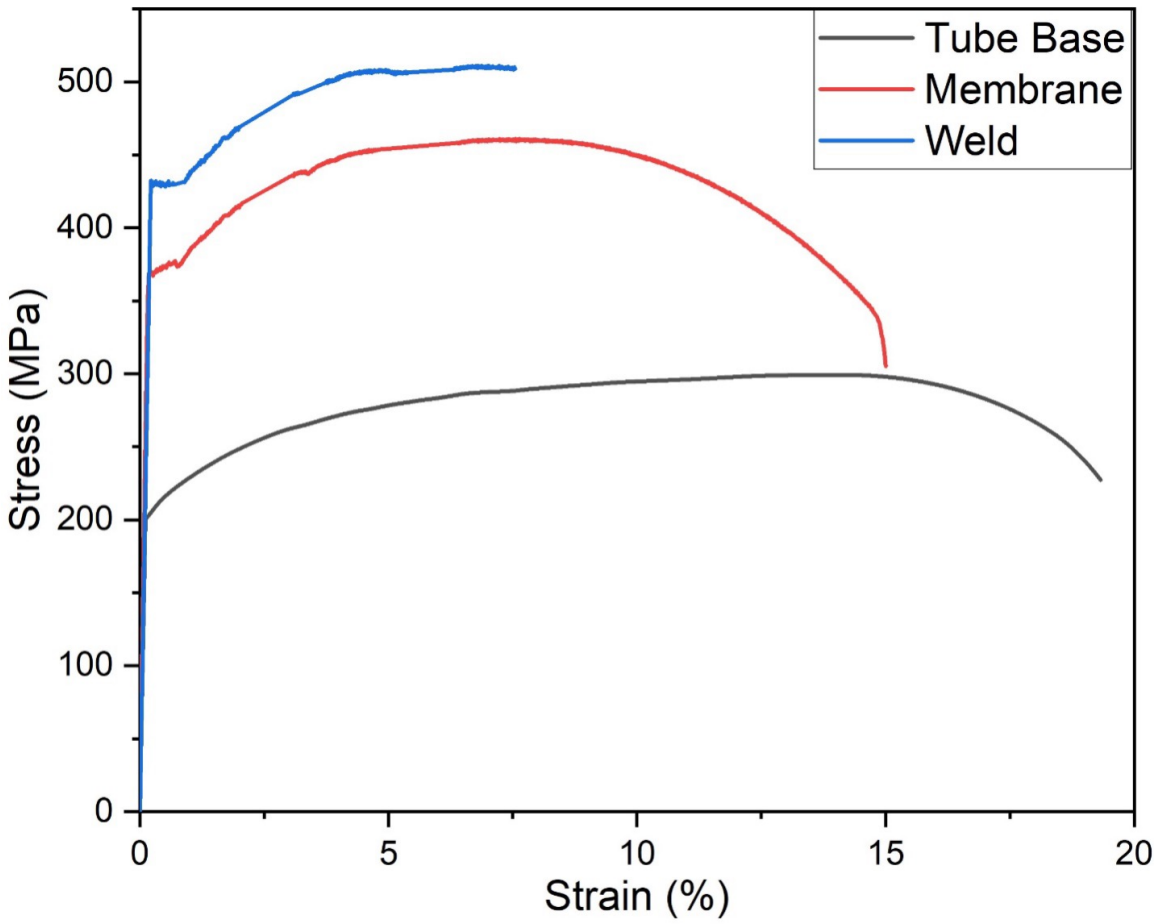

Figure 5.3: Stress-strain curves for Tube Base, Membrane, and Weld. The weld and tube base properties served as input parameters for finite element simulation

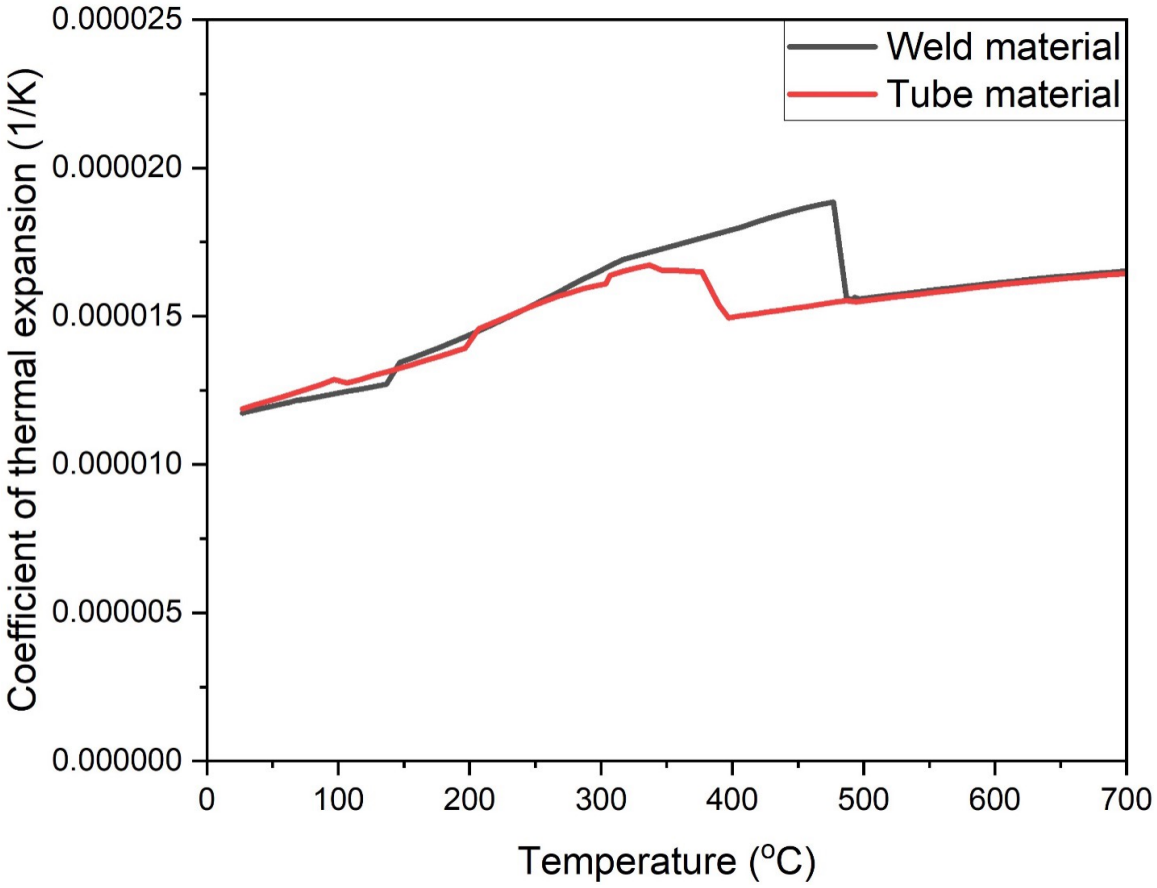

Figure 5.4: Coefficient of thermal expansion as a function of temperature for weld and base metals

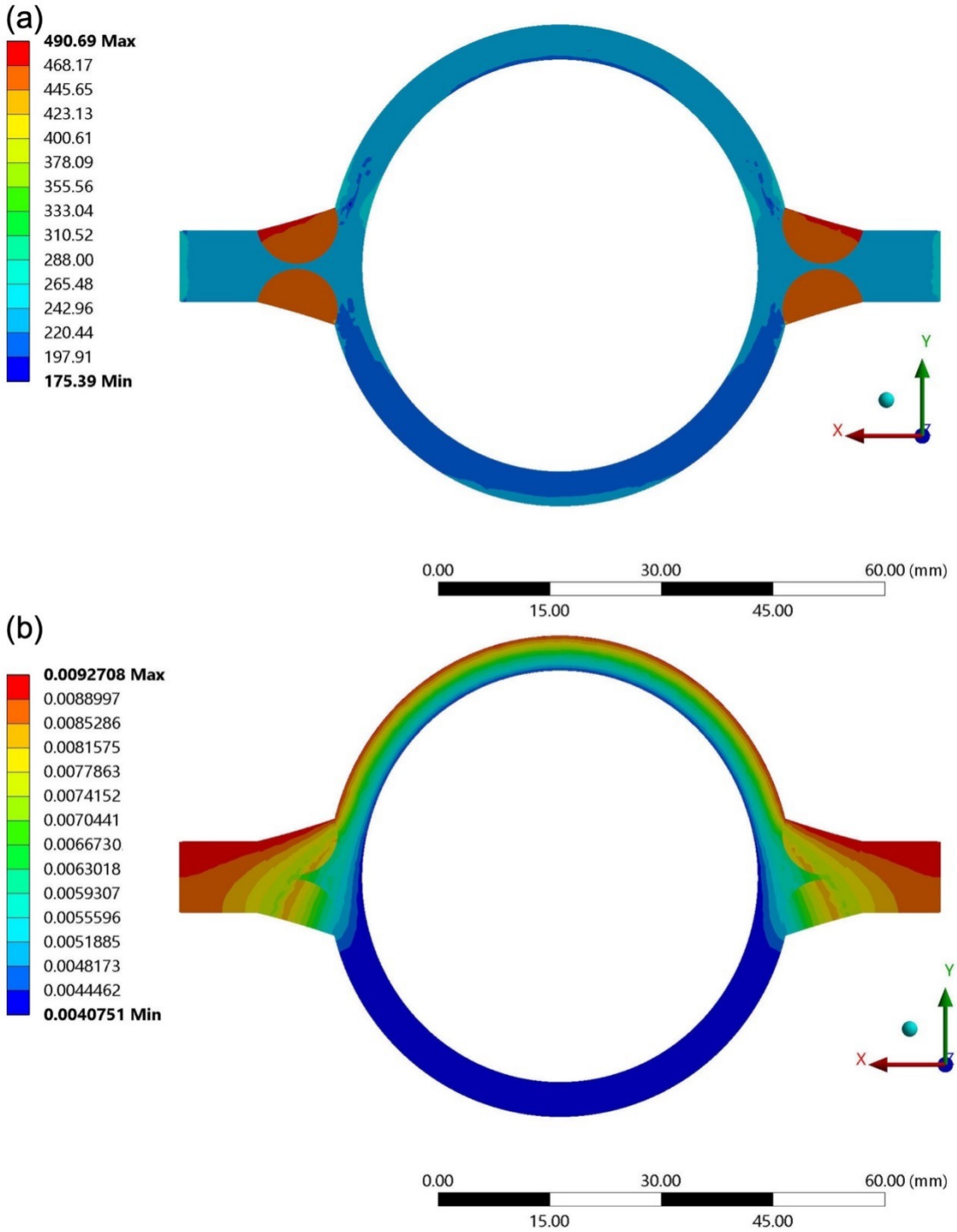

Figure 5.5: ANSYS simulation of water walls: (a) equivalent stress, and (b) total strain in Z-direction (i.e., tube axial direction)

Table 5.1: Mechanical properties of water walls tested at 300°C.

Material	**Yield Strength (MPa)**	**Tensile Strength (MPa)**	**Young's Modulus (GPa)**
Tube Base	200	298	180 (Measured)
Membrane	367	461	215
Weld	435	511	228

Figure 5.6 illustrates the cross-sectional views of two types of specimens: defect-containing and defect-free, captured from both the left and right ends. Upon visual inspection, no visible defects are observed in Specimen C, Specimen D, Specimen G, and Specimen H, indicating that they are defect-free. On the other hand, defect-containing specimens, namely Specimen A, Specimen B, Specimen E, and Specimen F, exhibit a lack of fusion along the entire length of the specimens. However, it should be noted that optical macrographs can only confirm the presence of defects at the ends of the specimens.

To validate the presence of defects throughout the entire length of the specimens, XCT scanning is employed for three-dimensional imaging. XCT scanning provides a detailed and comprehensive analysis of the internal structure and defects within the specimens, allowing for a more accurate assessment of their presence and distribution.

The XCT scans of defective specimens A, B, E, and F are presented in Figure 5.7. These scans provide a comprehensive visualization of the internal structure and defect characteristics of the specimens. The scans confirm the presence of a continuous lack of fusion slit, which is aligned parallel to the axis of the fatigue specimen. Post-processing of the XCT scans enables the detailed identification and analysis of the defect features throughout the gauge length of the specimens. Specifically, Specimen A has seven porosity defects at the edges of the lack of fusion, Specimen B has four porosity defects, and Specimen E exhibits six porosity defects in proximity to the lack of fusion. In contrast, Specimen F displays a lack of fusion slit without any

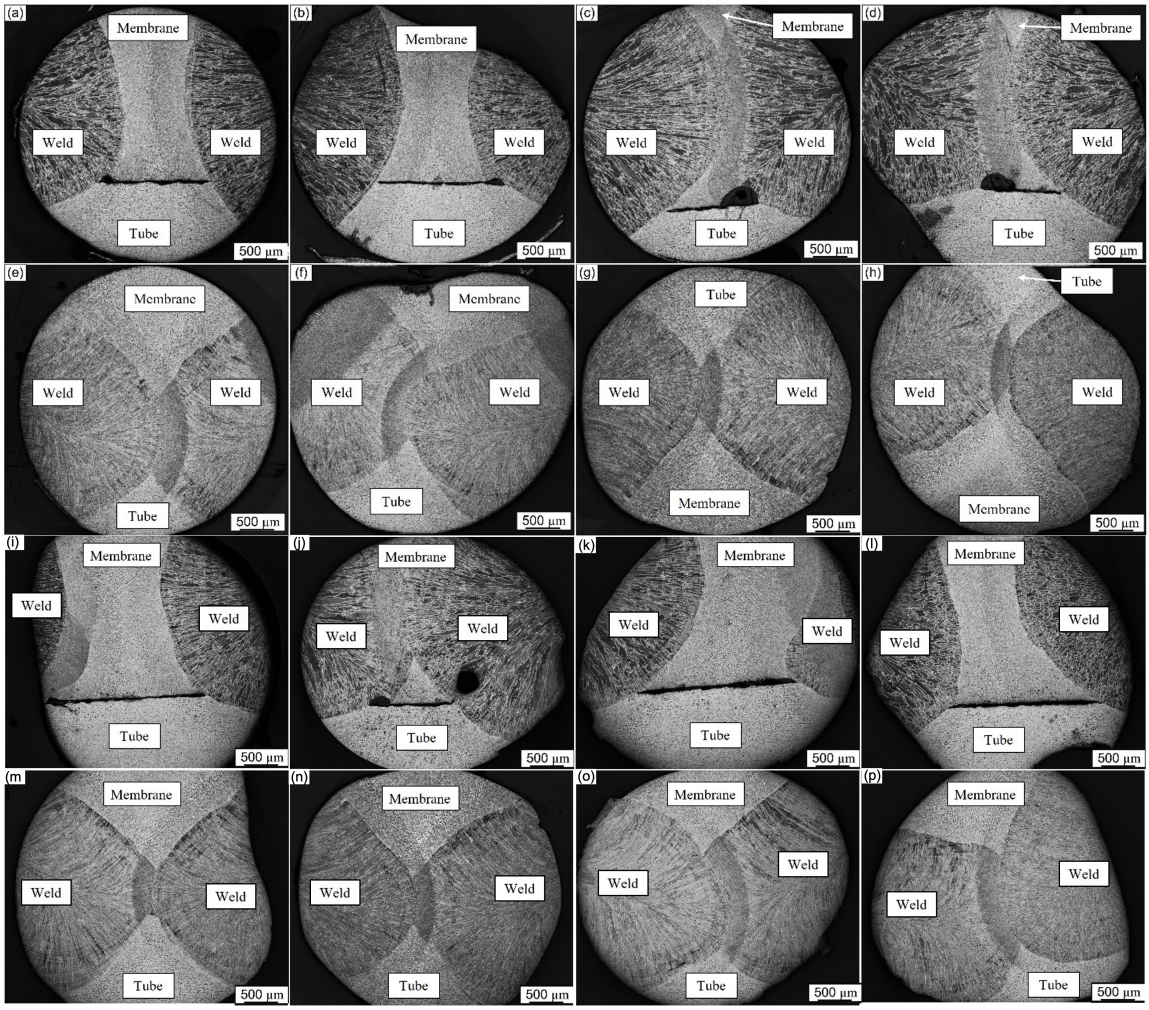

Figure 5.6: Cross-sectional macrographs of fatigue test specimens: (a) and (b): left and right ends of Specimen A; (c) and (d) left and right ends of Specimen B; (e) and (f) left and right ends of Specimen C; (g) and (h) left and right ends of Specimen D; (i) and (j): left and right ends of Specimen E; (k) and (l): left and right ends of Specimen F; (m) and (n): left and right ends of Specimen G; (o) and (p): left and right ends of Specimen H

accompanying defects.

The XCT scans of defect-free specimens, specifically Specimen C, Specimen D, Specimen G, and Specimen H, reveal the absence of any internal defects. Scans of Specimen G and Specimen H, as depicted in Figure 5.8, demonstrate a homogeneous and continuous material structure throughout the gauge length of the specimens. By thoroughly examining the post-processed XCT scans, it is confirmed that Specimen G and Specimen H do not exhibit any discernible internal defects such as lack of fusion, porosity, or other irregularities.

The fatigue test matrix presented in Table 5.2 provides quantitative information on the fatigue properties and performance of the eight specimens under investigation. Specimens A to D are subjected to a peak strain of 0.4%, while Specimens E to H are subjected to a peak strain of 0.7%.

Specimen A exhibits a fatigue life of 6262 cycles before failure, with the crack initiating at defect A_{D2}. Specimen B, on the other hand, sustains 15312 cycles before failure, with the crack initiating at defect B_{D1}. For the specimens tested at 0.7% peak strain, Specimen E endures 1663 cycles before failure, with the crack initiating at defect E_{D6}. Specimen F sustains 1279 cycles before failure, and the crack initiation is observed throughout the entirety of the lack of fusion slit.

In the case of defect-free specimens tested at 0.4% peak strain, Specimen C fails after 21171 cycles, while Specimen D fails after 27288 cycles. For defect-free specimens tested at 0.7% peak strain, Specimen G fails after 2974 cycles, and Specimen H fails after 2890 cycles.

The presence of defects significantly reduces the fatigue life of the water wall specimens, with the defects being the preferred locations for fatigue fracture initiation. It is noteworthy that Specimen A, despite having a smaller amount of weld metal compared to Specimen B, exhibits a shorter fatigue life. This can be attributed to the dominant influence of defect size and position in determining the fatigue life of the specimen.

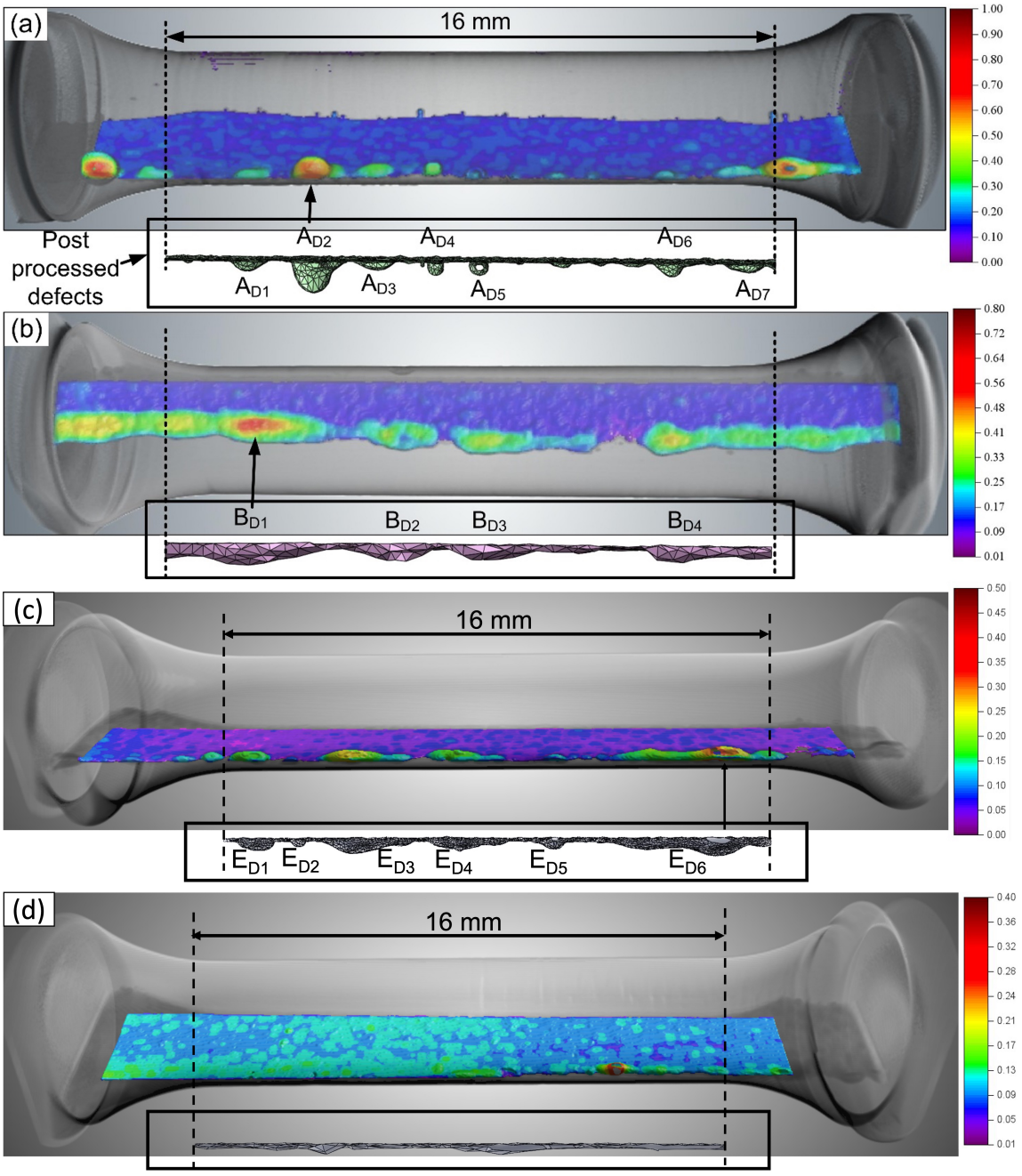

Figure 5.7: X-ray computed tomography scans for (a) Specimen A, (b) Specimen E, (c) Specimen B, and (d) Specimen F

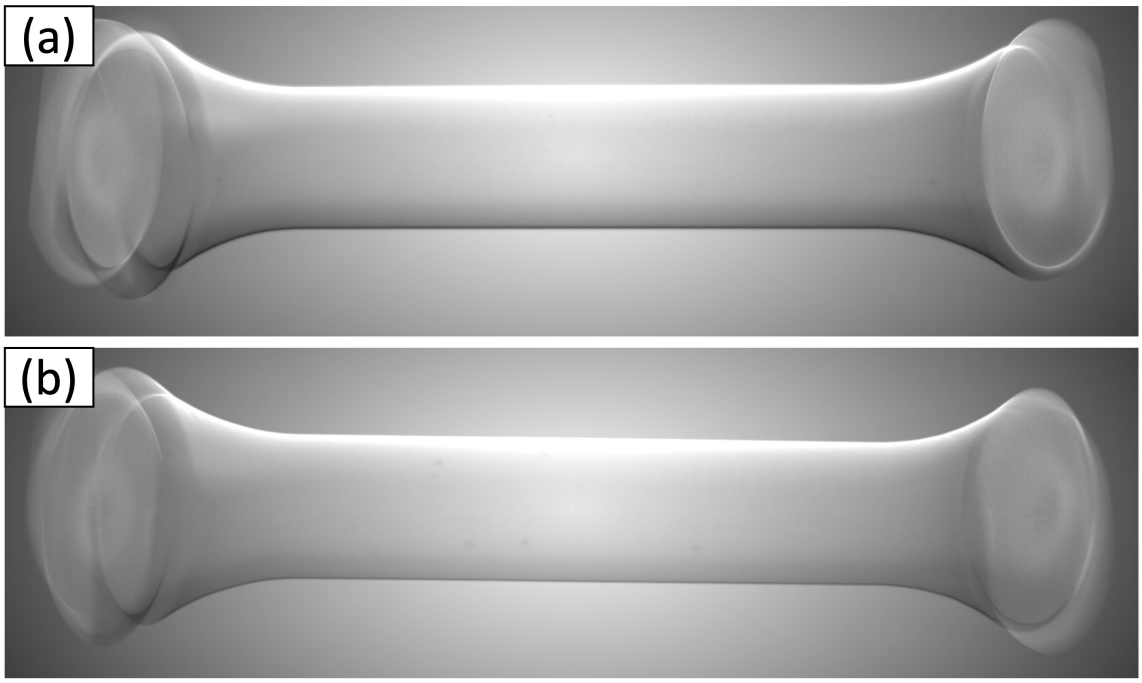

Figure 5.8: X-ray computed tomography scans for (a) Specimen G, and (b) Specimen H

Furthermore, Specimen E displays a longer fatigue life compared to Specimen F. This can be attributed to Specimen F having a larger lack of fusion slit without any porosities, leading to fatigue crack initiation occurring at two different locations.

In defect-free specimens, the weld fusion zone is identified as the most susceptible location for fatigue crack initiation. Comparing the fatigue lives of the specimens, a maximum reduction of 77% in fatigue life is observed due to the presence of defects.

Figure 5.9 represents the fatigue life results for all the specimens tested at a peak strain of 0.4%. The cycles to failure for each specimen are represented on the horizontal axis, while the maximum and minimum stresses experienced by each specimen per cycle are plotted on the vertical axis.

Similarly, Figure 5.10 illustrates the fatigue life results for all the specimens tested at a peak strain of 0.7%. The cycles to failure for each specimen are plotted on the horizontal axis, while the maximum and minimum stresses experienced by each specimen per cycle are shown on the vertical axis.

Table 5.2: Fatigue test matrix and results

Specimen	**Specimen Type**	**Test condition**	**Cycles to failure ($2N_f$)**	**Fracture Location**
A	With defect	0-0.4% ϵ 300°C 0.1 Hz	6262	A_{D2}
B	With defect		15,312	B_{D1}
C	Defect-free		21,171	Weld
D	Defect-free		27,288	Weld
E	With defect	0-0.7% ϵ 300°C 0.1 Hz	1663	E_{D6}
F	With defect		1279	Lack of fusion slit
G	Defect-free		2974	Weld
H	Defect-free		2890	Weld

It is important to note that a peak strain level of 0.4% or 0.7% causes plastic deformation in the specimens, resulting in work hardening. When the specimens are unloaded and return to the zero-stress condition, residual plastic strain is generated. This residual plastic strain enables the specimens to experience compressive stress at 0% strain.

The fractured surfaces of the specimens are carefully examined to provide a comprehensive understanding of the fracture mechanism. Figures 5.11 (a-b) present the fractographs for Specimen A, while Figures 5.11 (c-d) show the fractographs for Specimen B. Similarly, Figures 5.13 (a-b) display the fractographs for Specimen E, and Figures 5.13 (c-d) represent the fractographs for Specimen F.

In all four specimens, it is observed that the crack initiation occurs at an internal defect, which then propagates through the specimen. The crack continues to grow until it reaches a critical size that significantly reduces the stress-bearing capacity of the specimen. The final failure of the specimens is caused by tensile pull resulting from ongoing fatigue crack initiation and growth.

Upon closer examination at higher magnifications, striations are observed in the crack growth region. These striations provide clear evidence of fatigue as the primary mode of crack propagation. The presence of these striations confirms that the fatigue mechanism plays a significant role in the specimens' failure.

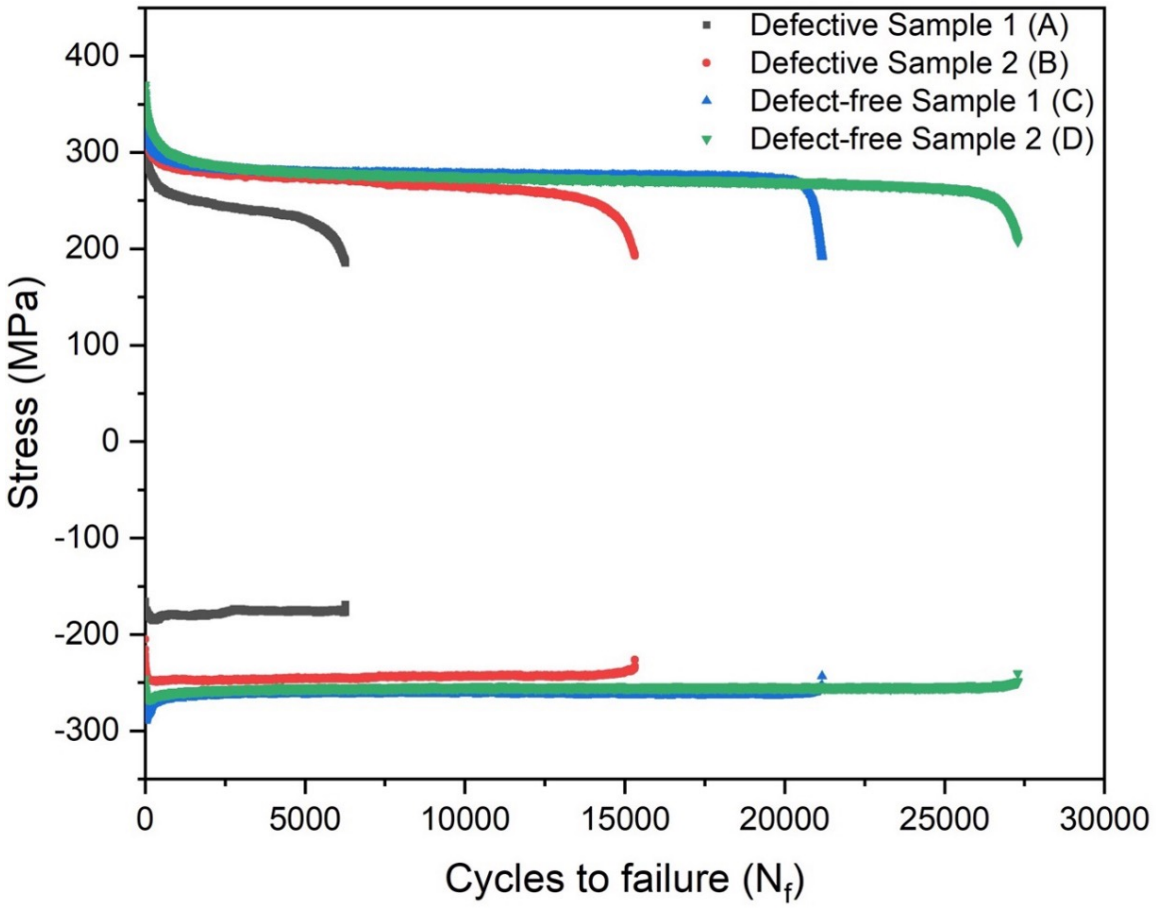

Figure 5.9: Maximum and minimum stresses vs number of cycles to failure curves for fatigue tested specimens at 0.4% peak strain

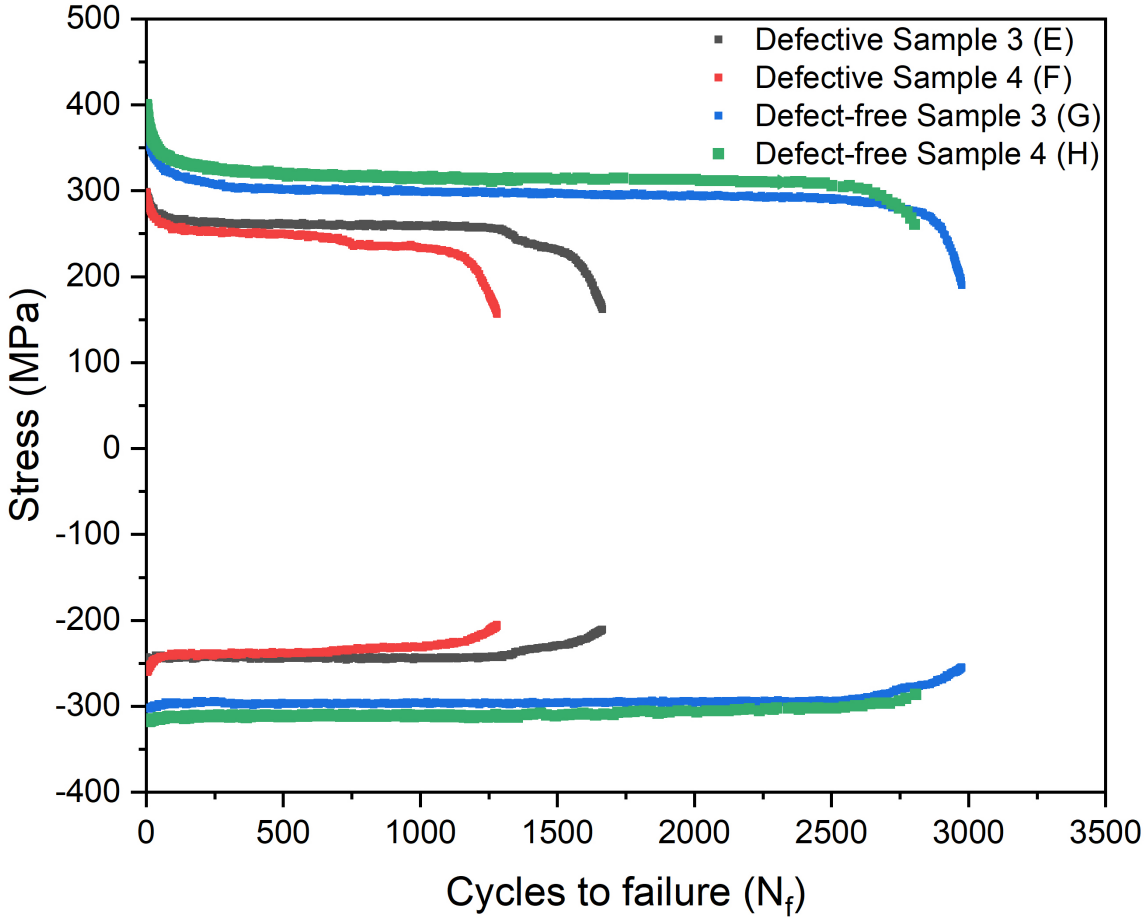

Figure 5.10: Maximum and minimum stresses vs number of cycles to failure curves for fatigue tested specimens at 0.7% peak strain

In the case of Specimen B, the defect size is smaller compared to Specimen A, which results in Specimen B enduring more fatigue cycles before failure occurs.

For Specimen E, the crack initiation occurs from a defect, while in Specimen F, there are two crack initiation sites. One of the cracks in Specimen F originates from the entirety of the lack of fusion slit, indicating a significant role of the defect in the fatigue failure process.

On the other hand, the defect-free specimens, namely Specimen C, Specimen D, Specimen G, and Specimen H (Figures 5.12 (a-b), Figures 5.12 (c-d), and Figures 5.14 (a-b), Figures 5.14 (c-d), show no visible defects on their fractured surfaces. However, clear striations are observed, providing conclusive evidence of fatigue propagation even in the absence of visible defects.

Figure 5.15 shows the cross-sectional macrographs and hardness map for defect-free Specimens C and D. In Figure 5.15(a), the crack initiation site for Specimen C is depicted, showing that the crack originated from the weld region. This observation confirms that the weld region is susceptible to crack initiation in defect-free specimens. The hardness map presented in Figure 5.15(b) further supports this finding. It reveals that the weld region exhibits higher hardness compared to the base metal. The hardness measurement for the weld region is 211 HV, while the base metal (soft ferritic matrix) has a hardness of 100 HV. This disparity in hardness values indicates a significant difference in the mechanical properties of the weld region and the surrounding base metal. A similar trend of cracking is observed in defect-free Specimen D, as shown in Figure 5.15(c). The crack initiation site is also located in the weld region, reaffirming the role of microstructure in determining the fatigue crack initiation site for defect-free specimens. A similar trend was observed for Specimen G and H.

5.4 Discussion

The present study combines FEA analysis and experimental characterization to investigate the effect of defects on fatigue life. FEA analysis is employed as an initial

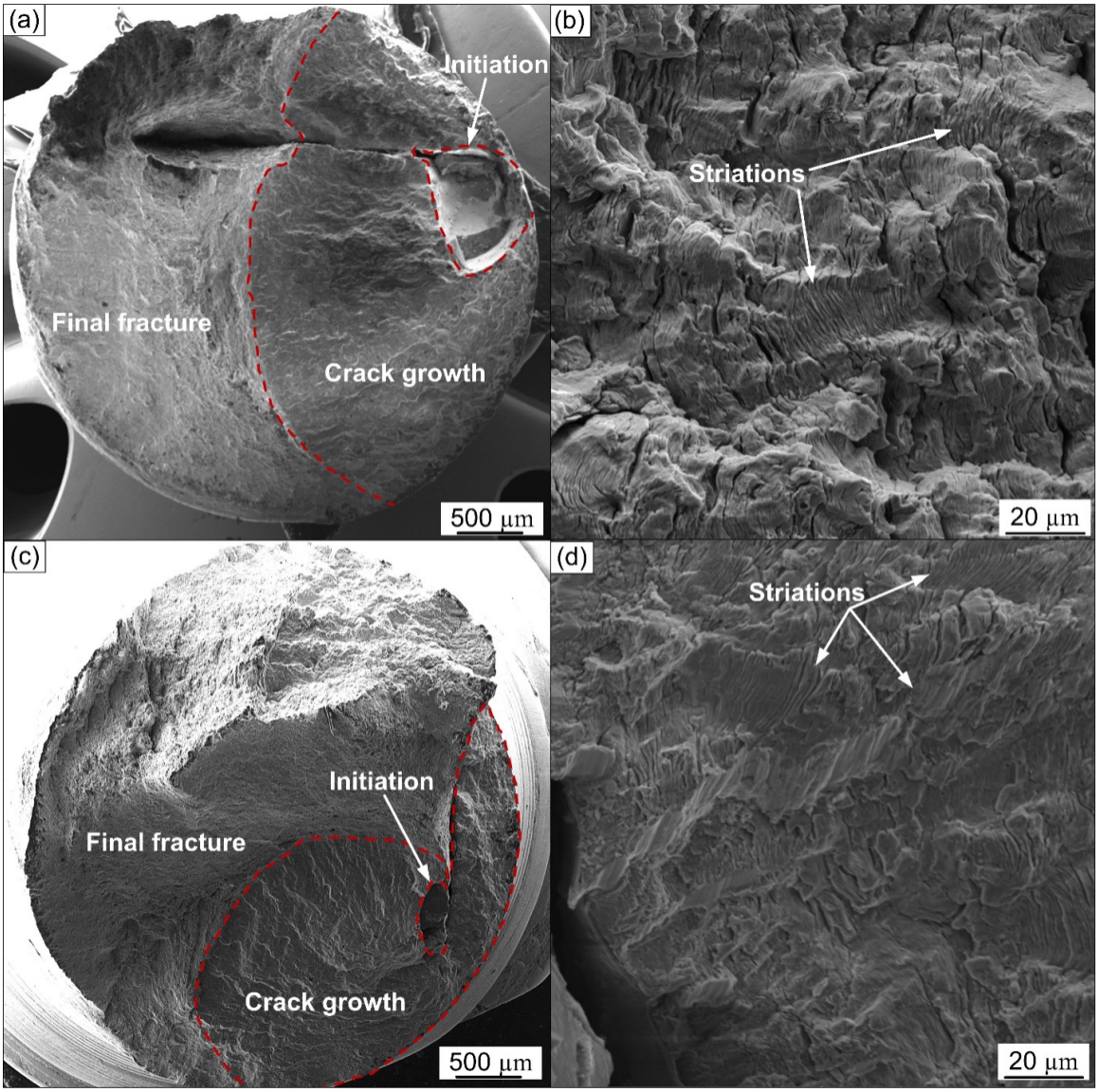

Figure 5.11: Fractography of specimens with defects: (a) the entire fracture surface Specimen A (b) fatigue striations in Specimen A, (c) the entire fracture surface Specimen B, and (d) fatigue striations in Specimen B

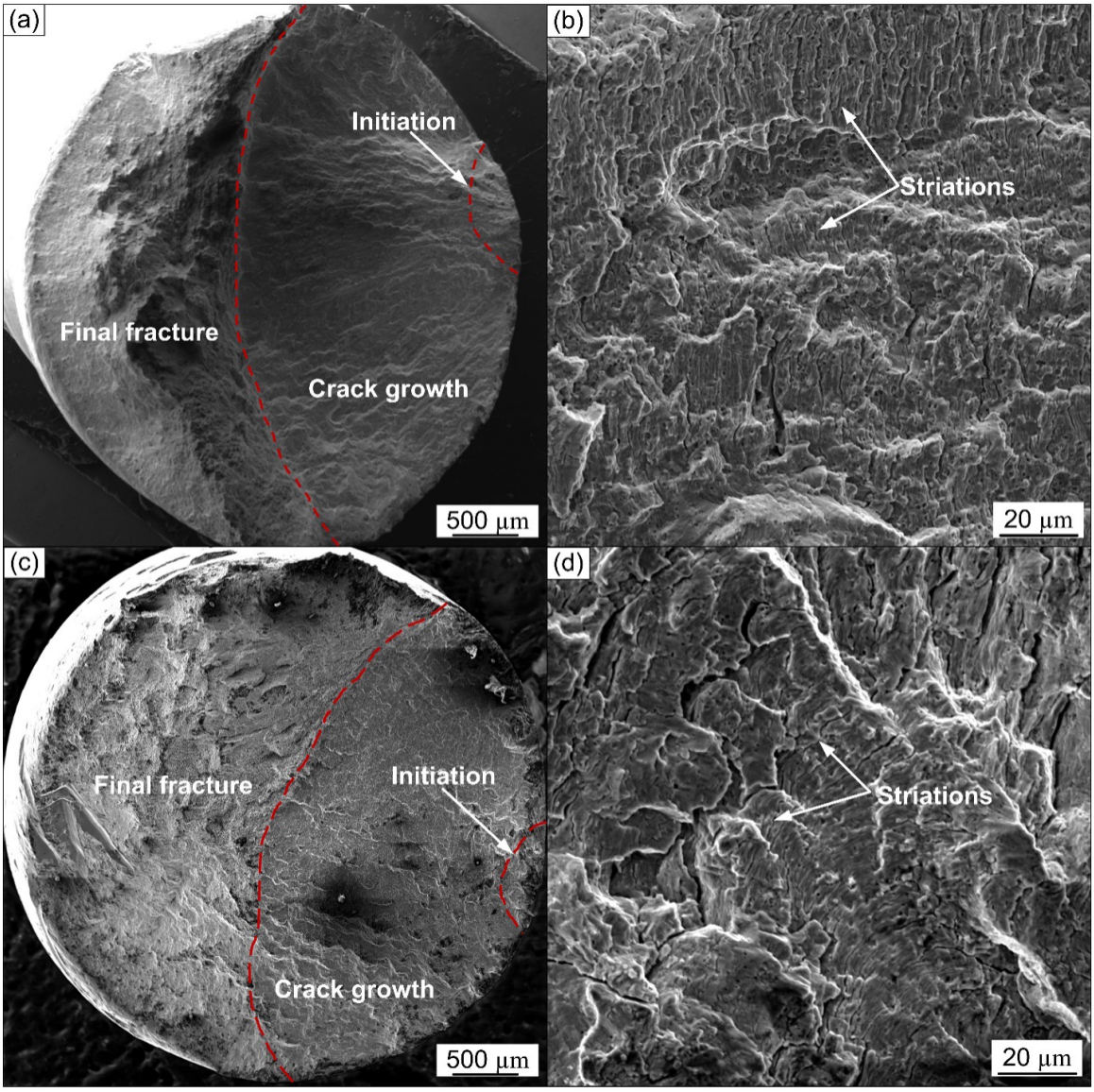

Figure 5.12: Fractography of defect-free specimens: (a) the entire fracture surface Specimen C (b) fatigue striations in Specimen C, (c) the entire fracture surface Specimen D, and (d) fatigue striations in Specimen D

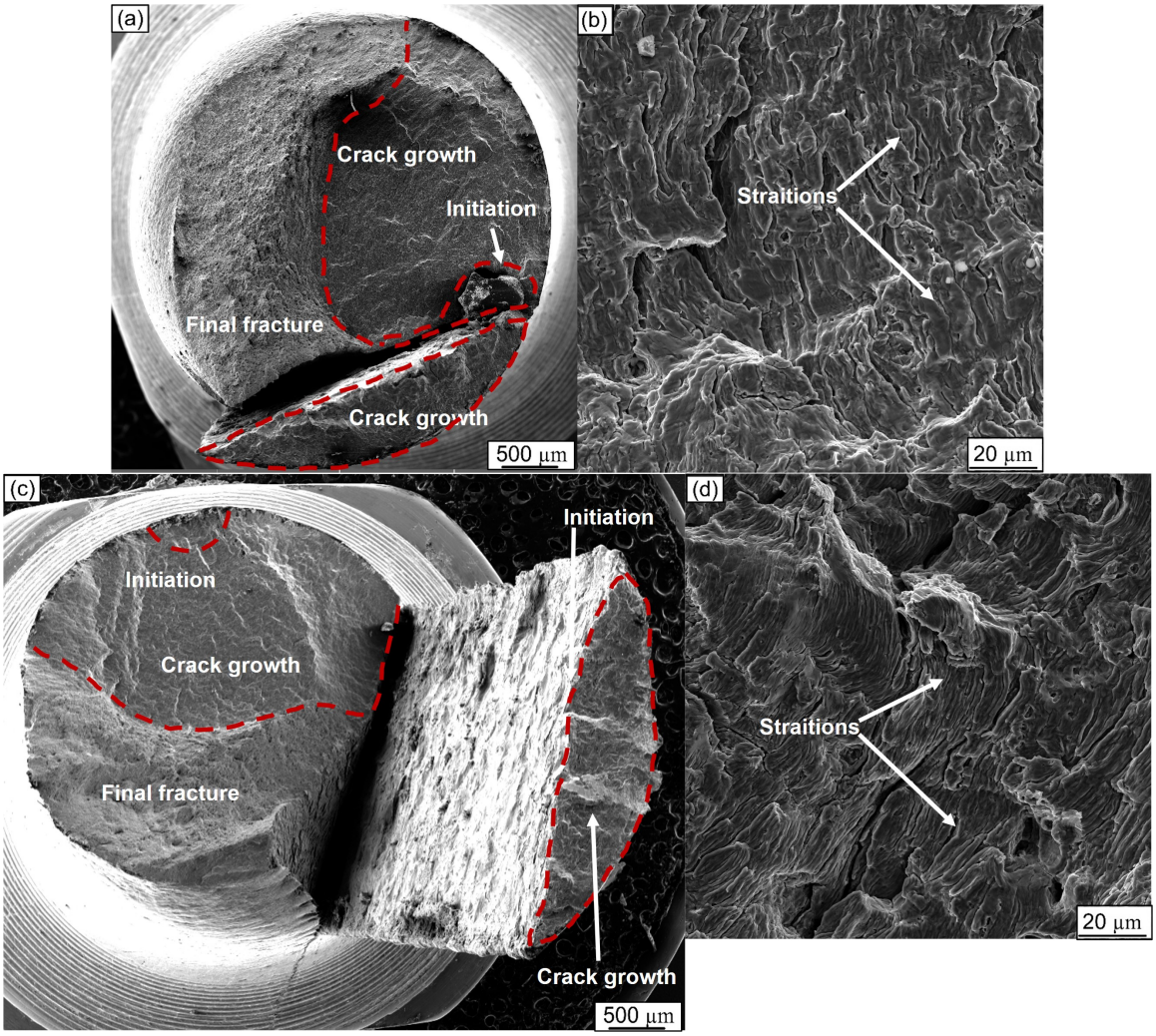

Figure 5.13: Fractography of specimens with defects: (a) the entire fracture surface Specimen E (b) fatigue striations in Specimen E, (c) the entire fracture surface Specimen F, and (d) fatigue striations in Specimen F

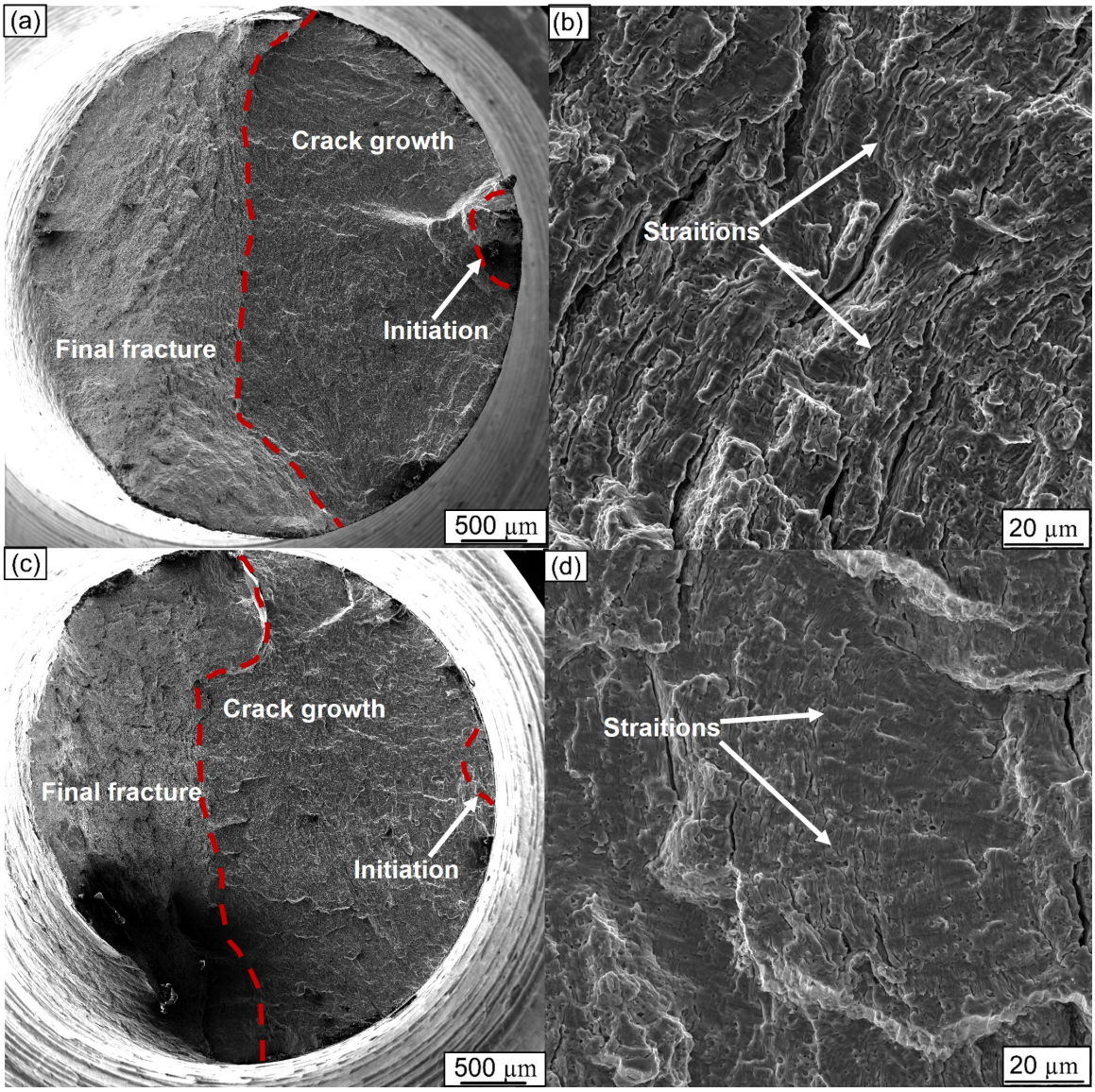

Figure 5.14: Fractography of defect-free specimens: (a) the entire fracture surface Specimen G (b) fatigue striations in Specimen G, (c) the entire fracture surface Specimen H, and (d) fatigue striations in Specimen H

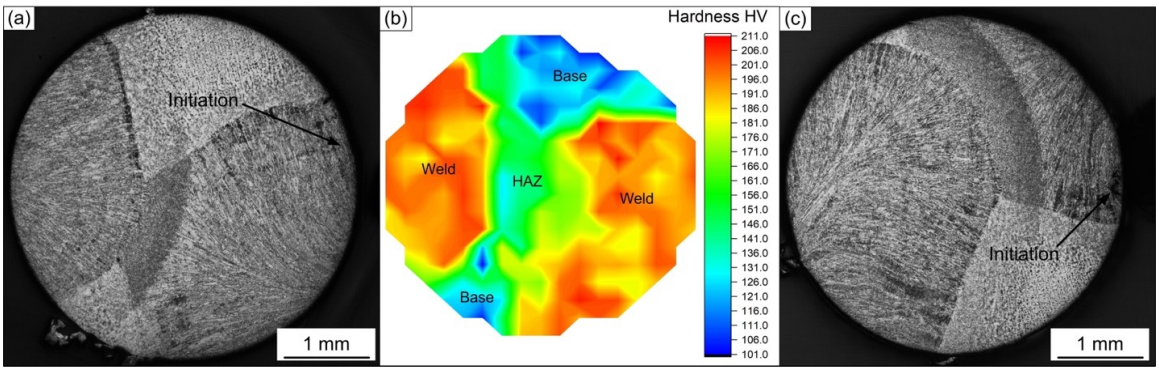

Figure 5.15: (a) macrograph of Specimen C shows fatigue crack initiation, (b) hardness map of Specimen C, and (c) macrograph of Specimen D

tool to determine the experimental parameters, considering the in-service conditions of the water wall material under the actual in-phase thermo-mechanical environment of 300-850°C and 9.5 MPa steam pressure. This analysis aids in identifying the strain parameter for the subsequent low-cycle fatigue tests (refer to Figure 5.5).

The crack propagation is observed to occur perpendicular to the direction of the maximum principal stress, indicating fracture behaviour in Mode I for all specimens [112]. The initial volume of defects plays a significant role in influencing the fatigue life of the specimens, as the stress triaxiality at the crack initiation site is highly dependent on the defect volume [113][114]. In the water walls, defects are consistently present throughout the section, making them potential sites for fatigue crack initiation.

While 2D analysis of defects provides a preliminary understanding of their presence, it lacks detailed information about their characteristics. On the other hand, 3D XCT analysis enables the detection of defects in three-dimensional space and facilitates the quantification of their volume, distribution, location, and morphology. During the post-processing of the 3D XCT scans, the gauge length is systematically sliced at 0.1 mm intervals, allowing measurement of the projected defect at each cross-section for defect size and stress intensity factor (SIF) calculations. These measurements are then used to quantify the defect parameters, including size, shape, position, and SIF. The summarized results of this subsequent analysis are presented in Table 5.3. It is

important to note that the severe irregularity in the shape of defect AD5 hinders the quantification of its specific shape and SIF parameters.

The defect size in this study is represented by the square root of the defect's projected area, as depicted in the provided Figure 5.16 [113][114]. Defect distribution for Specimen F cannot be obtained as it only has a lack of fusion slit. To estimate the maximum prospective defect size for each specimen, the EVS method is employed. This method allows for the calculation of the maximum size of defects by analyzing statistical distributions. The defect size obtained from the macrographs of fractured surfaces is then compared with the maximum prospective defect size calculated using the EVS method.

In the analysis of the maximum prospective defect size, the GPD function is utilized. The GPD function is described by equation 5.3, which provides a statistical model for the distribution of extreme values in a dataset. By fitting the GPD function to the data, the maximum prospective defect size can be estimated and further compared to the observed defect size from the macrographs [115].

$$F(x) = 1 - (1 + \gamma \frac{x - u}{\sigma})^{\frac{-1}{\gamma}} \tag{5.3}$$

where σ, γ and u are the scale parameters, shape parameters, and threshold value, respectively.

The mean excess (ME) plot is utilized to analyze the defect size for each cross-section of the specimens, following the methodology described by Ghosh et al [116]. The ME plot provides valuable information regarding the statistical behaviour of the defect sizes. Figure 5.17 illustrates the ME plot for Specimen A, Specimen B, and Specimen E. The linear portion of the ME plot is of particular interest as it allows for the calculation of the scale and shape parameters for the GPD function.

To determine the threshold value (u), which represents the point at which the mean excess of the data becomes linear [82], a suitable choice is made by observing the ME plot. In this study, the threshold value is selected at 350 μm for Specimen A, 320 μm

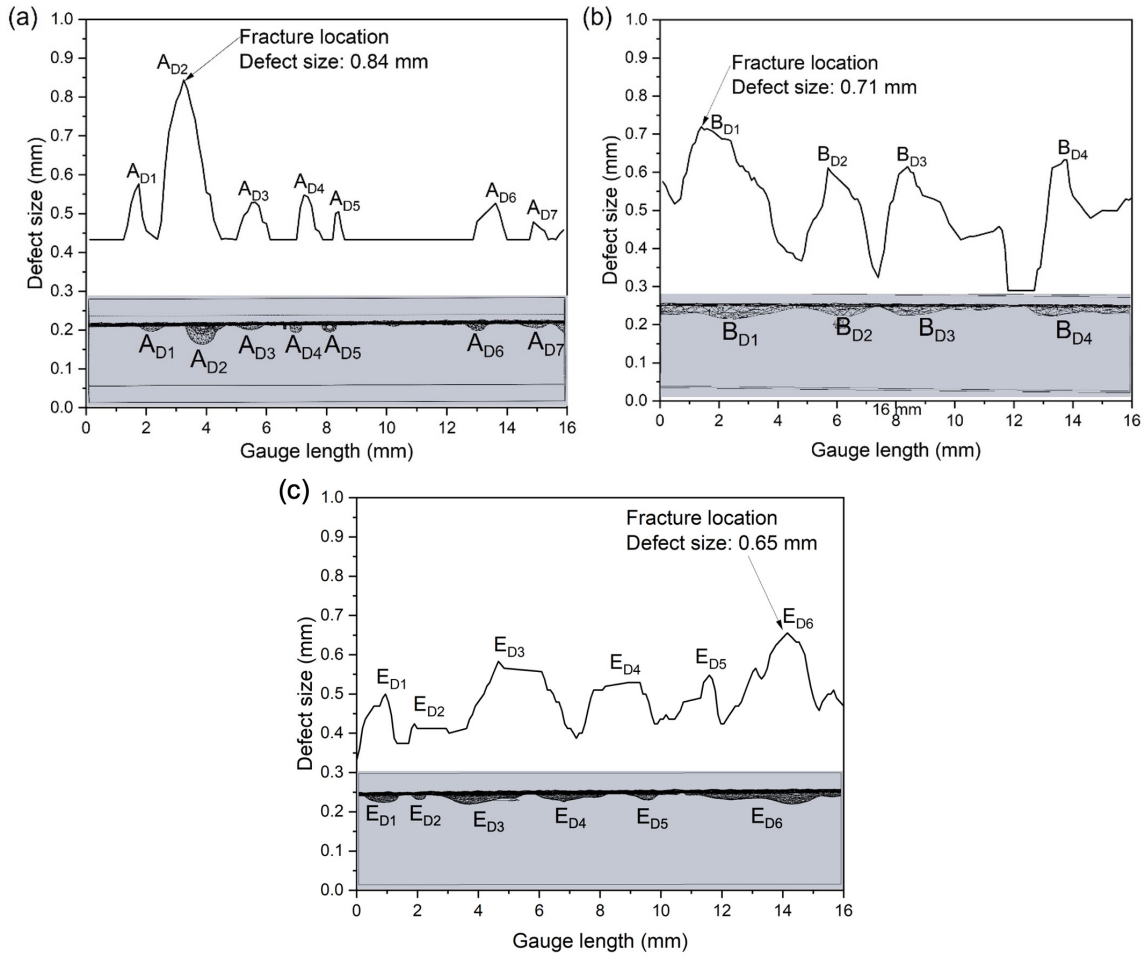

Figure 5.16: Distribution of defect size throughout the gauge length; (a) for Specimen A, (b) for Specimen B, and (c) for Specimen E

for Specimen B, and 410 μm for Specimen E, as the ME plot demonstrates a nearly linear trend above these values.

Table 5.3: Various defect parameters calculated from XCT scans

Specimen ID	Defect ID	Defect Size (mm)	Defect size from fracture surface (mm)	Maximum predicted defect size from EVS (mm)	Sphericity	Circularity	Aspect Ratio	Shortest distance from edge (mm)	SIF from Murakami formula ($MPa\sqrt{m}$)	SIF from LEFM ($MPa\sqrt{m}$)	SIF % Difference between Murakami and LEFM
Specimen A	AD1	0.58	0.81	1.03	0.73	0.47	0.29	0.03	10.44	9.89	5.27
	AD2	0.84			0.76	0.65	0.51	0.01	13.20	13.59	2.87
	AD3	0.53			0.70	0.46	0.28	0.13	10.00	9.05	9.50
	AD4	0.55			0.88	0.80	0.37	0.17	10.18	9.60	5.70
	AD5	0.52			-	-	-	0.03	-	-	-
	AD6	0.53			0.70	0.69	0.29	0.04	9.98	9.71	2.71
	AD7	0.48			0.61	0.45	0.30	0.08	9.51	9.42	0.95
Specimen B	BD1	0.72	0.70	0.90	0.51	0.23	0.21	0.42	12.70	13.50	2.44
	BD2	0.61			0.50	0.35	0.14	0.37	11.71	11.71	0
	BD3	0.62			0.45	0.20	0.09	0.28	11.86	12.19	2.71
	BD4	0.63			0.50	0.26	0.16	0.21	12.03	13.01	7.53
Specimen E	ED1	0.5	0.68	0.83	0.69	0.19	0.26	0.35	9.98	10.1	1.18
	ED2	0.42			0.87	0.59	0.15	0.18	9.33	9.87	5.47
	ED3	0.58			0.57	0.25	0.11	0.23	10.34	10.29	0.48
	ED4	0.52			0.54	0.24	0.15	0.31	10.02	10.88	8.58
	ED5	0.54			0.81	0.72	0.25	0.16	10	9.87	1.31
	ED6	0.65			0.51	0.49	0.11	0.1	12.34	12.58	1.90

The shape parameter (γ) can be calculated from the slope of the linear portion of the ME plot, while the scale parameter (σ) can be calculated from the intercept. These parameters play a crucial role in characterizing the statistical distribution of defect sizes.

Mathematically, the maximum prospective defect size is represented by equation 5.4, which takes into account the scale and shape parameters obtained from the ME plot analysis.

$$\text{Maximum prospective defect size} = u - \frac{\sigma}{\gamma} \tag{5.4}$$

The predicted maximum defect sizes obtained from the EVS method align closely with the observed defect sizes from the macrographs of fractured surfaces. Figure 5.18 displays the defect dimensions and locations within the gauge length for Specimen A, Specimen B, and Specimen E.

In Specimen A, it is found that defects AD2 and AD7 have the largest and smallest sizes, respectively, among all the defects present. Notably, defect AD2, which is also the site of fatigue initiation, exhibits a significantly larger size of 0.84 mm compared to the other defects in the specimen. The sizes of the remaining defects in Specimen A range around 0.5 mm.

A similar analysis conducted for Specimen B and Specimen E reveals that the largest defect at the fracture site is BD1 (0.72 mm) for Specimen B and ED6 (0.44 mm) for Specimen E. The sizes of the other defects in these specimens are approximately 0.6 mm and 0.3 mm, respectively.

It is worth noting that the largest defect size is observed in Specimen A compared to Specimen B, which is consistent with the results obtained from the fatigue life experimental and statistical analysis. Additionally, when comparing Specimen E and Specimen F, it is evident that the fracture site for Specimen F corresponds to the entire lack of fusion slit, whereas for Specimen E, the crack initiation site was from only one defect. This difference in defect characteristics contributes to the longer

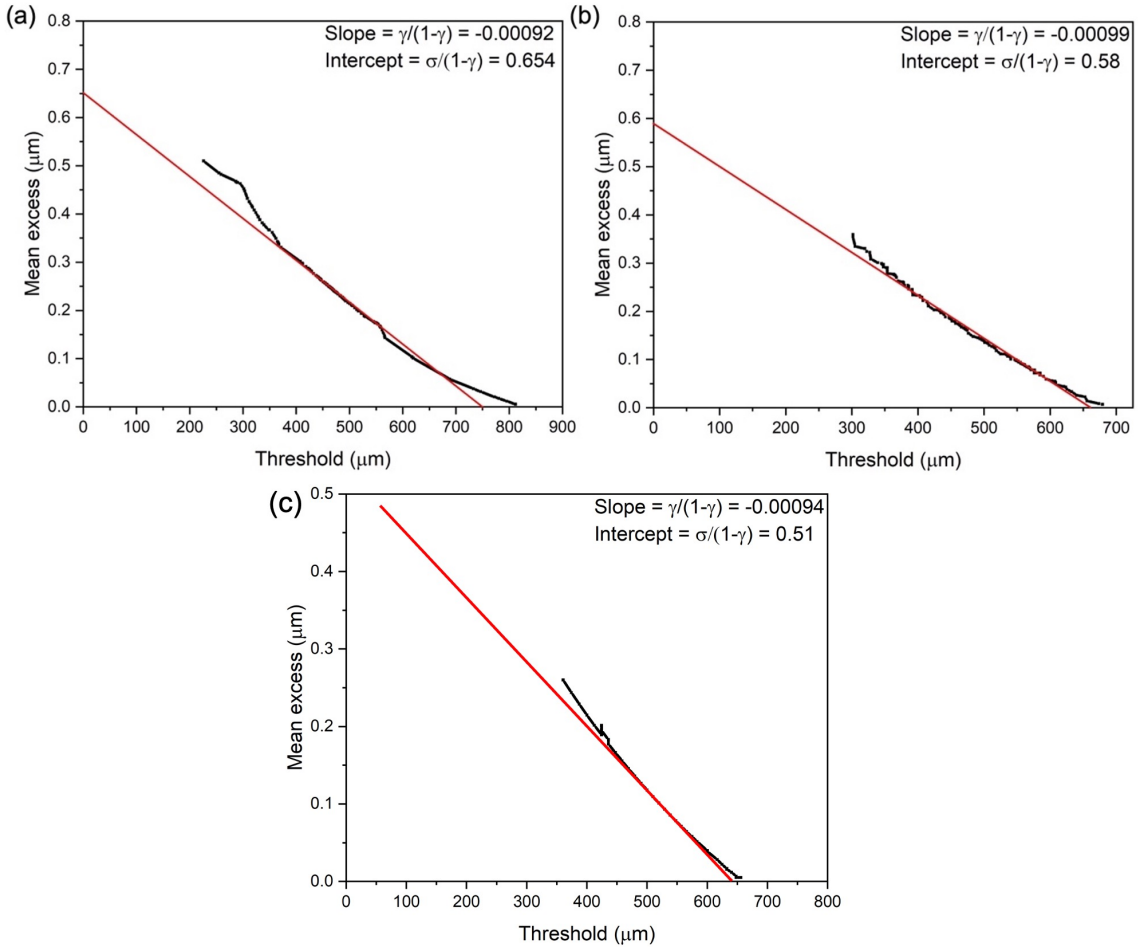

Figure 5.17: Mean excess (ME) plot for (a) Specimen A, (b) Specimen B, and (c) Specimen E

fatigue life observed in Specimen E compared to Specimen F.

The shape characteristics of a defect can be described using parameters such as sphericity, aspect ratio, and circularity, which provide information about the roundness and sharpness of the defect [112]. The aspect ratio is defined as the ratio between the minor axis and the major axis of the ellipse (2D) or ellipsoid (3D) fitted into the defect. Sphericity, on the other hand, measures how closely a defect resembles a sphere, with values ranging from 0 to 1, where 1 indicates a more spherical shape [91]. Circularity is another parameter used to assess the roundness of a defect.

In the case of Specimen A, the defect AD2, which is the crack initiation site, exhibits a maximum aspect ratio of 0.51, while the other defects have aspect ratios around 0.3 (Figure 5.19). Similarly, for Specimen B, the critical defect BD1 has a slightly higher aspect ratio (0.21) compared to the other defects. In Specimen E, the critical defect ED6 has a lower aspect ratio compared to the other defects, but the size and shape of the defect played a dominant role in determining the crack initiation site. Since ED6 is the largest and the sharpest defect, the crack initiation occurred from that specific defect.

The aspect ratio vs circularity plot (Figure 5.19 (b)) demonstrates that circularity alone cannot be considered a reliable indicator for predicting the fatigue crack initiation site. However, the dimensional heat map and corresponding shape parameters clearly indicate that defect AD2 in Specimen A is sharper than defect BD1 in Specimen B. The sharpness of defect AD2 makes it more susceptible to fatigue initiation, which is confirmed by the smaller number of cycles to failure compared to Specimen B. The same trend can be observed for Specimen E, where even though the aspect ratio of ED6 is lower, the heat map clearly shows that ED6 is the sharpest defect.

The position of a defect in relation to the free surface of the specimen is an important parameter in fatigue testing and can influence the crack initiation and propagation behaviour [89]. In the case of Specimen A, the critical defect AD2 is located very close to the free surface, at a distance of 0.01 mm. This sub-surface position of the

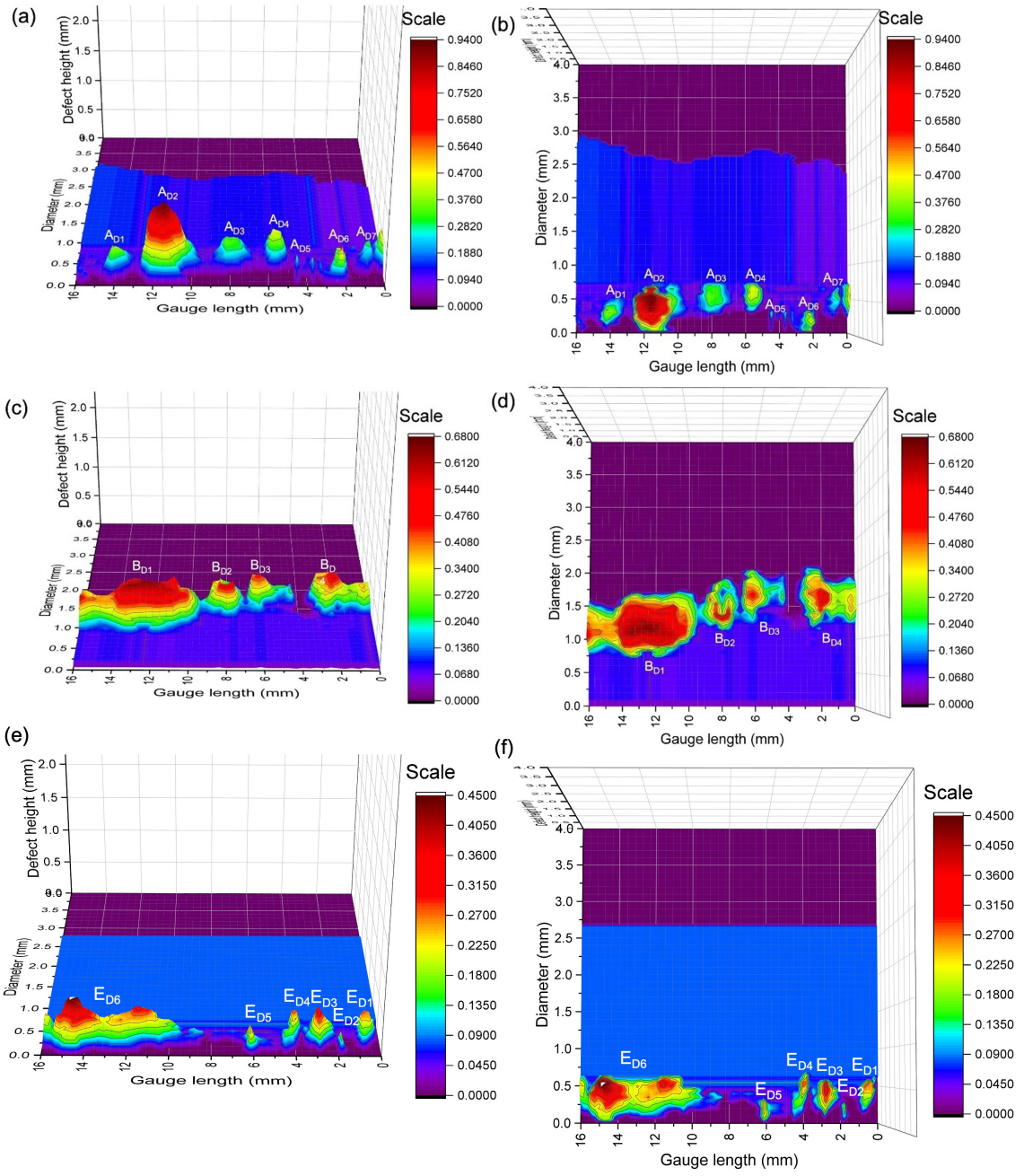

Figure 5.18: Dimensional heat map from XCT scans, showing height and width of defects: (a) and (b) are for Specimen A, (c) and (d) are for Specimen B, and (e) and (f) are for Specimen E

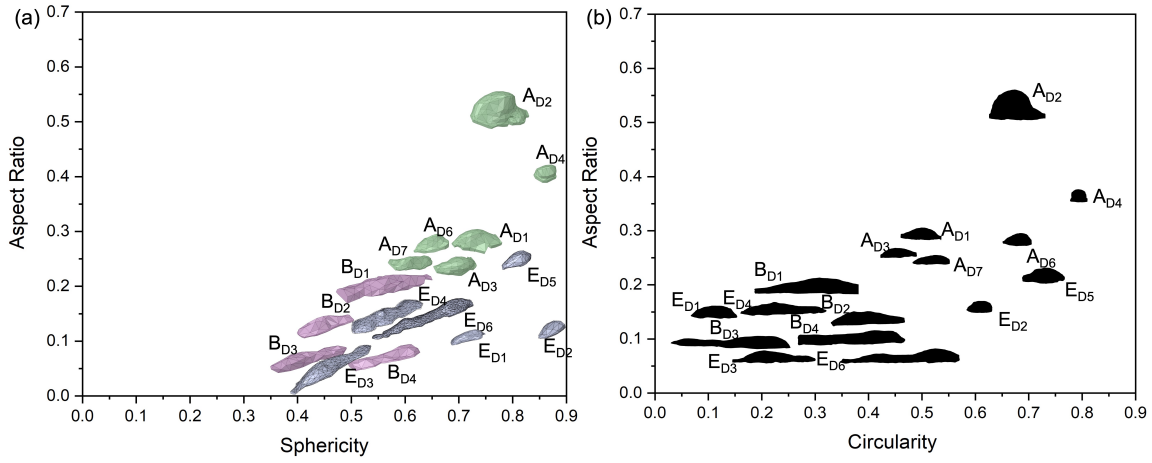

Figure 5.19: The shape parameters of defects: (a) aspect ratio vs. sphericity, and (b) aspect ratio vs. circularity.

defect accelerates the fatigue crack initiation and propagation, resulting in a lower number of cycles to failure compared to Specimen B. In contrast, for Specimen B, the fatigue crack initiates at a greater distance from the free surface, approximately 0.42 mm. The defects in Specimen B, being located further away from the surface, contribute to a longer fatigue life compared to Specimen A.

In the case of Specimen E, the critical defect ED6 is positioned at a distance of 0.10 mm from the free surface. On the other hand, in Specimen F, the lack of fusion slit extends to the surface, making it a surface defect. Surface defects are particularly susceptible to fatigue crack initiation. Therefore, Specimen F experiences a shorter fatigue life compared to Specimen E due to the presence of a surface defect.

The distance of a defect from the free surface influences the stress distribution and concentration around the defect, which, in turn, affects the fatigue behaviour of the specimen. Sub-surface defects are typically more critical as they can initiate cracks under lower stress levels, leading to shorter fatigue lives. On the other hand, surface defects are more prone to rapid crack initiation, resulting in reduced fatigue life.

Murakami suggested a formula where the SIF range can be calculated using the stress data ($\Delta\sigma$) with defect size represented by the square root of the defect area (A_d) and a geometry factor Y [112].

$$\Delta K_I = Y \Delta\sigma \sqrt{\pi \sqrt{A_d}} \tag{5.5}$$

where Y is equal to 0.65 for surface defects and 0.5 for internal defects. The SIFs for each defect are calculated using equation 5.5 with a geometry factor of 0.5, considering all defects as internal defects.

The geometry correction factor can be calculated as a function of the aspect ratio a/b and inclination angle of defect β for more accurate calculations of SIFs [117]. The geometry factors and SIFs for each defect are also calculated using the LEFM model [86][87]:

$$\phi = \int_0^{\pi/2} \sqrt{1 - (1 - \frac{a^2}{c^2}) sin^2\theta} d\theta \tag{5.6}$$

$$\Delta K_I = \frac{\Delta\sigma\sqrt{\pi a}}{\phi} sin^2\theta + \frac{a^2}{c^2} cos^2\theta^{1/4} \tag{5.7}$$

where ϕ represents the elliptical integral, $2c$ denotes the major axis of the ellipse, and $2a$ represents the minor axis of the ellipse. When $\theta = 90°$, K_I reaches its maximum value, and when $\theta = 0°$, K_I reaches its minimum value. In this study, the major axis (c) and minor axis (a) of each defect are measured to calculate the value of ΔK_I, and the maximum value of ΔK_I is considered for comparison with the Murakami method. The SIF calculation using the Murakami method assumes a constant value for the geometry factor, regardless of the defect's shape, whereas the LEFM model takes into account the defect's aspect ratio.

The SIF values obtained using the Murakami and LEFM methods are analyzed for Specimen A, Specimen B, and Specimen E. It is observed that the defects with the highest SIF values, namely AD2 in Specimen A, BD1 in Specimen B, and ED6 in Specimen E, are the most favourable sites for fatigue crack initiation. This indicates that higher SIF values contribute to the initiation of fatigue cracks.

Further investigation reveals that the critical defect AD2 in Specimen A is comparatively sharper than the other defects, resulting in a higher SIF. Similarly, when comparing critical defect AD2 in Specimen A with BD1 in Specimen B, AD2 exhibits a higher SIF due to its sharper characteristics. As a result, Specimen A, which has a higher SIF for its critical defect, experiences a smaller number of cycles to failure compared to Specimen B.

It is important to note that the Murakami method tends to underpredict the SIF values in cases involving sharper defects, such as those observed in Specimen A. This discrepancy can be attributed to the method's limitation of not considering the shape parameter and assuming a fixed area for each defect. By not accounting for the shape characteristics, the Murakami method may underestimate the stress concentration effects of sharper defects, leading to lower predicted SIF values.

The type, shape, and size of defects in weld specimens are crucial parameters that significantly influence fatigue life. In the case of water wall welds, these defects are primarily attributed to improper welding practices. Porosities, for instance, indicate gas entrapment during welding, typically occurring at the edges of lack of fusion sites.

Moreover, it is important to note that the current tests focused on examining the effect of defects on fatigue performance specifically in the tube axial direction, considering the dimensional and shape constraints of water walls. However, to comprehensively understand the impact of defects, it is necessary to validate their effects in both the hoop and axial directions of water walls. This would provide a more comprehensive understanding of how defects influence the fatigue behaviour of the entire structure.

5.5 Summary

The study focuses on investigating the impact of fluid and thermal loadings on water walls during start-ups and shutdowns, which induce fluctuating stresses. 3D characterization of weld defects in water walls has been conducted to establish their correla-

tion with fatigue life. The use of 3D examination methods overcomes the limitations of traditional 2D approaches by quantifying defect and failure parameters.

Parameters such as sphericity, circularity, and aspect ratio are identified as effective indicators for describing the sharpness of defects. It is observed that sharper defects significantly reduced the fatigue life compared to rounder defects.

The SIF calculated using both the LEFM and Murakami methods are found to be in close agreement with each other. However, Murakami's method underpredicts the SIF calculation due to the omission of the shape parameter and reliance on a fixed defect area.

In defect-free specimens, the weld fusion zone has been identified as the most susceptible location for fatigue crack initiation. This can be attributed to the coarse dendritic microstructure, which is less ductile compared to the base material. The coarse microstructure is more prone to the formation of micro-cracks, ultimately leading to the development of primary cracks.

By considering these findings, further improvements can be made in the design and manufacturing of water walls, with a focus on minimizing defect sharpness and optimizing the microstructure to enhance fatigue life and overall structural integrity.

Chapter 6

Low cycle fatigue damage and crack propagation simulation of welded membranes

6.1 Introduction

This chapter focuses on developing a predictive model to determine the fatigue life of defect-containing welded water wall specimens. The weld defects characterized in Chapter 4 are incorporated into the model, and an investigation involving a combination of experimental testing and numerical analysis is carried out.

To estimate fatigue initiation and crack propagation, a combination of the cyclic plasticity model in the FE method and CDM theory is employed [118]. This approach relies on physical quantities such as stress, strain, and energy definitions. Key parameters extracted include the stress-mechanical strain hysteresis loop for the first cycle and the stabilized state, the evolution of maximum and minimum stress cycles, and the accumulated inelastic strain energy density per cycle at different stress ratios [119]. Direct Cyclic Analysis (DCA) is conducted based on the accumulated inelastic hysteresis strain energy per cycle to calculate damage accumulation throughout the fatigue process. This analysis takes into account the variations in cyclic plasticity. By considering the combination of cyclic plasticity and damage evolution, the model enables the estimation of fatigue initiation and fatigue crack growth.

To estimate fatigue crack propagation in welded membranes, the XFEM is employed [120][121][122]. XFEM allows for the simulation of mixed-mode crack propagation processes [123]. By utilizing the XFEM module in ABAQUS [124], the displacement field and stress field of a static crack in three-dimensional structures can be solved based on the principles of LEFM. This approach, which forms the core of this research, enables the analysis of crack propagation in welded membranes. The critical energy release rate is utilized as the criteria for crack growth in this methodology. These methods incorporate the introduction of virtual nodes, eliminating the need for special elements such as cohesive elements and supporting crack propagation along arbitrary paths. Furthermore, FEM coupled with DCA [125] is utilized to calculate the low-cycle fatigue life under constant amplitude cyclic loading. By combining FEM with DCA, the research aims to accurately estimate the fatigue life of the welded membranes.

Through this approach, the fatigue crack propagation behaviour in welded membranes is simulated. By employing XFEM, the study aims to simulate crack growth and determine critical crack growth paths based on the criteria of energy release rate. XFEM allows for the propagation of cracks along arbitrary paths. Additionally, the combination of FEM and DCA facilitates the calculation of low-cycle fatigue life under cyclic loading conditions.

6.2 Theoretical background

6.2.1 Nonlinear kinematic hardening

The Lemaitre-Chaboche model [126] is widely employed to capture the nonlinear mixed kinematic hardening behaviour observed in materials. This model is implemented to account for both isotropic and nonlinear kinematic components of a cyclic hardening model. These components describe the translation of the yield surface in the stress space by utilizing the back stress tensor, denoted as α. The mathematical

representation of the yield surface's function can be expressed as follows:

$$f(\sigma - \alpha) = \sigma^0, \tag{6.1}$$

where σ^0 is the radius of the yield surface and σ is the stress tensor and $f(\sigma - \alpha)$ can be expressed as:

$$f(\sigma - \alpha) = \sqrt{\frac{3}{2}(\sigma - \alpha^{\text{dev}}) : (\sigma - \alpha^{\text{dev}})} \tag{6.2}$$

α^{dev} is the deviatoric part of the stress tensor and σ is the deviatoric stress tensor. The back stress α consists of multiple back stress components, which are shown as:

$$\alpha = \sum_i [C_i \frac{1}{\sigma^0}(\sigma - \alpha)^{\epsilon^p} - \gamma_i \alpha^{\epsilon^p}] \tag{6.3}$$

where C_i and γ_i are the material properties and σ^0 is defined as:

$$\sigma^0 = \sigma_0 + Q_\infty(1 - e^{-be^p}) \tag{6.4}$$

σ_0 is the yield stress at zero plastic strain, Q_∞ is the maximum change in the size of the yield surface, and b refers to the rate at which the size of the yield surface changes as plastic strain evolves [127]. The material parameters mentioned above capture the non-uniform behaviour of isotropic hardening during cyclic loading. This non-uniformity is responsible for the Bauschinger effect, which is observed as a shift in the yield surface during cyclic loading. This shift is illustrated by the back stress tensor, which accounts for the redistribution of stresses and strains within the material. By incorporating these effects into the model, the behaviour of the material under cyclic loading can be accurately simulated and analyzed.

6.2.2 Damage initiation

The damage criterion, when applied in conjunction with cyclic loading conditions, allows for the prediction of damage initiation resulting from stress reversals [128]. In

the case of ductile materials subjected to LCF loading, the initiation of damage is determined based on the hysteresis energy per cycle. This damage initiation model can be represented by the following equation:

$$N_0 = c_1 \Delta w_0^{c_2} \tag{6.5}$$

where N_0 is the number of cycles of the damage initiation and Δw_0 is the accumulated inelastic hysteresis energy per cycle and c_1 and c_2 are material constants, which are calibrated from experimental tests. The values of c_1 and c_2 can be obtained by implementing log rules to equation 6.5.

$$Log(N_0) = Log(c_1 \Delta w_0^{c_2}) = c_2 Log(\Delta w) + Log(c_1) \tag{6.6}$$

The linear expression between accumulated inelastic hysteresis energy density and damage initiation for each cycle is given in equation 6.6. N_0 stands for the number of cycles before hysteresis stabilization and can be obtained directly from experimental data. In the experimental data, once the hysteresis loops reach a stabilized shape and do not change from cycle to cycle, this point is referred to as the stabilized point. From this point onward, the material will start experiencing a reduction in the hysteresis loops after a certain number of cycles, denoted as N_0. N_0 represents the fatigue life or the number of cycles required for the material to exhibit a noticeable decrease in the hysteresis loops. In Figure 6.1, an approximate value of N_0 is determined to be around 550 cycles, corresponding to the point of stabilized hysteresis loops. It is an important parameter in fatigue analysis as it provides information about the material's resistance to fatigue damage and the onset of fatigue failure.

Determining the fatigue damage initiation life for cyclic softening materials can be challenging. In some cases, a 20% drop in maximum load is used as the final fracture criterion. However, for the purpose of determining the fatigue initiation life N_0, a 5% drop in the maximum load during the fatigue test is typically considered [129][130].

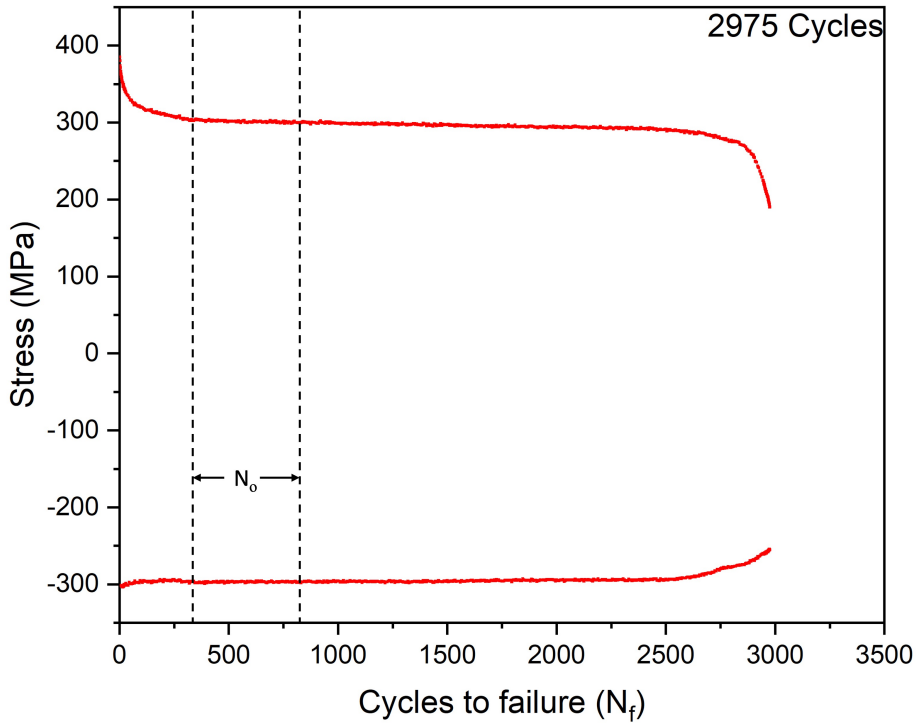

Figure 6.1: Estimation of N_o from max. and min. stress versus cycle number

The specific value chosen for N_0 does not significantly affect the final predictions for different strain ranges, as the calculation of the accumulated damage ΔW is based on the values of the stabilized cycles.

It is important to note that the value of N_0 used in the analysis impacts the rate at which damage evolves and reaches the specified failure point at 20%. A smaller value of N_0 would imply a slower development of damage over time, leading to a longer duration before reaching the specified failure criterion. However, it is crucial to consider that these observations hold true under the assumption that there are no changes in loading frequency, temperature, and material properties throughout the testing process.

6.2.3 Damage evolution

Damage evolution based on the plastic hysteresis energy density of the stabilized cycle is determined once the damage initiation criterion is satisfied. The rate of damage,

D per cycle can be defined as:

$$\frac{dD}{dN} = \frac{c_3 \Delta w^{c^4}}{L} \tag{6.7}$$

Equation 6.7 is a power law damage evolution model after fatigue damage has been initiated. D is the overall damage variable, c_3, and c_4 are material constants and L is the characteristic length associated with an integration point. To determine the material damage parameters, log rule can be applied to equation 6.7. The results can be used to compare experimental data for a given cycle number to damage increments during elemental degradation.

$$Log(\Delta N) = -c_4 Log(\Delta w) + Log(\frac{L \Delta D}{c_3}) \tag{6.8}$$

Care should be taken when modifying or converting the value of c_3 to a different system of units to ensure accuracy and consistency. When plotting the cycle number for damage evolution against the accumulated inelastic hysteresis energy per cycle (ΔN versus Δw), a linear relationship can be observed. This linear graph allows for the determination of the parameters c_3 and c_4. The characteristic length, L, associated with each integration point in the damage evolution model, is dependent on the element's geometry. By considering these factors, the final fatigue life can be predicted using the following relationship.

$$N_f = N_i + N_e = c_1 \Delta w_0^{c_2} + \frac{L}{c_3 \Delta w^{c^4}} \cdot \frac{1}{1 - c_4} \tag{6.9}$$

Equation 6.9 is used to estimate the total fatigue life when the material parameters are given by the combination of fatigue damage initiation and evolution. These four damage-related parameters can be fitted from experimental data under different stress ratios. By analyzing the experimental results, the four damage-related parameters can be accurately determined and used to predict the fatigue life of the material under different loading conditions.

6.2.4 Extended finite element formulation

The XFEM is an enhanced version of the FEM that incorporates the partition of unity (PU) method [131]. It offers several advantages, including the effective modelling of discontinuities such as cracks within the computational domain. In XFEM, the standard FEM approximation is enriched with additional functions that capture the presence of discontinuities in the displacement field. These enrichment functions are introduced through the partition of unity property, which allows for a more accurate representation of the crack geometry. One of the unique features of XFEM is its ability to model cracks independently of the underlying mesh as they are represented using an enrichment function that introduces additional degrees of freedom. These enrichment functions allow the displacement field to capture the stress singularity near the crack tip. The crack itself is not explicitly meshed, but rather its presence is captured by these enrichment functions. The enriched displacement approximation at any point can be expressed as follows [132][133]:

$$u_{xfem} = \sum_{i=1}^{n} N_i(x)[u_i + (H(x) - H(x_i))a_i + \sum_{k=1}^{4} F_k(x)b_i^k] \tag{6.10}$$

where $N_i(x)$ is the nodal shape function; u_i is the nodal displacement vector associated with the continuous part of finite element solution; $H(x)$ is the Heaviside function across the crack surface; a_k is the additional degree of freedom associated with the Heaviside function; $F_k(x)$ is the associated elastic asymptotic crack-tip function; and b_i^k is the nodal enriched degree of freedom vector. The Heaviside discontinuous function also contributes to the jump-enriched nodes:

$$H(x) = \begin{cases} +1, & \Phi(x) > 0 \\ -1, & \Phi(x) < 0 \end{cases} \tag{6.11}$$

where $\Phi(x)$ is the signed distance function calculated from the measurement point x to the crack surfaces. It takes a value of zero on the crack surface and has different signs on either side of the crack. For nodes located near the crack tip, there are four

essential asymptotic crack tip functions required to accurately represent the solution for linear elastic isotropic materials:

$$F_\alpha(x) = [\sqrt{r}sin\frac{\theta}{2}, \sqrt{r}cos\frac{\theta}{2}, \sqrt{r}sin\theta sin\frac{\theta}{2}, \sqrt{r}sin\theta cos\frac{\theta}{2}] \tag{6.12}$$

where r and θ are the local polar coordinates defined at the crack front. By incorporating the nodal displacement approximation described in Equation 6.10, the simulation of crack propagation can be achieved while preserving the benefits of the conventional finite element method.

The crack growth criteria commonly adopted in engineering are the maximum energy release rate (MERR) criterion [134], the maximum circumferential/hoop tensile stress (MTS) criterion [135], and the minimum strain energy density criterion [136]. When considering cracks in practical engineering structures subjected to complex loads, which are often of mixed-mode nature, these criteria provide guidance for determining the crack propagation orientation. Based on the stress field expression near the crack tip of a homogeneous, isotropic body in LEFM, the MTS criterion identifies the location of the maximum circumferential tensile stress as the direction of crack propagation. Therefore, the crack propagation angle can be determined accordingly:

$$\theta_c = 2tan^{-1}\left(\frac{\Delta K_I - \sqrt{\Delta K_I^2 + \Delta K_{II}^2}}{4\Delta K_{II}}\right) \tag{6.13}$$

The crack propagation angle, denoted as θ_i, represents the angle of crack deflection in each crack propagation step. It is important to note that the angle of crack deflection obtained from Equation 6.13 is based on the local coordinate system of the crack tip, rather than the global coordinate system of the structure.

When the mode II stress intensity factor, K_{II}, is equal to zero ($K_{II} = 0$), θ_i will be zero, indicating that the crack will continue to propagate along its previous direction without any deflection occurring. On the other hand, when K_{II} is greater than zero ($K_{II} > 0$), θ_i will be negative ($\theta_i < 0$), indicating a deflection in the counterclockwise

direction. Conversely, when K_{II} is less than zero ($K_{II} < 0$), θ_i will be positive ($\theta_i > 0$), signifying a deflection in the clockwise direction. Here, it is assumed that the counterclockwise direction is considered positive, while the clockwise direction is considered negative.

6.3 Finite element results and discussion

6.3.1 Geometry of FE models

In order to estimate the total fatigue life of the material, a fatigue specimen geometry model was created in ABAQUS. The 3D model had a radius of 2 mm and a gauge length of 25 mm. The direct cyclic analysis approach was employed, allowing for cycle-by-cycle iteration. The model was discretized using C3D8R elements with a mesh size of 0.5, as depicted in Figure 6.2. C3D8R elements are 3-dimensional solid elements with 8 nodes and 3 degrees of freedom per node. The C3D8R element had 6 faces and 4 integration points per face. To simulate the mechanical strain range, a displacement-controlled loading boundary was applied to the top portion of the model. This boundary condition represented the strain conditions experienced by the specimen during the fatigue test.

To estimate the fatigue crack propagation in a water wall section, a 3D model was developed. The water wall section, with a length of 100 mm and an inner diameter of 53.5 mm, was considered. In order to represent the weld defects observed in the weld membranes, a lack of fusion slit was incorporated into the geometry. The slit had a length of 4.5 mm and extended throughout the entire length of the water wall section. The model was meshed using C3D8R elements with a mesh size of 1 mm with refinement near the crack. This mesh size ensured an accurate representation of the geometry and allowed for capturing the crack propagation behaviour effectively. To simulate the in-phase thermo-mechanical loading conditions experienced by the water wall during service, the tube was subjected to an internal pressure of

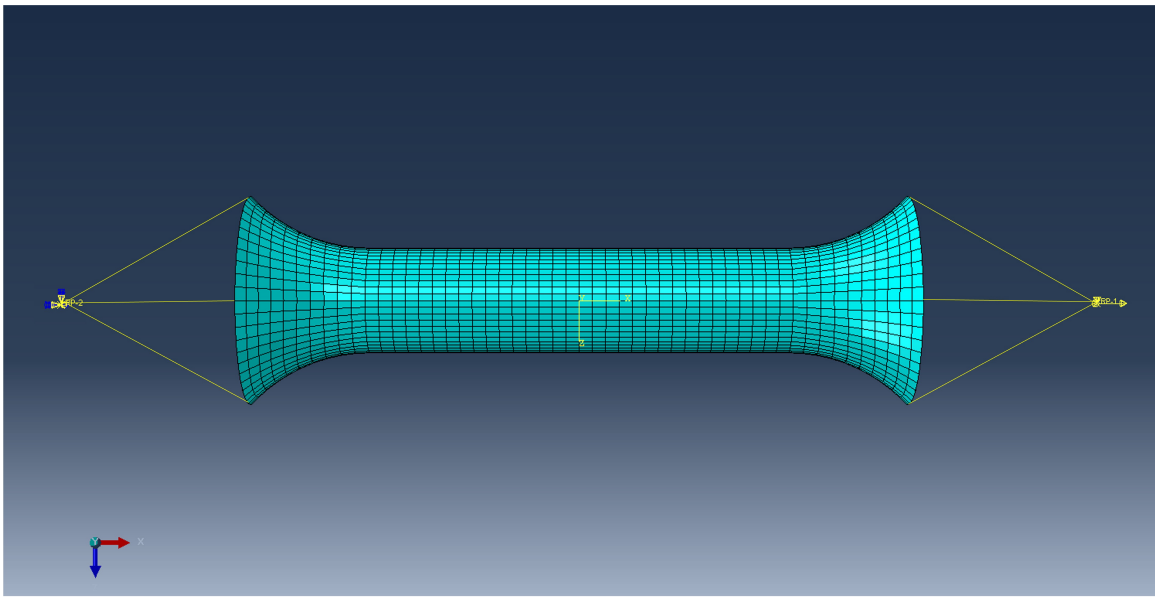

Figure 6.2: FE model for damage initiation and evolution in ABAQUS

9.5 MPa and a temperature of 300°C. The fireside of the tube was maintained at a temperature of 850°C as shown in Figure 6.3. These boundary conditions replicated the thermo-mechanical loading experienced by the water walls in practical operating conditions. To analyze the fatigue crack propagation, the direct cyclic analysis approach was employed. This approach enabled cycle-by-cycle iteration of the specified boundary conditions, allowing for a comprehensive evaluation of the crack propagation behaviour and estimation of the fatigue life of the water wall section.

6.3.2 Cyclic softening and stabilization parameters

The plasticity parameters for the welded membrane were determined through curve fitting, and their values were presented in Table 6.1. To validate the accuracy of these parameters, experimental data was compared with the calculated results of the maximum and minimum stress relaxation curves for the first 1000 cycles, as shown in Figure 6.4. The calculated results of the first 1000 cycles and the peak stress evolution curves at strain amplitudes of 0.4%, 0.6%, and 0.7% exhibited excellent agreement with the experimental results. The maximum stress gradually decreased and stabilized during the stress relaxation process, indicating a stable cyclic soften-

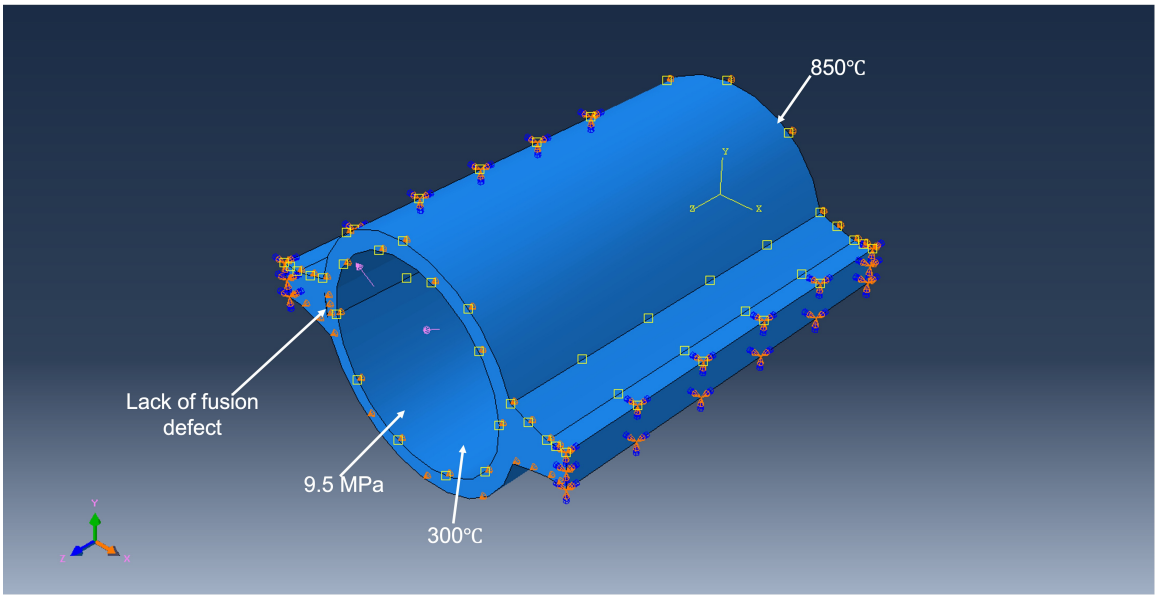

Figure 6.3: FE model for fatigue crack propagation in ABAQUS

ing behaviour. This observation confirmed the excellent predictive capability of the Chaboche plastic model for capturing the cyclic softening behaviour under uniaxial fatigue loading conditions. The comparison between experimental data and calculation results provided confidence in the accuracy of the plasticity parameters obtained through curve fitting. This further supported the suitability of the Chaboche plastic model for simulating the cyclic softening behaviour of the welded membrane under fatigue loading conditions.

Table 6.1: Chaboche nonlinear kinematic hardening model parameters of welded membranes

Materials	σ_0 **(MPa)**	Q_∞	b
Welded Membrane	371.6	-85	2.49

6.3.3 Damage initiation and evolution parameters

To predict the LCF life using the CDM approach, it was necessary to define the cyclic number for damage initiation and final failure. However, determining the exact number of cycles for damage initiation and stabilization was not straightforward and

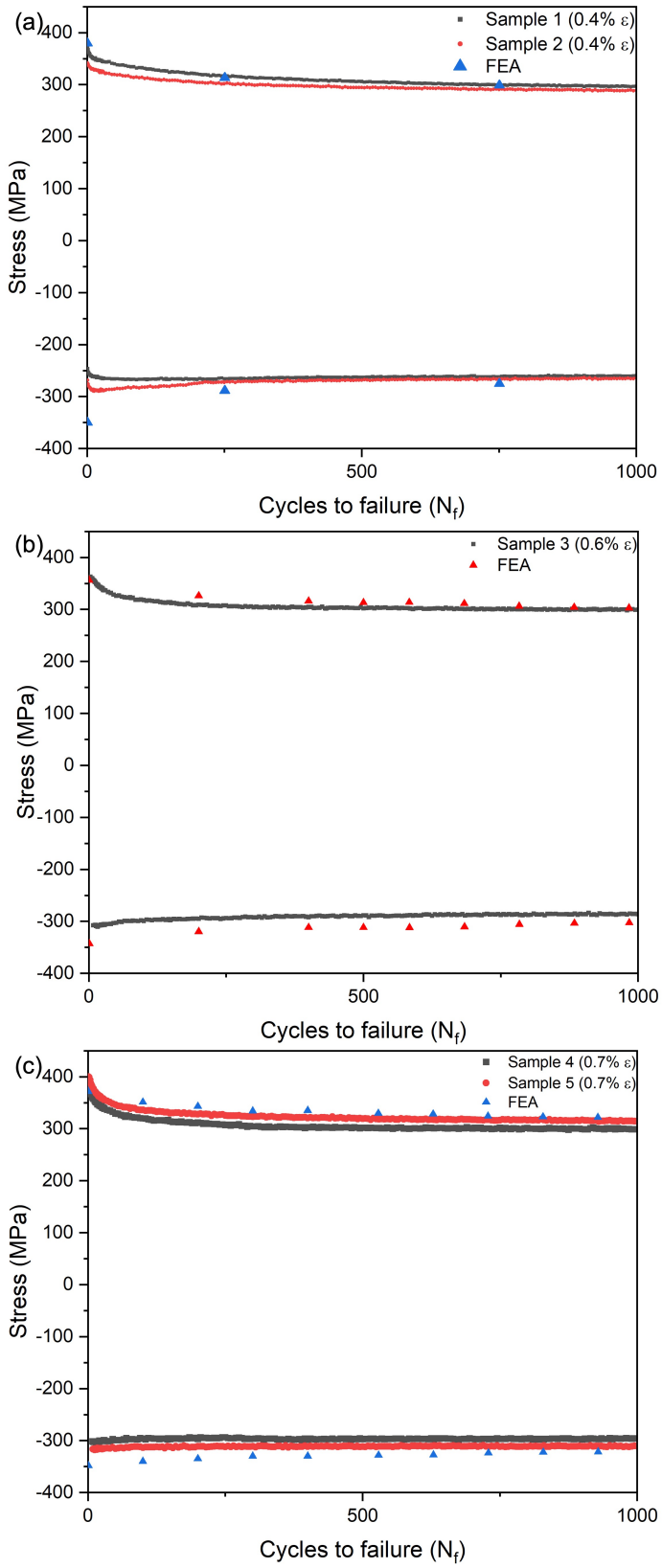

Figure 6.4: Experimental and simulation comparison of max-min stress evolution (a) max-min stress evolution under $\epsilon = 0.4\%$, (b) max-min stress evolution under $\epsilon = 0.6\%$, and (c) max-min stress evolution under $\epsilon = 0.7\%$

lacked a standardized procedure. In order to obtain the damage parameters in cyclic stress-strain curves, the strain energy density was selected as a key parameter. The stress amplitudes for each cycle exhibited different patterns depending on the material properties, resulting in diverse stabilized plateaus. Prior to reaching the stabilized cycle, the damage initiation could be estimated by analyzing the inelastic strain energy density per cycle, represented by Δw vs. N, where Δw was commonly used to characterize damage initiation and crack propagation in strain-controlled LCF studies [130]. It was important to note that different materials might exhibit distinct stress evolution responses and consequently yield varying stabilized plateaus. Therefore, the approach for estimating damage initiation based on Δw could be material-dependent. The inelastic strain density was defined by the following equation:

$$\Delta w = \int_{\epsilon_{ie1}}^{\epsilon_{ie2}} \sigma_{ij}\, d\epsilon_{ifie} \tag{6.14}$$

where ϵ_{ifie} is the inelastic strain tensor, ϵ_{ie1} is the inelastic strain tensor at the beginning of the cycle, ϵ_{ie2} is the inelastic strain tensor at the beginning of the cycle, and σ_{ij} is the stress tensor. The inelastic strain in LCF tests, neglecting other strains such as creep strain, is equivalent to the plastic strain. Therefore, the relationship between inelastic strain and plastic strain can be expressed as follows:

$$\epsilon_{ie} = \epsilon_p \tag{6.15}$$

Table 6.2 provides a summary of the values obtained for Δw_o, N_f, N_o, and $\Delta D/\Delta N$ from the LCF experimental tests. Figure 6.5 depicts the linear log-log relationships between the plastic strain energy density and fatigue life in the initial stage for the welded membrane. The linear relationships between Δw and the damage value per cycle is depicted in Figure 6.6. The figure illustrates how the damage value changes as a function of the inelastic strain energy density accumulated per cycle. The linear relationships indicate that there is a consistent and proportional increase in the

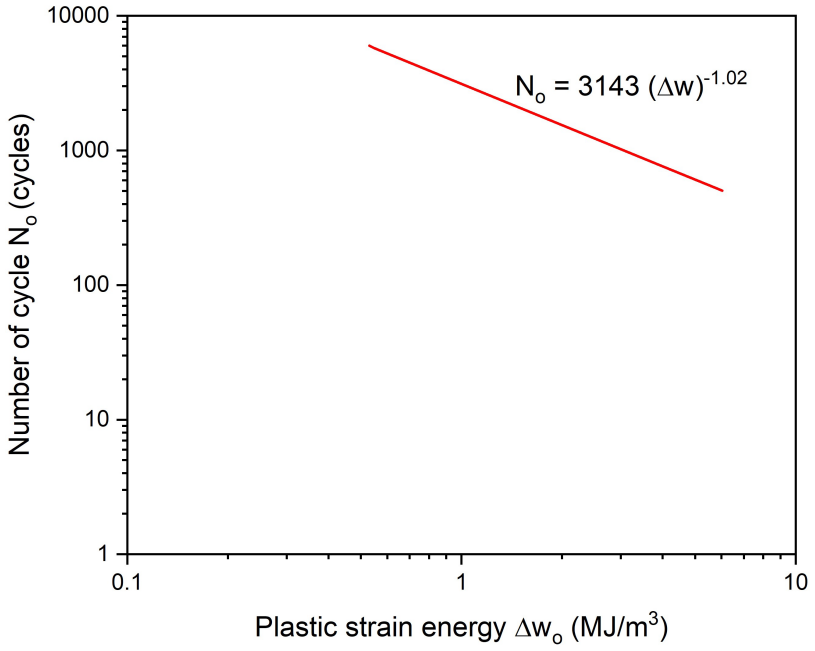

Figure 6.5: Calculation of damage initiation parameter at 300°C

damage value as the inelastic strain energy density increases. This suggests that the accumulation of inelastic strain energy plays a significant role in the progression of damage during cyclic loading.

Table 6.2: Fatigue damage value from experimental data

Specimen	$\epsilon_{max}\%$	$\Delta w_o(MJ/m^3)$	N_f	N_o	$\Delta D/\Delta N(cycle^{-1})$
Sample 1	0.4	0.53	27288	6005	4.51E-5
Sample 2	0.4	0.55	21171	5740	4.66E-5
Sample 3	0.6	4.06	3700	752	2.56E-4
Sample 4	0.7	5.5	2975	552	3.34E-4
Sample 5	0.7	6.03	2789	502	3.62E-4

The c_3 parameter, which is an important factor in the damage model, was calculated using the characteristic length L. The characteristic length L represents the adjacent distance between integration points and has been set to 0.5 mm in ABAQUS. The damage parameters obtained for LCF are summarized in Table 6.3.

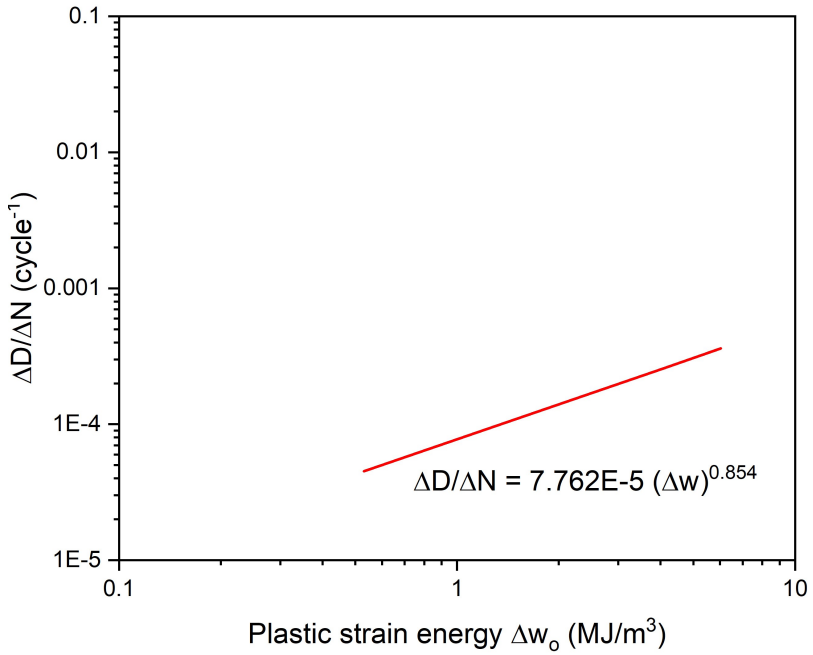

Figure 6.6: Calculation of damage evolution parameter at 300°C

Table 6.3: Fatigue damage parameters

	c_1	c_2	c_3	c_4
Welded Membrane	3143	-1.02	3.881E-5	0.854

6.3.4 Fatigue damage results

The direct cyclic analysis is performed in ABAQUS to simulate the behaviour of welded membrane specimens under various loading conditions. This analysis combines the cyclic plastic parameters obtained from the Chaboche model with the CDM parameters specific to the welded membrane material. By incorporating both the cyclic plasticity and damage evolution models, the direct cyclic FE analysis can accurately capture the material's response to cyclic loading and predict its fatigue life. The Chaboche model accounts for the cyclic plastic deformation and softening behaviour, while the CDM parameters describe the damage initiation and evolution during the loading cycles.

In Figure 6.7 (a)-(c), the predictions of the stress evolution per cycle during LCF

tests on welded membrane specimens at 300°C are compared with the corresponding experimental results for three different strain ranges: 0.4%, 0.6%, and 0.7%. The three distinct regions in the stress evolution curves can be identified. In the first region, which extends from the initial cycle up to the stabilized cycle, there is a gradual decrease in stress due to the cyclic softening behaviour of the material. The second region starts from the stabilized cycle, where the stress remains relatively constant with little change. This indicates that the material has reached a stabilized state and exhibits a stable cyclic response. This region represents a period of cyclic stability in the material's behaviour. After a certain number of loading cycles, the damage initiation stage occurs, marking the beginning of the third region. In this region, the material experiences progressive damage development, leading to a gradual decrease in stress until specimen failure. This region primarily represents the damage accumulation and degradation process in the material. It is worth noting that the FE predictions show excellent agreement with the experimental data throughout all three regions. The model successfully captures the cyclic softening behaviour, the stabilized cyclic response, and the subsequent damage initiation and development leading to failure.

In Figure 6.8, the predicted fatigue life is plotted against the corresponding experimental values for welded membrane specimens. The factor of two lines is also shown in the plot. It can be observed that all the data points representing the predicted results fall within the factor of two lines. Such an agreement suggests that the calibrated damage material parameters, obtained through the CDM approach, provide a reliable estimation of the fatigue life for the tested welded membrane specimens. It also demonstrates the potential of applying these calibrated material parameters to assess the fatigue life of more complex structures, beyond the specific welded membrane specimens tested.

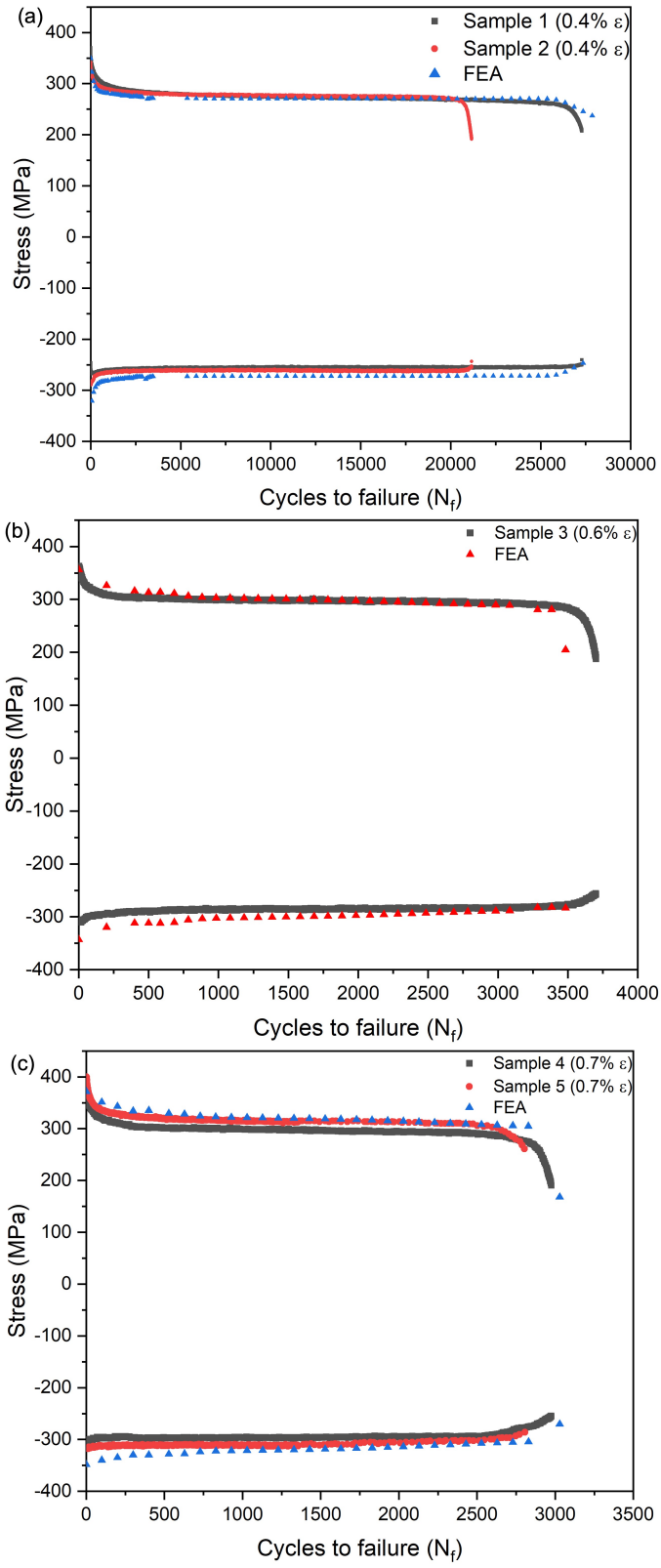

Figure 6.7: Experimental data and FE model's prediction of max. and min. stress versus cycle number for (a) $\Delta\epsilon_t = 0.4\%$, (b) $\Delta\epsilon_t = 0.6\%$, and (c) $\Delta\epsilon_t = 0.7\%$

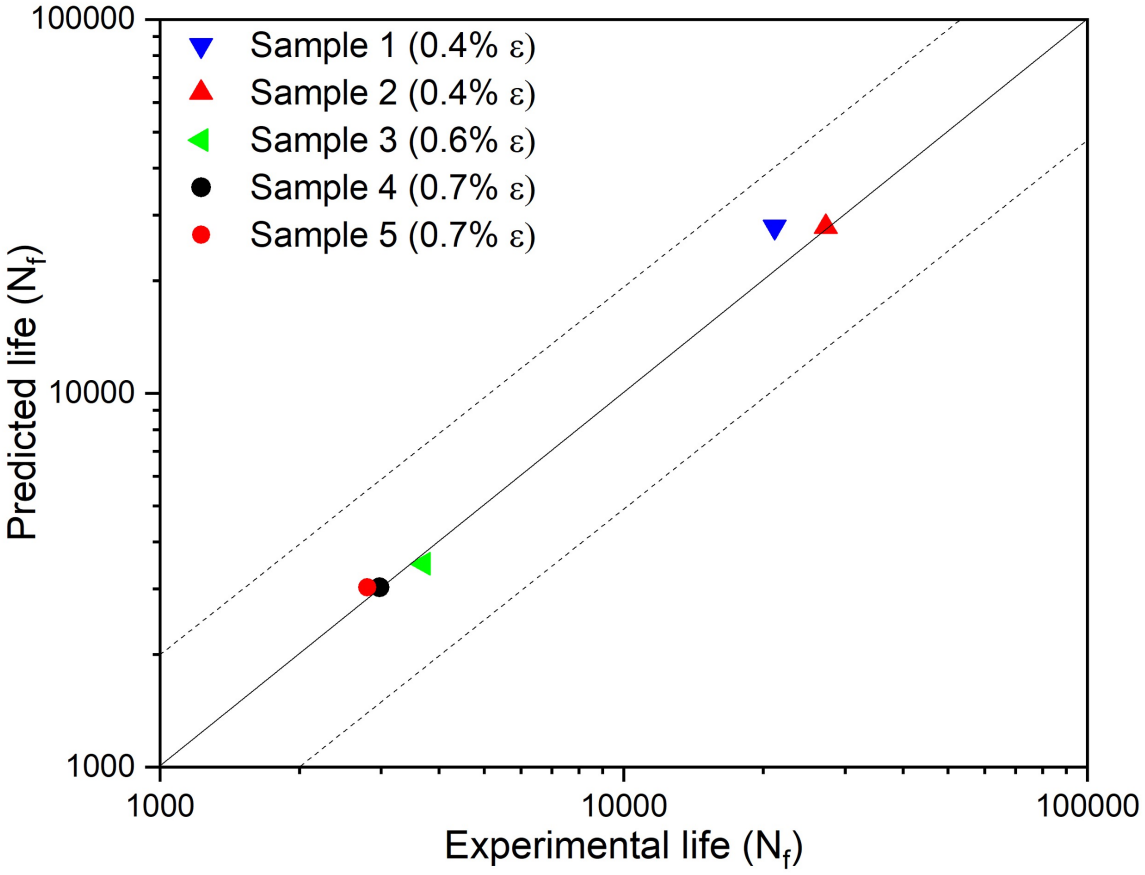

Figure 6.8: Fatigue life predictions of the welded membrane specimens

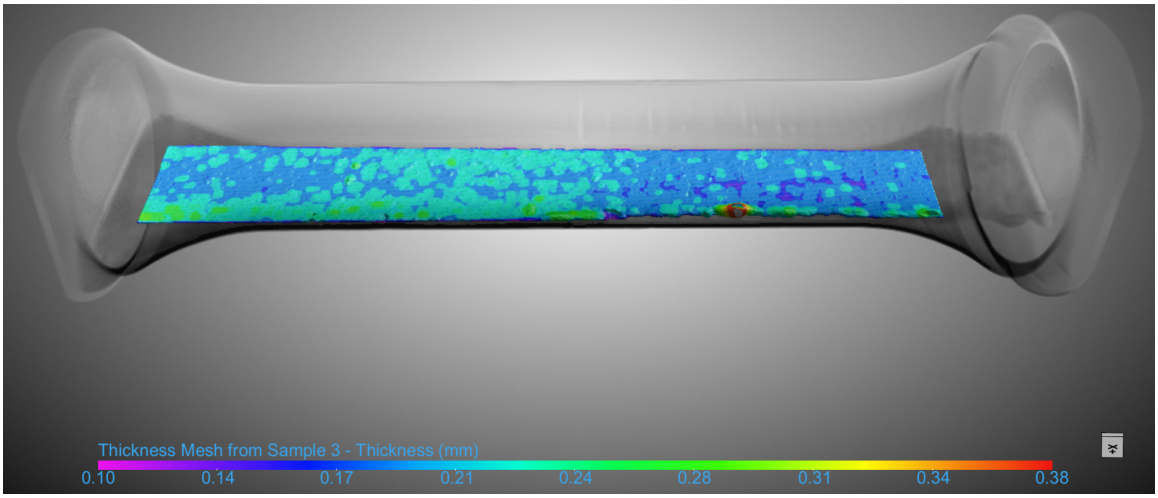

Figure 6.9: X-ray tomography results for a specimen with lack of fusion slit

6.3.5 Fatigue damage results for specimen with lack of fusion defect

The calibrated material damage parameters obtained from previous experiments are applied to predict the fatigue life and damage initiation location in a weld membrane specimen with a lack of fusion defect. The specimen is examined using X-ray tomography, which revealed the presence of a lack of fusion defect without any gas porosities as shown in Figure 6.9. A LCF test is conducted on the specimen at a temperature of 300°C, with a strain level of 0.7% and a frequency of 0.1 Hz. Fractography analysis of the specimen is performed to study the crack initiation and propagation behaviour.

The results of the fractography analysis indicated that fatigue cracks are initiated at two distinct regions in the specimen. One crack initiated from the lack of fusion slit and propagated towards the specimen surface, while the other crack initiated at the specimen surface and propagated towards the center. The presence of fatigue striations at higher magnification confirmed that the damage occurred due to cyclic fatigue loading as shown in Figure 5.13.

A 3D model of the specimen with a lack of fusion slit is created, and a displacement-controlled loading boundary condition is applied to the top portion of the model. This boundary condition is set to mimic the strain conditions experienced by the speci-

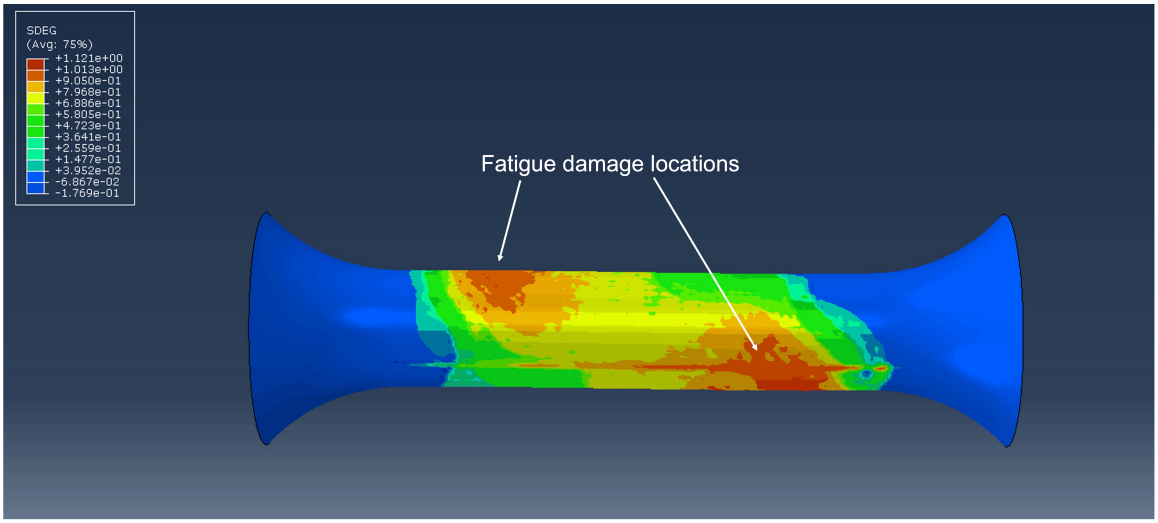

Figure 6.10: FE simulation of a welded specimen with lack of fusion slit

men during the fatigue test. The simulation results reveal that two crack initiation locations are observed within the specimen. One crack originates from the lack of fusion slit and propagates towards the specimen surface. The other crack initiates at the specimen surface and propagates towards the center of the specimen, as shown in Figure 6.10. The simulation results for the fatigue crack initiation locations are in good agreement with the experimental findings. Both the simulation and experimental data indicate that crack initiation occurs at two locations. The comparison between the predicted and experimental stress evolution per cycle for the specimen with a lack of fusion slit in Figure 6.11 supports the accuracy of the model in predicting not only the fatigue crack initiation locations but also the overall fatigue life of the welded membrane specimens. The agreement between the simulation and experimental results further strengthens the confidence in the model's predictive capabilities for assessing the structural integrity and fatigue performance of similar components with weld defects.

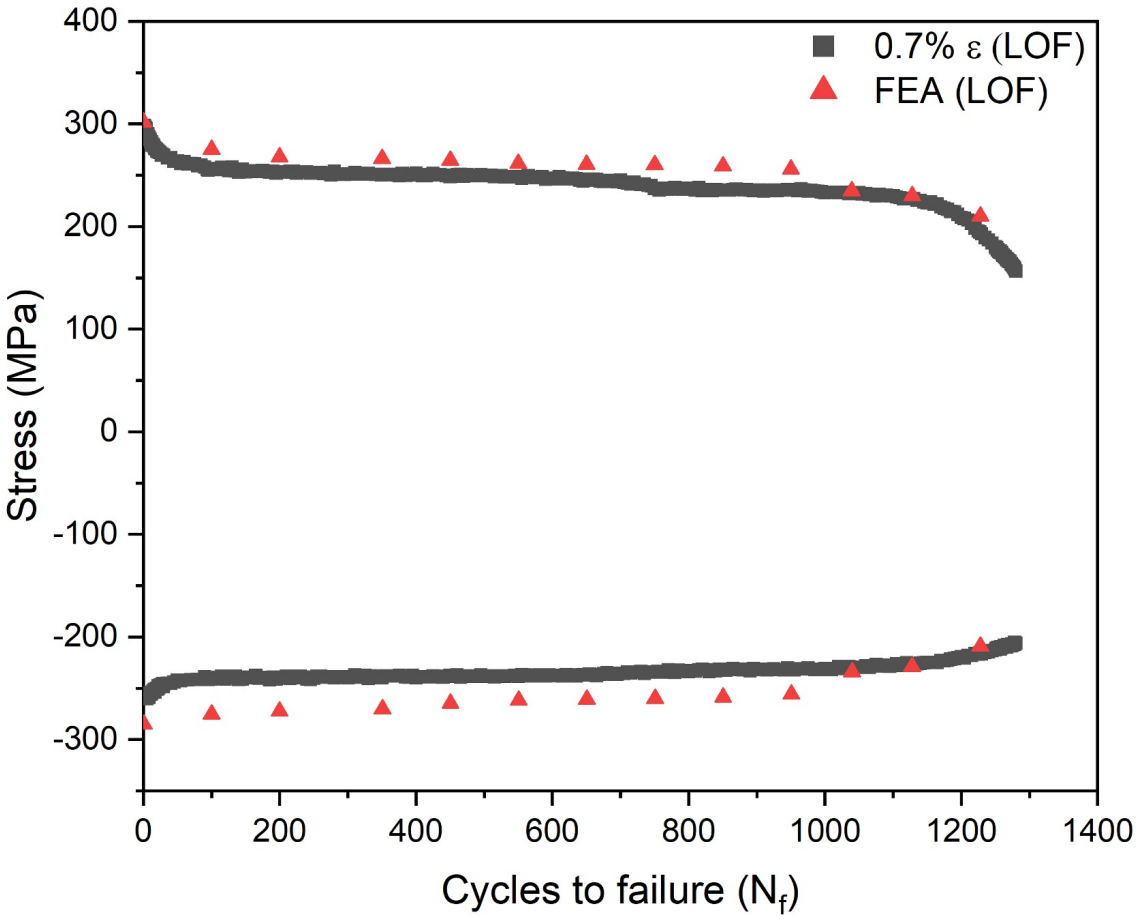

Figure 6.11: Experimental data and FE model's prediction of max. and min. stress versus cycle number for specimen with lack of fusion slit

Table 6.4: Paris constants used in water wall section

Fatigue coefficient, C (N-mm)	Fatigue exponent, m
1.67e-06	2.78

6.3.6 Fatigue crack propagation for water wall section with lack of fusion defect

The XFEM method, utilized in this study, offers a valuable approach to simulating the step-by-step crack propagation process. By incorporating additional functions into the finite element model, the XFEM method effectively captures the discontinuities and cracks present in the domain, specifically representing the fatigue crack growth in the lack of fusion defect under in-phase thermo-mechanical loading conditions. This simulation visualization of critical areas of stress distribution within the water wall section. Fracture mechanics experiments and fatigue crack growth studies are known to be resource-intensive, requiring sophisticated instruments and involving time-consuming procedures for each set of parameters. Additionally, due to geometric constraints within the water wall structure, performing such tests becomes challenging.

In the fatigue crack growth analysis, the Paris constants C and m play a significant role in estimating the crack growth rate. These constants are specific to the material being analyzed. Table 6.4 provides the values of the Paris constants C and m for the studied material. To simulate the crack propagation, two different crack configurations are considered. The first crack is located at the weld toe, while the second crack is situated at the lack of fusion defect. These crack locations are depicted in Figure 6.12, providing a visual representation of the simulated crack configurations. By employing the Paris law and considering these crack locations, the model can predict the fatigue crack growth behaviour at these specific sites.

The simulation results for fatigue crack propagation provide the crack propagation direction in the water wall section under cyclic loading conditions. When the crack is

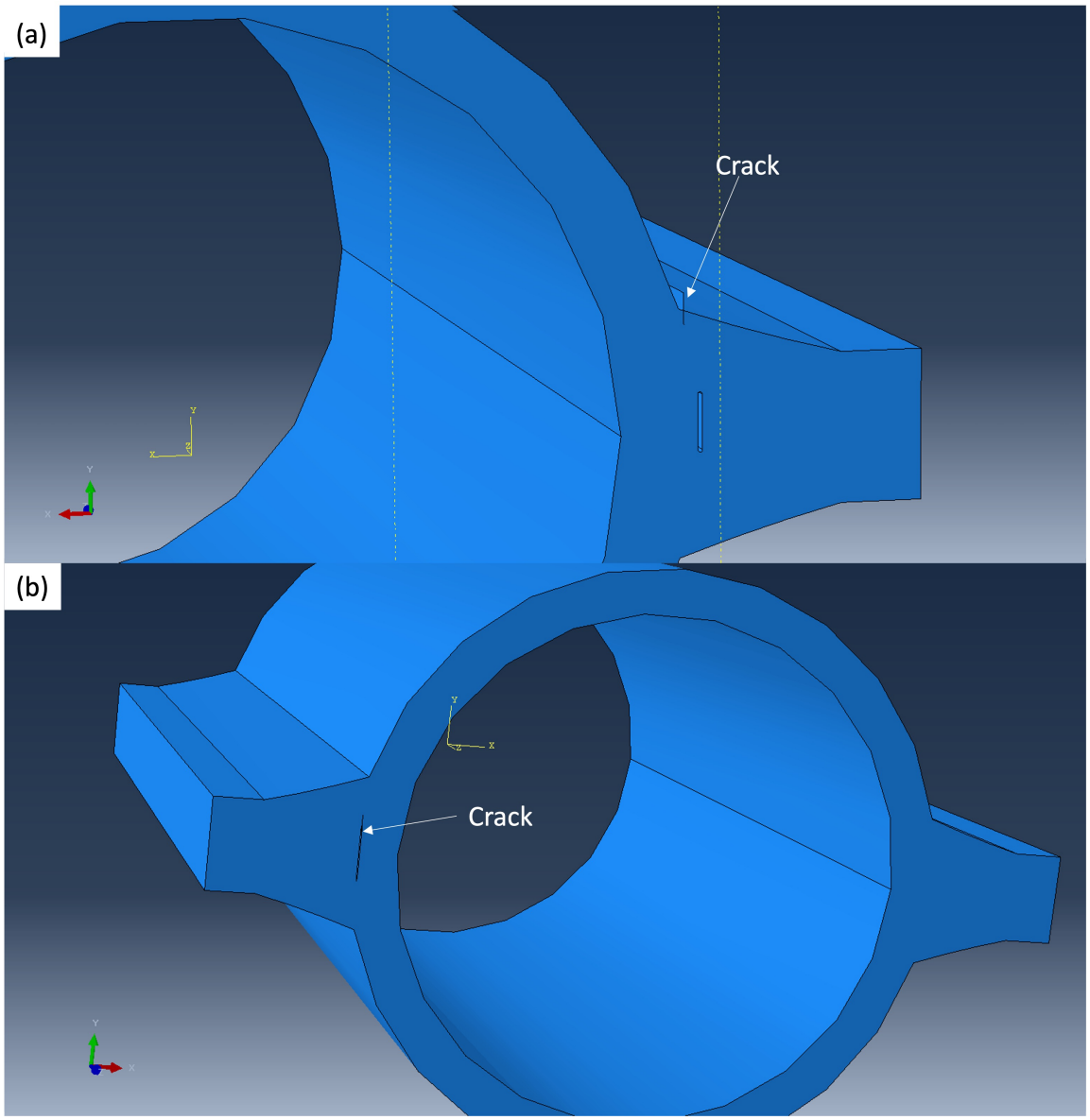

Figure 6.12: FE model with different crack locations: (a) at the weld toe region, (b) at the lack of fusion defect

located at the weld root, as depicted in Figure 6.13, the results indicate that the crack will propagate through the weld and into the tube, leading to catastrophic failure of the water wall section. This failure will result in leakage and loss of pressure. Based on the simulation, it is estimated that this failure will occur after approximately 18 years, considering 10 loading and unloading cycles per year.

On the other hand, when the crack is placed at the lack of fusion defect, as shown in Figure 6.14, the simulation results demonstrate that the crack will propagate through the weld but not into the tube. In this scenario, although the water walls will still be functional, there will be a loss of heat transfer efficiency due to only a small section of the membrane being attached to the tube. The estimated time for this type of failure to occur is approximately 13 years, considering 10 loading and unloading cycles per year.

6.3.7 Failure analysis of blowholes in water walls

The presence of a blow hole in the water wall section, as shown in Figure 6.16, has significant implications for the structural integrity and performance of the component. The crack is observed to propagate from the fireside into the airside, leaving molten slag on the airside.

In the specific case of the water wall section, the fatigue crack is initiated from a pre-existing lack of fusion defect, likely triggered by the in-phase thermo-mechanical loading during operation. This crack propagates through the weld, resulting in the detachment of a section of the membrane from the tubes, as shown in Figure 6.14. This detachment adversely affects heat transfer efficiency and creates a localized hotspot. The temperature gradient in the water wall section with the presence of lack of fusion defects and fatigue cracks is illustrated in Figure 6.17 (a). TET10 element type with a global mesh size of 1 mm is considered after performing a mesh independence study (Figure 6.15). The fatigue crack isolates a section of the membrane, leading to decreased heat transfer efficiency. Temperature measurements range from 850°C to

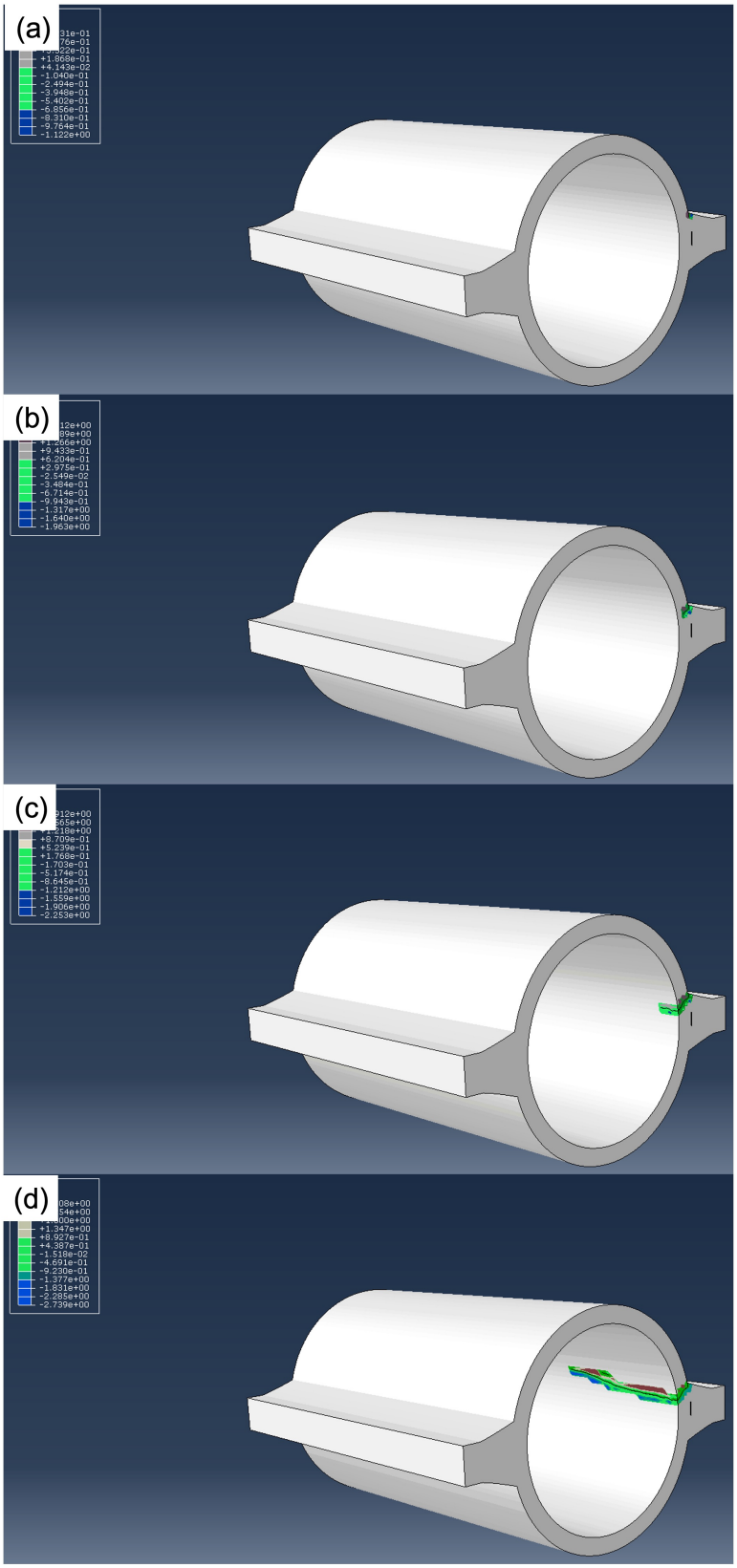

Figure 6.13: Crack propagation simulation when the crack is placed at weld root: (a) crack propagation status at t = 0 cycles, (b) crack propagation status at t = 117 cycles, (c) crack propagation status at t = 180 cycles, and (d) crack propagation status at t = 182 cycles.

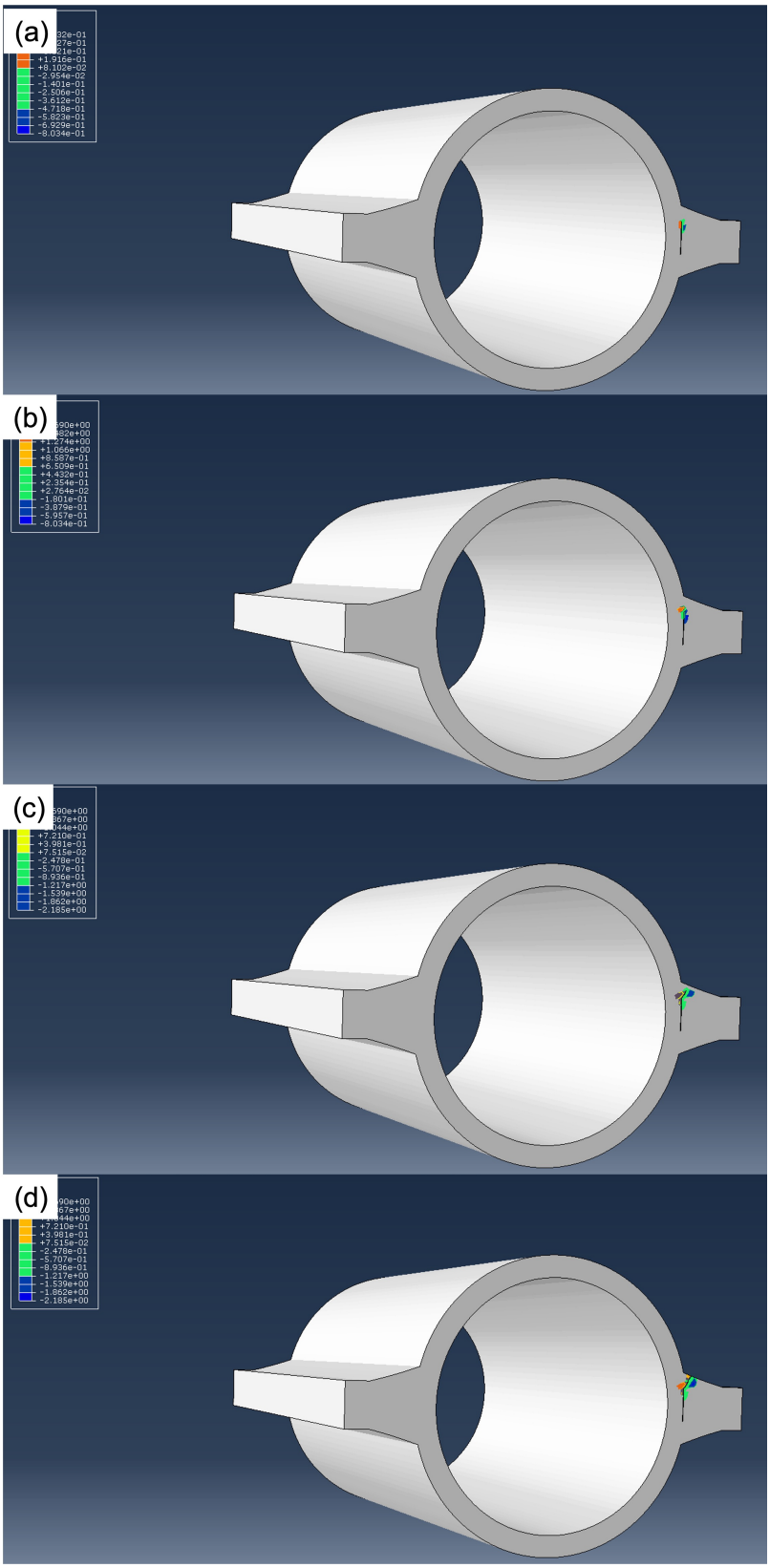

Figure 6.14: Crack propagation simulation when the crack is placed at lack of fusion slit: (a) crack propagation status at t = 0 cycles, (b) crack propagation status at t = 99 cycles, (c) crack propagation status at t = 112 cycles, and (d) crack propagation status at t = 129 cycles.

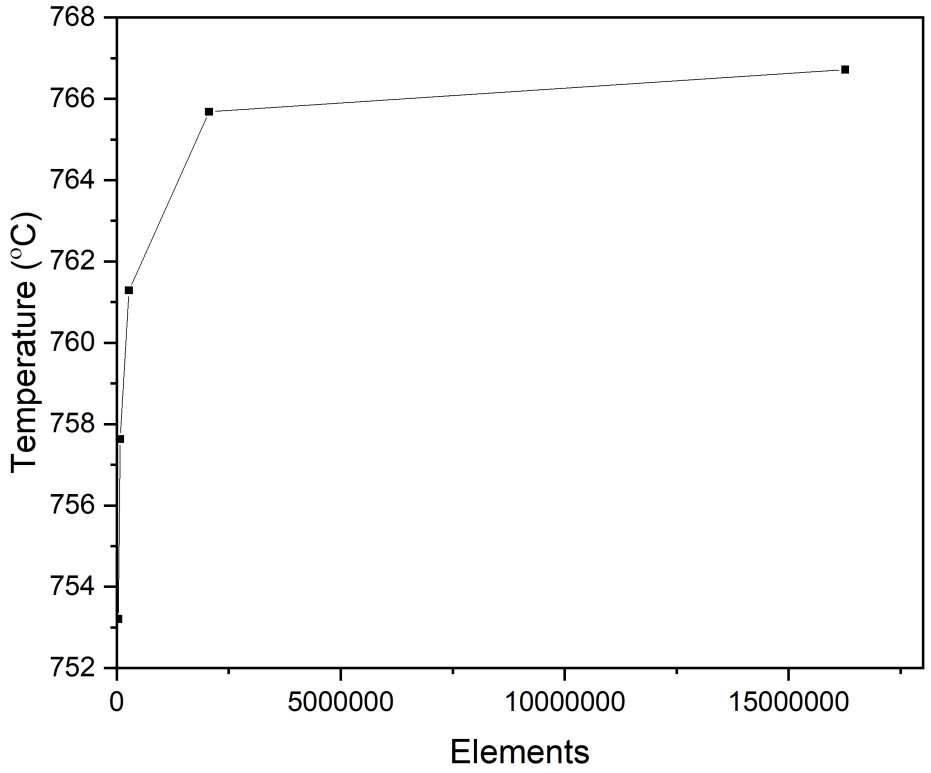

Figure 6.15: Mesh study for temperature in water wall section

750°C, with temperatures above 800°C observed in 3/4th of the membrane thickness. In contrast, Figure 6.17 (b) illustrates the temperature gradient in the water wall section without the presence of any defects. The thermal gradient in the membrane section is not as severe as observed in the defect-containing water wall section with temperatures above 800°C observed up to half of the membrane thickness.

The presence of oxide layers, acting as thermal insulators, exacerbates the temperature at the membrane. As the temperature approaches the melting point, the affected membrane section can be blown out, resulting in molten residues on the air-side. The presence of weld observed at the edges of the blowhole, as shown in Figure 6.18, provides additional evidence supporting the assumption of its formation.

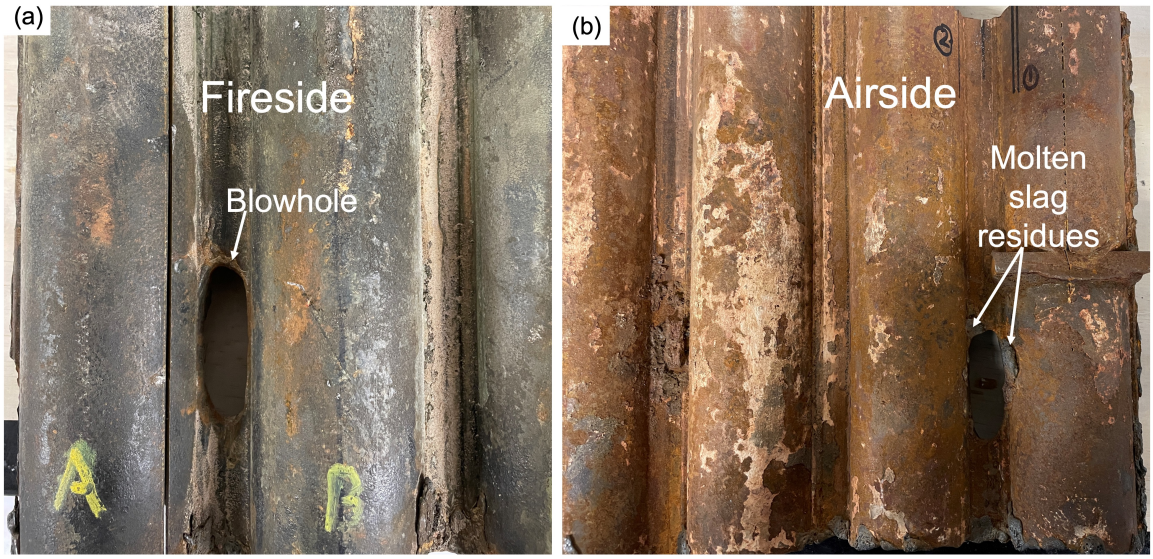

Figure 6.16: (a) Fireside of the water wall section, and (b) Airside of the water wall section

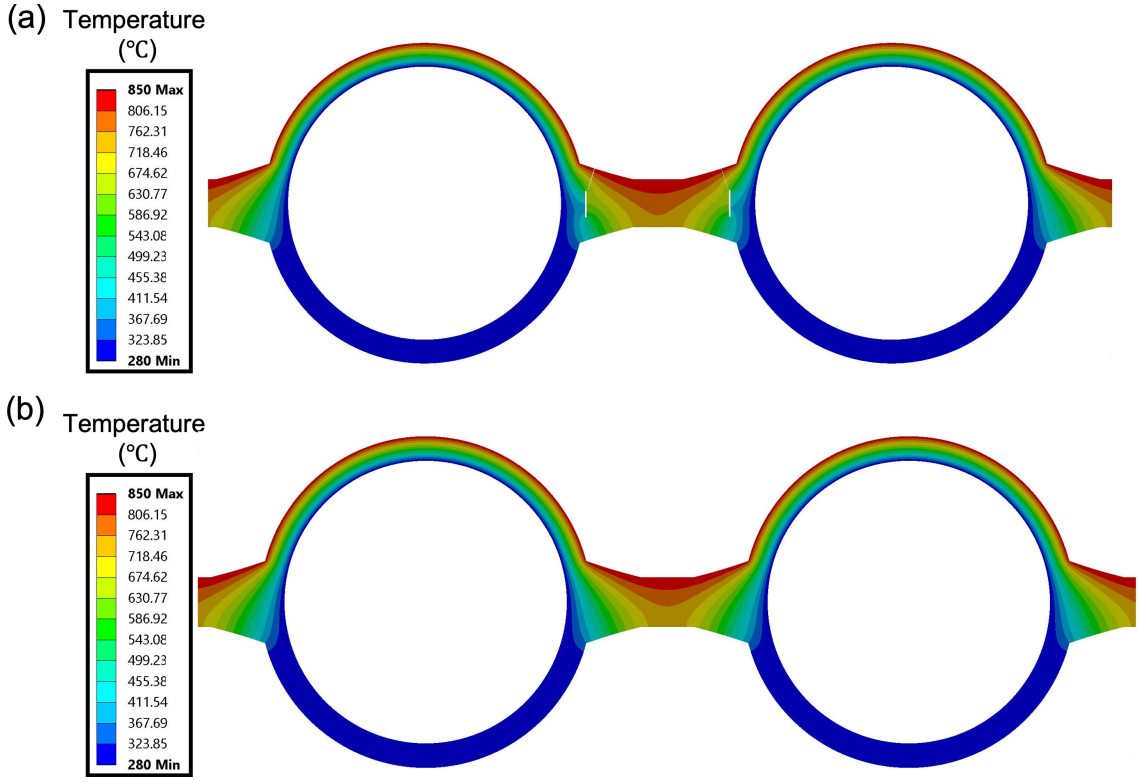

Figure 6.17: (a) FE simulation of temperature gradient in the presence of lack of fusion defects and fatigue cracks, (b) FE simulation of temperature gradient without the presence of lack of fusion defects and fatigue cracks

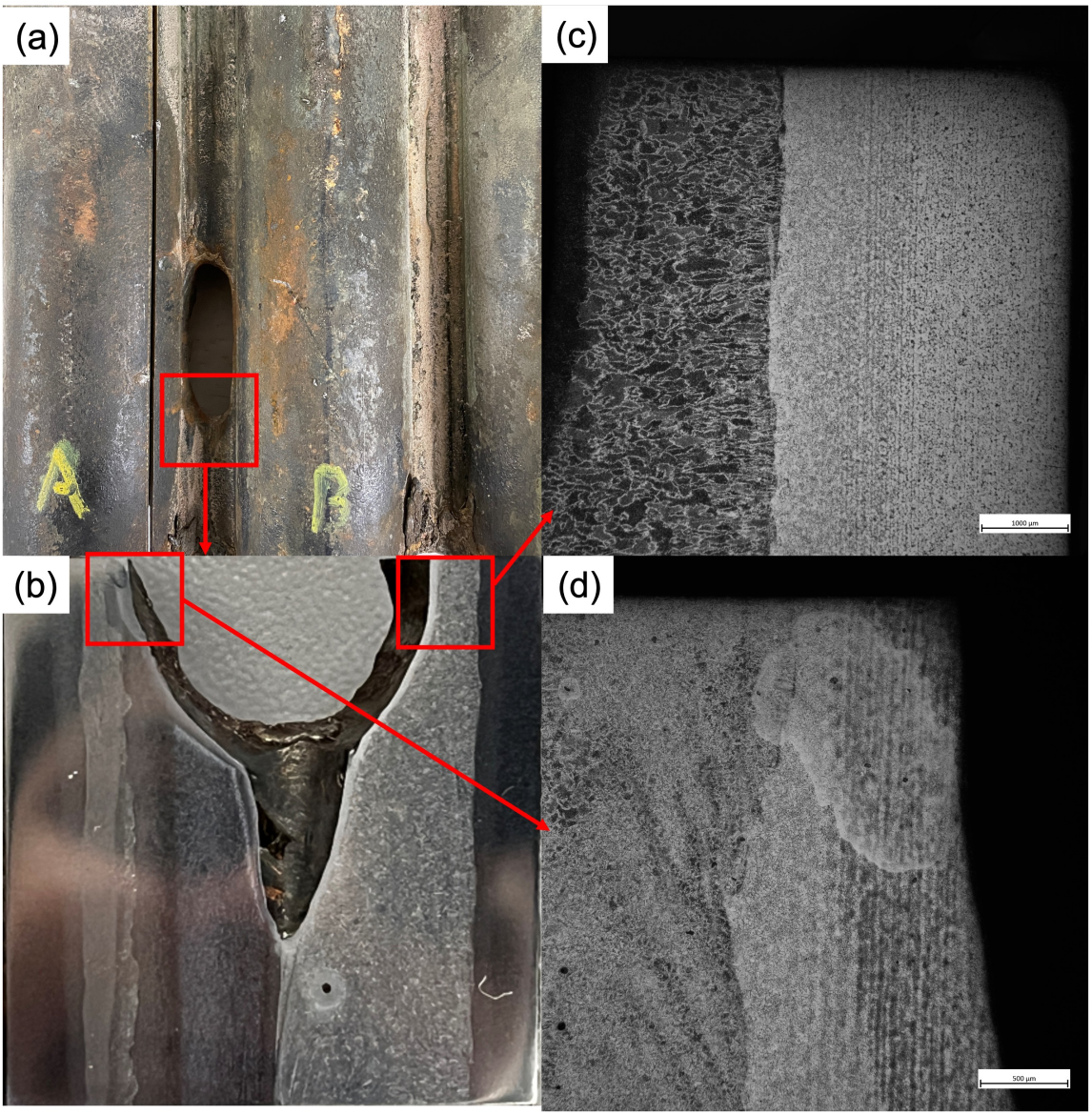

Figure 6.18: (a) Blow hole from the fireside, (b) Polished section of the blow hole, (c) macrostructure at the right edge of the blow hole, and (d) macrostructure at the left edge of the blow hole.

6.4 Summary

The fatigue damage parameters and crack propagation parameters are established for weld membrane specimens, successfully validating the cyclic softening, fatigue damage initiation, and damage evolution parameters at strain levels of 0.4%, 0.6%, and 0.7%. The experimental and simulation results exhibit excellent agreement, accurately replicating all three stages of fatigue life. The application of the fatigue damage parameters is extended to simulate fatigue damage in specimens with a lack of fusion defect, enabling precise prediction of fatigue crack initiation sites and fatigue life.

Furthermore, the establishment of Paris law parameters aims to understand the formation of blowholes in the water wall section's membrane. Cracks are introduced at two different locations: the weld toe and the lack of fusion slit. In the case of the crack at the weld toe, it is predicted that the crack will propagate through the weld into the tube, leading to pressure drop and leakage. However, when the crack is positioned at the lack of fusion defect, it is observed that the crack will propagate through the weld, disconnecting a section of the membrane from the tube.

The investigation of the blowhole reveals that the crack originates from the lack of fusion defect and propagates into the weld, causing the membrane to disconnect from the tubes. Consequently, the heat transfer efficiency of the water wall section decreases, resulting in the formation of a local thermal hotspot. As the temperature approaches the melting point, the membrane ruptures, leaving molten slag residues on the airside of the water walls.

Chapter 7

Conclusion and Future work

7.1 Conclusion

Water walls in industrial power plants and refineries are prone to premature failure due to harsh service conditions. Existing research has focused on microstructural degradation and oxide formation on water walls, but the role of pre-existing weld defects as crack initiation sites during plant operations has not been thoroughly examined. This thesis aims to enhance the understanding of thermo-mechanical fatigue failure in water walls using advanced experimental techniques and finite element modeling, establishing their applicability to in-service conditions. By comparing the fatigue damage and crack growth behaviour observed in experimental analysis, the applicability of the findings to water wall failure during in-service conditions is established. Based on the research conducted in this thesis, the following major conclusions can be drawn:

1. By employing finite element modeling and EBSD characterization, it is discovered that subjecting defect-containing water walls to hydrostatic preloading has a notable impact on their mechanical properties after being put back into service. Specifically, hydrostatic preloading at a pressure of 1.5 times the MAWP results in localized plastic deformation near the pre-existing weld defects, leading to significant strain hardening and strain aging effects. As a consequence, the mechanical properties of the welded membrane specimens are considerably

altered. Based on the test results, it is recommended to maintain the hydrostatic pressure at approximately 110% of the MAWP to minimize the occurrence of significant changes in mechanical properties caused by strain hardening and strain aging at stress concentration points within defect-containing water wall membranes.

2. A thorough three-dimensional characterization is performed on pre-existing weld defects, as observed in Chapter 3. The size and shape of the defects play a crucial role in determining the site of fatigue crack initiation and the overall fatigue life. Sharper defects have a more detrimental impact on fatigue life compared to rounder defects. The SIF are calculated using both the LEFM and the Murakami method, showing close agreement. However, the stress intensity factor calculated using Murakami's method slightly underestimates SIF since it does not consider the shape parameter and only accounts for a fixed defect area.

   The weld fusion zone, in the absence of defects, is the most susceptible location for fatigue crack initiation. This observation is attributed to the coarse dendritic microstructure present in the as-solidified weld fusion zone, which is generally less ductile than the base material. The coarse microstructure is more prone to the formation of micro-cracks, which eventually propagate and contribute to the formation of primary fatigue cracks.

3. The utilization of defect parameters established in Chapter 4 and finite element analysis proves to be effective in modeling the fatigue damage and crack propagation within the welded membranes of water walls. By conducting simulations, important parameters related to fatigue damage and crack propagation are established for the weld membrane specimens. The experimental results obtained from physical testing and the simulation results demonstrate excellent agreement with each other, validating the accuracy and reliability of the finite

element modeling approach.

The cyclic softening parameters are calibrated to replicate the cyclic softening behaviour observed with the welded membrane specimens and show agreement with experimental results. The fatigue damage parameters are extracted from experimental results to simulate damage accumulation and progression. The FE model replicates the experimental observations and provides cycles to failure predictions within a factor of 1.22 for both defect-containing and defect-free specimens.

The fatigue crack propagation parameters are calibrated to investigate the crack propagation direction from different initiation sites. The formation of blowholes at the membrane of the water walls is explained by tracking the initiation and propagation of cracks. The investigation reveals that cracks originate from lack of fusion defects and propagate into the weld, causing the disconnection of the membrane from the tubes. This disconnection results in a decrease in the heat transfer efficiency of the water wall section, leading to the formation of a localized thermal hotspot. As the temperature approaches the melting point, the membrane ruptures, leaving behind molten slag residues on the airside of the water walls.

7.2 Future work

The research conducted in this thesis represents an initial step towards comprehending the fatigue failure in water walls. It opens up avenues for further investigation in the following areas:

1. **Exploring operating parameter**: Future research can explore the effects of different water wall operating parameters, such as steam pressure, steam quality, temperature, and loading cycles, on the fatigue failure of water walls. Investigating the influence of these parameters, individually and in combination,

will provide underlying mechanisms of fatigue damage in water walls and help optimize their operation for enhanced reliability.

2. **Integrate oxide properties to fatigue model**: Integrating the properties and behaviour of oxide scales into the thermo-mechanical fatigue model can provide more realistic fatigue crack propagation predictions in water walls. The formation of oxide scales on the surface of water walls is a common occurrence due to exposure to flue gases in the combustion chamber. These oxide scales have significant effects on the material's mechanical and thermal properties. This can involve studying the interaction between the oxide scales and pre-existing defects, as well as the effect of thermal cycling on the integrity and adhesion of the oxide layer. Furthermore, considering the growth and spallation of oxide scales during thermal and mechanical loading can provide a more comprehensive understanding of the fatigue failure mechanisms in water walls.

Bibliography

[1] *Central Boiler Plants*. Department of the Army, 1989.

[2] J. Lancaster, "Failures of boilers and pressure vessels: Their causes and prevention," *International Journal of Pressure Vessels and Piping*, vol. 1, no. 2, pp. 155–170, 1973, ISSN: 0308-0161. DOI: https://doi.org/10.1016/0308-0161(73)90020-3.

[3] R. Viswanathan, S. R. Paterson, H. Grunloh, and S. Gehl, "Life Assessment of Superheater/Reheater Tubes in Fossil Boilers," *Journal of Pressure Vessel Technology*, vol. 116, no. 1, pp. 1–16, Feb. 1994, ISSN: 0094-9930. DOI: 10.1115/1.2929553.

[4] A. Pramanick, G. Das, S. Das, and M. Ghosh, "Failure investigation of super heater tubes of coal fired power plant," *Case Studies in Engineering Failure Analysis*, vol. 9, pp. 17–26, 2017, ISSN: 2213-2902. DOI: https://doi.org/10.1016/j.csefa.2017.06.001.

[5] H. Sunandrio, H. Suhartono, and Y. Prawoto, "Overheated pipe due to scale: Field failure investigation and finite element analysis," *Case Studies in Engineering Failure Analysis*, vol. 8, pp. 36–48, 2017, ISSN: 2213-2902. DOI: https://doi.org/10.1016/j.csefa.2017.04.003.

[6] B. R. Cardoso, F. W. Comeli, R. M. de Santana, H. C. Furtado, M. B. Lisboa, and L. H. de Almeida, "Microstructural degradation of boiler tubes due to the presence of internal oxide layer," *Journal of Materials Research and Technology*, vol. 1, no. 2, pp. 109–116, 2012, ISSN: 2238-7854. DOI: https://doi.org/10.1016/S2238-7854(12)70020-0.

[7] R. K. Roy, S. K. Das, A. K. Panda, and A. Mitra, "Analysis of superheater boiler tubes failed through non-linear heating," *Procedia Engineering*, vol. 86, pp. 926–932, 2014, Structural Integrity, ISSN: 1877-7058. DOI: https://doi.org/10.1016/j.proeng.2014.11.115.

[8] S. Begum, A. M. Karim, M. A. M. Nainar, and S. Sevah, "Analysis of end crack in boiler tube," in *Advances in Manufacturing and Materials Engineering (ICAMME)*, ser. Advanced Materials Research, vol. 576, Trans Tech Publications Ltd, Nov. 2012, pp. 749–752. DOI: 10.4028/www.scientific.net/AMR.576.749.

[9] J. Ahmad, J. Purbolaksono, and L. Beng, "Thermal fatigue and corrosion fatigue in heat recovery area wall side tubes," *Engineering Failure Analysis*, vol. 17, no. 1, pp. 334–343, 2010, Papers presented at the 25th meeting of the Spanish Fracture Group, ISSN: 1350-6307. DOI: https://doi.org/10.1016/j.engfailanal.2009.06.014.

[10] D. Jones, "Creep failures of overheated boiler, superheater and reformer tubes," *Engineering Failure Analysis*, vol. 11, no. 6, pp. 873–893, 2004, ISSN: 1350-6307. DOI: https://doi.org/10.1016/j.engfailanal.2004.03.001.

[11] J. J. Perdomo and T. D. Spry, "An overheat boiler tube failure," *Journal of Failure Analysis and Prevention*, vol. 5, no. 2, pp. 25–28, 2005. DOI: 10.1361/15477020522997.

[12] L. N. Moghanlou and M. Pourgol-Mohammad, "Assessment of the Pitting Corrosion Degradation Lifetime: A Case Study of Boiler Tubes," *ASCE-ASME J Risk and Uncert in Engrg Sys Part B Mech Engrg*, vol. 3, no. 4, Jun. 2017, 041002, ISSN: 2332-9017. DOI: 10.1115/1.4036064.

[13] J. Ahmad, J. Purbolaksono, and L. Beng, "Thermal fatigue and corrosion fatigue in heat recovery area wall side tubes," *Engineering Failure Analysis*, vol. 17, no. 1, pp. 334–343, 2010, ISSN: 1350-6307. DOI: https://doi.org/10.1016/j.engfailanal.2009.06.014.

[14] S. Srikanth, K. Gopalakrishna, S. Das, and B. Ravikumar, "Phosphate induced stress corrosion cracking in a waterwall tube from a coal fired boiler," *Engineering Failure Analysis*, vol. 10, no. 4, pp. 491–501, 2003, ISSN: 1350-6307. DOI: https://doi.org/10.1016/S1350-6307(03)00014-1.

[15] C. B51:19, "Boiler, pressure vessel, and pressure piping code," *CSA Group*, 2019.

[16] W. M. J.F. Kiefner, "The benefits and limitations of hydrostatic testing," *Kiefner Associates, Worthington, Ohio*, 2010.

[17] *Effects of Hydrostatic Testing on the Growth of Stress-Corrosion Cracks*, vol. Volume 1: Risk Assessment and Management; Emerging Issues and Innovative Projects; Operations and Maintenance; Corrosion and Integrity Management, International Pipeline Conference, Jun. 1998, pp. 459–472. DOI: 10.1115/IPC1998-2053. eprint: https://asmedigitalcollection.asme.org/IPC/proceedings-pdf/IPC1998/40221/459/2507263/459_1.pdf.

[18] *Effectiveness of Hydrostatic Testing for High Strength Pipe Material*, vol. 2010 8th International Pipeline Conference, Volume 1, International Pipeline Conference, Sep. 2010, pp. 647–651. DOI: 10.1115/IPC2010-31426. eprint: https://asmedigitalcollection.asme.org/IPC/proceedings-pdf/IPC2010/44205/647/2703583/647_1.pdf.

[19] Y. Kang, W. Chen, R. Kania, G. V. Boven, and R. Worthingham, "Simulation of crack growth during hydrostatic testing of pipeline steel in near-neutral ph environment," *Corrosion Science*, vol. 53, no. 3, pp. 968–975, 2011, ISSN: 0010-938X. DOI: https://doi.org/10.1016/j.corsci.2010.11.029.

[20] J. Li, M. Elboujdaini, M. Gao, and R. Revie, "Investigation of plastic zones near scc tips in a pipeline after hydrostatic testing," *Materials Science and Engineering: A*, vol. 486, no. 1, pp. 496–502, 2008, ISSN: 0921-5093. DOI: https://doi.org/10.1016/j.msea.2007.09.046.

[21] W. Zhao, M. Chen, S. Chen, and J. Qu, "Static strain aging behavior of an x100 pipeline steel," *Materials Science and Engineering: A*, vol. 550, pp. 418–422, 2012, ISSN: 0921-5093. DOI: https://doi.org/10.1016/j.msea.2012.04.095.

[22] H. sang Lee, J. sung Jung, D. soo Kim, and K. bong Yoo, "Failure analysis on welded joints of 347h austenitic boiler tubes," *Engineering Failure Analysis*, vol. 57, pp. 413–422, 2015, ISSN: 1350-6307. DOI: https://doi.org/10.1016/j.engfailanal.2015.08.024.

[23] P. Munda, S. Kumar, A. Prakash, M. M. Husain, V. Rajnikanth, and S. Ghosh Chowdhury, "Failure investigation of boiler water wall tubes of a thermal power station," *Journal of Failure Analysis and Prevention*, vol. 16, no. 1, pp. 9–18, 2016. DOI: 10.1007/s11668-015-0055-0.

[24] M. Nurbanasari and Abdurrachim, "Investigation of leakage on water wall tube in a 660 mw supercritical boiler," *Journal of Failure Analysis and Prevention*, vol. 14, no. 5, pp. 657–661, 2014. DOI: 10.1007/s11668-014-9861-z.

[25] K. Tsuzaki, Y. Matsuzaki, T. Maki, and I. Tamura, "Fatigue deformation accompanying dynamic strain aging in a pearlitic eutectoid steel," *Materials Science and Engineering: A*, vol. 142, no. 1, pp. 63–70, 1991, ISSN: 0921-5093. DOI: https://doi.org/10.1016/0921-5093(91)90754-B.

[26] R. Adi Himarosa, S. Dini Hariyanto, W. Hozaifa Hasan, and M. Akhsin Muflikhun, "Failure analysis of platen superheater tube, water wall tube, and sealpot plate: A case study from electricity power plant in indonesia," *Engineering Failure Analysis*, vol. 135, p. 106 108, 2022, ISSN: 1350-6307. DOI: https://doi.org/10.1016/j.engfailanal.2022.106108.

[27] D. Ghosh, H. Roy, A. Saha, and C. Subramanian, "Failure analysis of boiler water wall tube: A case study from thermal power plant," *Journal of Failure Analysis and Prevention*, vol. 22, no. 1, pp. 203–208, 2022. DOI: 10.1007/s11668-021-01271-y.

[28] M. Braun and X. Wang, "A review of fatigue test data on weld toe grinding and weld profiling," *International Journal of Fatigue*, vol. 145, p. 106 073, 2021, ISSN: 0142-1123. DOI: https://doi.org/10.1016/j.ijfatigue.2020.106073.

[29] B. Atzori, P. Lazzarin, G. Meneghetti, and M. Ricotta, "Fatigue design of complex welded structures," *International Journal of Fatigue*, vol. 31, no. 1, pp. 59–69, 2009, Fatigue assessment of welded connections, ISSN: 0142-1123. DOI: https://doi.org/10.1016/j.ijfatigue.2008.02.013.

[30] S. Tsutsumi *et al.*, "Effects of weld geometry and haz property on low-cycle fatigue behavior of welded joint," *International Journal of Fatigue*, vol. 156, p. 106 683, 2022, ISSN: 0142-1123. DOI: https://doi.org/10.1016/j.ijfatigue.2021.106683.

[31] M. Ottersböck, M. Leitner, M. Stoschka, and W. Maurer, "Effect of weld defects on the fatigue strength of ultra high-strength steels," *Procedia Engineering*, vol. 160, pp. 214–222, 2016, XVIII International Colloquium on Mechanical Fatigue of Metals (ICMFM XVIII), Gijón (Spain), September 5-7, 2016, ISSN: 1877-7058. DOI: https://doi.org/10.1016/j.proeng.2016.08.883.

[32] A. Deshmukh, G. Venkatachalam, H. Divekar, and M. Saraf, "Effect of weld penetration on fatigue life," *Procedia Engineering*, vol. 97, pp. 783–789, 2014, ISSN: 1877-7058. DOI: https://doi.org/10.1016/j.proeng.2014.12.277.

[33] F. Shuaeib, K. Benyounis, and M. Hashmi, "Material behavior and performance in environments of extreme pressure and temperatures," in *Reference Module in Materials Science and Materials Engineering*, Elsevier, 2017, ISBN: 978-0-12-803581-8. DOI: https://doi.org/10.1016/B978-0-12-803581-8.04170-9.

[34] A. E606/E606M-21, "Standard test method for strain-controlled fatigue testing standard test method for strain-controlled fatigue testing," *ASTM International, West Conshohocken.*, 2021.

[35] G. E. Dieter, *Mechanical Metallurgy*. McGraw-Hill Book Company.

[36] A. D. Swapan Basu, *Power Plant Instrumentation and Control Handbook: A Guide to Thermal Power Plants*, 2nd ed. 2019.

[37] L Susmel, *Multiaxial Notch Fatigue*, 1st ed. 2009.

[38] M. D. Sangid, "The physics of fatigue crack initiation," *International Journal of Fatigue*, vol. 57, pp. 58–72, 2013, Fatigue and Microstructure: A special issue on recent advances, ISSN: 0142-1123. DOI: https://doi.org/10.1016/j.ijfatigue.2012.10.009.

[39] K. Bhanu Sankara Rao and B. Raj, "Fatigue testing: Thermal and thermomechanical," in *Encyclopedia of Materials: Science and Technology*, K. J. Buschow *et al.*, Eds., Oxford: Elsevier, 2001, pp. 2999–3001, ISBN: 978-0-08-043152-9. DOI: https://doi.org/10.1016/B0-08-043152-6/00534-9. [Online]. Available: https://www.sciencedirect.com/science/article/pii/B0080431526005349.

[40] F. Shuaeib, K. Benyounis, and M. Hashmi, "Material behavior and performance in environments of extreme pressure and temperatures," in *Reference Module in Materials Science and Materials Engineering*, Elsevier, 2017, ISBN: 978-0-12-803581-8. DOI: https://doi.org/10.1016/B978-0-12-803581-8.04170-9. [Online]. Available: https://www.sciencedirect.com/science/article/pii/B9780128035818041709.

[41] A. Nagesha *et al.*, "Thermomechanical fatigue evaluation and life prediction of 316l(n) stainless steel," *International Journal of Fatigue*, vol. 31, no. 4, pp. 636–643, 2009, ISSN: 0142-1123. DOI: https://doi.org/10.1016/j.ijfatigue.2008.03.019. [Online]. Available: https://www.sciencedirect.com/science/article/pii/S0142112308000856.

[42] B. Li, Y. Zheng, Q. Li, C. Liu, and X. Chen, "Thermomechanical fatigue properties and microstructural damage of nitrogen alloyed 316ln stainless steel," *International Journal of Fatigue*, vol. 138, p. 105 704, 2020, ISSN: 0142-1123. DOI: https://doi.org/10.1016/j.ijfatigue.2020.105704. [Online]. Available: https://www.sciencedirect.com/science/article/pii/S0142112320302358.

[43] J. Sun and H. Yuan, "Life assessment of multiaxial thermomechanical fatigue of a nickel-based superalloy inconel 718," *International Journal of Fatigue*, vol. 120, pp. 228–240, 2019, ISSN: 0142-1123. DOI: https://doi.org/10.1016/j.ijfatigue.2018.11.018. [Online]. Available: https://www.sciencedirect.com/science/article/pii/S0142112318305747.

[44] C. Gao, T. Ren, and M. Liu, "Low-cycle fatigue characteristics of cr18mn18n0.6 austenitic steel under strain controlled condition at 100 °c," *International Journal of Fatigue*, vol. 118, pp. 35–43, 2019, ISSN: 0142-1123. DOI: https://doi.org/10.1016/j.ijfatigue.2018.08.038.

[45] W. A. Wood, "Formation of fatigue cracks," *The Philosophical Magazine: A Journal of Theoretical Experimental and Applied Physics*, vol. 3, no. 31, pp. 692–699, 1958. DOI: 10.1080/14786435808237004. eprint: https://doi.org/10.1080/14786435808237004.

[46] M. N. Islam, Y. Arai, and W. Araki, "Use of ultrasonic back-reflection intensity for predicting the onset of crack growth due to low-cycle fatigue in stainless steel under block loading," *Ultrasonics*, vol. 56, pp. 354–360, 2015, ISSN: 0041-624X. DOI: https://doi.org/10.1016/j.ultras.2014.09.001.

[47] R. Wang, H. Liu, D. Hu, D. Li, and J. Mao, "Evaluation of notch size effect on lcf life of ta19 specimens based on the stress gradient modified critical distance method," *Fatigue & Fracture of Engineering Materials & Structures*, vol. 41, no. 8, pp. 1794–1809, 2018. DOI: https://doi.org/10.1111/ffe.12821.

[48] Y Murakami, *Stress intensity factors*. 1987.

[49] A. Seweryn and K. Molski, "Elastic stress singularities and corresponding generalized stress intensity factors for angular corners under various boundary conditions," *Engineering Fracture Mechanics*, vol. 55, no. 4, pp. 529–556, 1996, ISSN: 0013-7944. DOI: https://doi.org/10.1016/S0013-7944(96)00035-5. [Online]. Available: https://www.sciencedirect.com/science/article/pii/S0013794496000355.

[50] T. Anderson, *Fracture Mechanics: Fundamentals and Applications*, 4th ed. CRC Press, 2017.

[51] P. Lukás, L. Kunz, B. Weiss, and R. Stickler, "Notch size effect in fatigue," *Fatigue & Fracture of Engineering Materials & Structures*, vol. 12, no. 3, pp. 175–186, 1989. DOI: https://doi.org/10.1111/j.1460-2695.1989.tb00525.x.

[52] Y. Akiniwa, N. Miyamoto, H. Tsuru, and K. Tanaka, "Notch effect on fatigue strength reduction of bearing steel in the very high cycle regime," *International Journal of Fatigue*, vol. 28, no. 11, pp. 1555–1565, 2006, ISSN: 0142-1123. DOI: https://doi.org/10.1016/j.ijfatigue.2005.04.017.

[53] K. Masuda, S. Ishihara, M. Ishiguro, and H. Shibata, *Study on Fatigue Lifetimes and Their Variation of Mg Alloy AZ61 at Various Stress Ratios*. Materials Sciences and Applications, 2018, vol. 9.

[54] K TANAKA and Y AKINIWA, "Fatigue crack propagation behaviour derived from s–n data in very high cycle regime," *Fatigue & Fracture of Engineering Materials & Structures*, vol. 25, no. 8-9, pp. 775–784, 2002. DOI: https://doi.org/10.1046/j.1460-2695.2002.00547.x.

[55] S. Beden, S. Abdullah, and A. K. Ariffin, "Review of fatigue crack propagation models for metallic components," *European Journal of Scientific Research*, vol. 28, Jan. 2009.

[56] P. Paris and F. Erdogan, "A Critical Analysis of Crack Propagation Laws," *Journal of Basic Engineering*, vol. 85, no. 4, pp. 528–533, Dec. 1963, ISSN: 0021-9223. DOI: 10.1115/1.3656900. eprint: https://asmedigitalcollection.asme.org/fluidsengineering/article-pdf/85/4/528/5763569/528_1.pdf. [Online]. Available: https://doi.org/10.1115/1.3656900.

[57] K. Walker, *The effect of stress ratio during crack propagation and fatigue for 2024-T3 and 7075-T6 aluminum*. ASTM International West Conshohocken, PA, 1970.

[58] R. Forman, "Study of fatigue crack initiation from flaws using fracture mechanics theory," *Engineering Fracture Mechanics*, vol. 4, no. 2, pp. 333–345, 1972, ISSN: 0013-7944. DOI: https://doi.org/10.1016/0013-7944(72)90048-3. [Online]. Available: https://www.sciencedirect.com/science/article/pii/0013794472900483.

[59] W. Elber, *The significance of fatigue crack closure*. ASTM International West Conshohocken, PA, USA, 1971.

[60] S. Roth, G. Hütter, and M. Kuna, "Simulation of fatigue crack growth with a cyclic cohesive zone model," *International Journal of Fracture*, vol. 188, no. 1, pp. 23–45, 2014. DOI: 10.1007/s10704-014-9942-8. [Online]. Available: https://doi.org/10.1007/s10704-014-9942-8.

[61] D. Dugdale, "Yielding of steel sheets containing slits," *Journal of the Mechanics and Physics of Solids*, vol. 8, no. 2, pp. 100–104, 1960, ISSN: 0022-5096. DOI: https://doi.org/10.1016/0022-5096(60)90013-2. [Online]. Available: https://www.sciencedirect.com/science/article/pii/0022509660900132.

[62] G. Barenblatt, "Concerning equilibrium cracks forming during brittle fracture. the stability of isolated cracks. relationships with energetic theories," *Journal of Applied Mathematics and Mechanics*, vol. 23, no. 5, pp. 1273–1282, 1959, ISSN: 0021-8928. DOI: https://doi.org/10.1016/0021-8928(59)90130-3. [Online]. Available: https://www.sciencedirect.com/science/article/pii/0021892859901303.

[63] Z. Ren and C. Ru, "Numerical investigation of speed dependent dynamic fracture toughness of line pipe steels," *Engineering Fracture Mechanics*, vol. 99, pp. 214–222, 2013, ISSN: 0013-7944. DOI: https://doi.org/10.1016/j.engfracmech.2012.12.016. [Online]. Available: https://www.sciencedirect.com/science/article/pii/S0013794413000027.

[64] R. Ghandriz, K. Hart, and J. Li, "Extended finite element method (xfem) modeling of fracture in additively manufactured polymers," *Additive Manufacturing*, vol. 31, p. 100 945, 2020, ISSN: 2214-8604. DOI: https://doi.org/10.1016/j.addma.2019.100945. [Online]. Available: https://www.sciencedirect.com/science/article/pii/S2214860419305184.

[65] A. Hillerborg, M. Modéer, and P.-E. Petersson, "Analysis of crack formation and crack growth in concrete by means of fracture mechanics and finite elements," *Cement and Concrete Research*, vol. 6, no. 6, pp. 773–781, 1976, ISSN: 0008-8846. DOI: https://doi.org/10.1016/0008-8846(76)90007-7. [Online]. Available: https://www.sciencedirect.com/science/article/pii/0008884676900077.

[66] T. Belytschko and T. Black, "Elastic crack growth in finite elements with minimal remeshing," *International Journal for Numerical Methods in Engineering*, vol. 45, no. 5, pp. 601–620, 1999.

[67] I. Singh, B. Mishra, S. Bhattacharya, and R. Patil, "The numerical simulation of fatigue crack growth using extended finite element method," *International Journal of Fatigue*, vol. 36, no. 1, pp. 109–119, 2012, ISSN: 0142-1123. DOI: https://doi.org/10.1016/j.ijfatigue.2011.08.010. [Online]. Available: https://www.sciencedirect.com/science/article/pii/S0142112311002209.

[68] Z. Wang, S. Zhou, J. Zhang, X. Wu, and L. Zhou, "Progressive failure analysis of bolted single-lap composite joint based on extended finite element method," *Materials Design*, vol. 37, pp. 582–588, 2012, ISSN: 0261-3069. DOI: https://doi.org/10.1016/j.matdes.2011.08.039. [Online]. Available: https://www.sciencedirect.com/science/article/pii/S0261306911006054.

[69] Y. Z. M. F. Zhongmin Xiao Wengang Zhang, "Fatigue investigations on steel pipeline containing 3d coplanar and non-coplanar cracks," *Computers, Materials & Continua*, vol. 62, no. 1, pp. 267–280, 2020, ISSN: 1546-2226. DOI: 10.32604/cmc.2020.06567. [Online]. Available: http://www.techscience.com/cmc/v62n1/38111.

[70] W. Song *et al.*, "Low-cycle fatigue life prediction of 10crni3mov steel and undermatched welds by damage mechanics approach," *Frontiers in Materials*, vol. 8, 2021, ISSN: 2296-8016. DOI: 10.3389/fmats.2021.641145. [Online]. Available: https://www.frontiersin.org/articles/10.3389/fmats.2021.641145.

[71] F. BIGLARI, P. LOMBARDI, S. BUDANO, C. M. DAVIES, and K. M. NIKBIN, "Predicting damage and failure under low cycle fatigue in a 9cr steel," *Fatigue & Fracture of Engineering Materials & Structures*, vol. 35, no. 12, pp. 1079–1087, 2012. DOI: https://doi.org/10.1111/j.1460-2695.2012.01695.x.

eprint: https://onlinelibrary.wiley.com/doi/pdf/10.1111/j.1460-2695.2012.01695.x. [Online]. Available: https://onlinelibrary.wiley.com/doi/abs/10.1111/j.1460-2695.2012.01695.x.

[72] Y. Zhang, M. Fan, Z. Xiao, and W. Zhang, "Fatigue analysis on offshore pipelines with embedded cracks," *Ocean Engineering*, vol. 117, pp. 45–56, 2016, ISSN: 0029-8018. DOI: https://doi.org/10.1016/j.oceaneng.2016.03.038. [Online]. Available: https://www.sciencedirect.com/science/article/pii/S0029801816300233.

[73] R. Cunningham *et al.*, "Analyzing the effects of powder and post-processing on porosity and properties of electron beam melted ti-6al-4v," *Materials Research Letters*, vol. 5, no. 7, pp. 516–525, 2017. DOI: 10.1080/21663831.2017.1340911.

[74] R. Cunningham, S. P. Narra, T. Ozturk, J. Beuth, and A. D. Rollett, "Evaluating the effect of processing parameters on porosity in electron beam melted ti-6al-4v via synchrotron x-ray microtomography," *JOM*, vol. 68, no. 3, pp. 765–771, 2016. DOI: 10.1007/s11837-015-1802-0.

[75] J. L. Huang, N. Warnken, J.-C. Gebelin, M. Strangwood, and R. C. Reed, "On the mechanism of porosity formation during welding of titanium alloys," *Acta Materialia*, vol. 60, no. 6, pp. 3215–3225, 2012, ISSN: 1359-6454. DOI: https://doi.org/10.1016/j.actamat.2012.02.035.

[76] N. Gouret, E. Ollivier, G. Dour, R. Fortunier, and B. Miguet, "Assessment of the origin of porosity in electron-beam-welded ta6v plates," *Metallurgical and Materials Transactions A*, vol. 35, no. 3, pp. 879–889, 2004. DOI: 10.1007/s11661-004-0013-z.

[77] G. Ziółkowski, E. Chlebus, P. Szymczyk, and J. Kurzac, "Application of x-ray ct method for discontinuity and porosity detection in 316l stainless steel parts produced with slm technology," *Archives of Civil and Mechanical Engineering*, vol. 14, no. 4, pp. 608–614, 2014, ISSN: 1644-9665. DOI: https://doi.org/10.1016/j.acme.2014.02.003.

[78] N. Sanaei and A. Fatemi, "Defect-based fatigue life prediction of l-pbf additive manufactured metals," *Engineering Fracture Mechanics*, vol. 244, p. 107 541, 2021, ISSN: 0013-7944. DOI: https://doi.org/10.1016/j.engfracmech.2021.107541.

[79] P. Amirafshari, N. Barltrop, M. Wright, and A. Kolios, "Weld defect frequency, size statistics and probabilistic models for ship structures," *International Journal of Fatigue*, vol. 145, p. 106 069, 2021, ISSN: 0142-1123. DOI: https://doi.org/10.1016/j.ijfatigue.2020.106069.

[80] I. Serrano-Munoz, J.-Y. Buffiere, C. Verdu, Y. Gaillard, P. Mu, and Y. Nadot, "Influence of surface and internal casting defects on the fatigue behaviour of a357-t6 cast aluminium alloy," *International Journal of Fatigue*, vol. 82, pp. 361–370, 2016, ISSN: 0142-1123. DOI: https://doi.org/10.1016/j.ijfatigue.2015.07.032.

[81] Y. Murakami, "Inclusion rating by statistics of extreme values and its application to fatigue strength prediction and quality control of materials," *J. Res. Natl. Inst. Stand. Tcchnol*, 99.

[82] S. Romano, A. Brandão, J. Gumpinger, M. Gschweitl, and S. Beretta, "Qualification of am parts: Extreme value statistics applied to tomographic measurements," *Materials Design*, vol. 131, pp. 32–48, 2017, ISSN: 0264-1275. DOI: https://doi.org/10.1016/j.matdes.2017.05.091.

[83] I. Serrano-Munoz, J.-Y. Buffiere, R. Mokso, C. Verdu, and Y. Nadot, "Location, location & size: Defects close to surfaces dominate fatigue crack initiation," *Scientific Reports*, vol. 7, no. 1, p. 45 239, 2017. DOI: 10.1038/srep45239.

[84] A. du Plessis, I. Yadroitsava, and I. Yadroitsev, "Effects of defects on mechanical properties in metal additive manufacturing: A review focusing on x-ray tomography insights," *Materials Design*, vol. 187, p. 108 385, 2020, ISSN: 0264-1275. DOI: https://doi.org/10.1016/j.matdes.2019.108385.

[85] M. Hamidi Nasab, S. Romano, D. Gastaldi, S. Beretta, and M. Vedani, "Combined effect of surface anomalies and volumetric defects on fatigue assessment of alsi7mg fabricated via laser powder bed fusion," *Additive Manufacturing*, vol. 34, p. 100 918, 2020, ISSN: 2214-8604. DOI: https://doi.org/10.1016/j.addma.2019.100918.

[86] J. Newman and I. Raju, "Stress-intensity factor equations for cracks in three-dimensional finite bodies," *ASTM Special Technical Publication*, pp. 238–265, 1983.

[87] H. Noguchi, R. Smith, J. Carruthers, and M. Gilchrist, "Stress intensity factors of embedded elliptical cracks and an assessment of the asme xi defect recharacterisation criteria," *International Journal of Pressure Vessels and Piping*, vol. 70, no. 1, pp. 69–76, 1997, ISSN: 0308-0161. DOI: https://doi.org/10.1016/S0308-0161(96)00048-8.

[88] A. Rotella, Y. Nadot, M. Piellard, R. Augustin, and M. Fleuriot, "Influence of defect morphology and position on the fatigue limit of cast al alloy: 3d characterization by x-ray microtomography of natural and artificial defects," *Materials Science and Engineering: A*, vol. 785, p. 139 347, 2020, ISSN: 0921-5093. DOI: https://doi.org/10.1016/j.msea.2020.139347. [Online]. Available: https://www.sciencedirect.com/science/article/pii/S0921509320304287.

[89] Y. Nadot, "Fatigue from defect: Influence of size, type, position, morphology and loading," *International Journal of Fatigue*, vol. 154, p. 106 531, 2022, ISSN: 0142-1123. DOI: https://doi.org/10.1016/j.ijfatigue.2021.106531.

[90] N. Sanaei, A. Fatemi, and N. Phan, "Defect characteristics and analysis of their variability in metal l-pbf additive manufacturing," *Materials Design*, vol. 182, p. 108 091, 2019, ISSN: 0264-1275. DOI: https://doi.org/10.1016/j.matdes.2019.108091. [Online]. Available: https://www.sciencedirect.com/science/article/pii/S0264127519305295.

[91] A. K. Matpadi Raghavendra, T. Armanni, S. Charles, and L. Marcin, "Role of defects in fatigue performance of in100," *Engineering Fracture Mechanics*, vol. 261, p. 108 224, 2022, ISSN: 0013-7944. DOI: https://doi.org/10.1016/j.engfracmech.2021.108224.

[92] M. R. Kabir and H. Richter, "Modeling of processing-induced pore morphology in an additively-manufactured ti-6al-4v alloy," *Materials*, vol. 10, no. 2, 2017, ISSN: 1996-1944. DOI: 10.3390/ma10020145. [Online]. Available: https://www.mdpi.com/1996-1944/10/2/145.

[93] A. E. 16a (2016), "Standard test methods for tension testing of metallic materials.," *ASTM International, West Conshohocken.*,

[94] *Ansys mechanical apdl theory reference*, ANSYS Inc., 2013.

[95] C. Kim and M.-G. Lee, "Finite element-based virtual fields method with pseudo-real deformation fields for identifying constitutive parameters," *International Journal of Solids and Structures*, vol. 233, p. 111 204, 2021, ISSN: 0020-7683. DOI: https://doi.org/10.1016/j.ijsolstr.2021.111204.

[96] G. Marom, S. Fischer, F. R. Tuler, and H. D. Wagner, "Hybrid effects in composites: Conditions for positive or negative effects versus rule-of-mixtures behaviour," *Journal of Materials Science*, vol. 13, no. 7, pp. 1419–1426, 1978. DOI: 10.1007/BF00553194.

[97] B. Feng, Y. Xin, Z. Sun, H. Yu, J. Wang, and Q. Liu, "On the rule of mixtures for bimetal composites," *Materials Science and Engineering: A*, vol. 704, pp. 173–180, 2017, ISSN: 0921-5093. DOI: https://doi.org/10.1016/j.msea.2017.08.005. [Online]. Available: https://www.sciencedirect.com/science/article/pii/S0921509317310122.

[98] K. Abdullah, P. Wild, J. Jeswiet, and A. Ghasempoor, "Tensile testing for weld deformation properties in similar gage tailor welded blanks using the rule of mixtures," *Journal of Materials Processing Technology*, vol. 112, no. 1, pp. 91–97, 2001, ISSN: 0924-0136. DOI: https://doi.org/10.1016/S0924-0136(01)00555-6. [Online]. Available: https://www.sciencedirect.com/science/article/pii/S0924013601005556.

[99] M. Kamaya, A. J. Wilkinson, and J. M. Titchmarsh, "Quantification of plastic strain of stainless steel and nickel alloy by electron backscatter diffraction," *Acta Materialia*, vol. 54, no. 2, pp. 539–548, 2006, ISSN: 1359-6454. DOI: https://doi.org/10.1016/j.actamat.2005.08.046. [Online]. Available: https://www.sciencedirect.com/science/article/pii/S1359645405005665.

[100] M. Kamaya *et al.*, "A round robin ebsd measurement for quantitative assessment of small plastic strain," *Materials Characterization*, vol. 170, p. 110 662, 2020, ISSN: 1044-5803. DOI: https://doi.org/10.1016/j.matchar.2020.110662. [Online]. Available: https://www.sciencedirect.com/science/article/pii/S1044580320321331.

[101] M. Kamaya, "Assessment of local deformation using ebsd: Quantification of accuracy of measurement and definition of local gradient," *Ultramicroscopy*, vol. 111, no. 8, pp. 1189–1199, 2011, ISSN: 0304-3991. DOI: https://doi.org/10.1016/j.ultramic.2011.02.004. [Online]. Available: https://www.sciencedirect.com/science/article/pii/S0304399111000726.

[102] M. Kamaya, "Measurement of local plastic strain distribution of stainless steel by electron backscatter diffraction," *Materials Characterization*, vol. 60, no. 2, pp. 125–132, 2009, ISSN: 1044-5803. DOI: https://doi.org/10.1016/j.matchar.2008.07.010. [Online]. Available: https://www.sciencedirect.com/science/article/pii/S104458030800212X.

[103] P. Watté, J. Van Humbeeck, E. Aernoudt, and I. Lefever, "Strain ageing in heavily drawn eutectoid steel wires," *Scripta Materialia*, vol. 34, no. 1, pp. 89–95, 1996, ISSN: 1359-6462. DOI: https://doi.org/10.1016/1359-6462(95)00479-3.

[104] S. Lou and D. O. Northwood, "Effect of temperature on the lower yield strength and static strain ageing in low-carbon steels," *Journal of Materials Science*, vol. 30, no. 6, pp. 1434–1438, 1995. DOI: 10.1007/BF00375244. [Online]. Available: https://doi.org/10.1007/BF00375244.

[105] A. H. Cottrell and B. A. Bilby, "Dislocation theory of yielding and strain ageing of iron," *Proceedings of the Physical Society. Section A*, vol. 62, no. 1, 1949.

[106] V. Ballarin, M. Soler, A. Perlade, X. Lemoine, and S. Forest, "Mechanisms and modeling of bake-hardening steels: Part i. uniaxial tension," *Metallurgical and Materials Transactions A*, vol. 40, no. 6, pp. 1367–1374, 2009. DOI: 10.1007/s11661-009-9813-5.

[107] V. Massardier, J. Merlin, E. Le Patezour, and M. Soler, "Mn-c interaction in fe-c-mn steels: Study by thermoelectric power and internal friction," *Metallurgical and Materials Transactions A*, vol. 36, no. 7, pp. 1745–1755, 2005. DOI: 10.1007/s11661-005-0039-x. [Online]. Available: https://doi.org/10.1007/s11661-005-0039-x.

[108] J. Belotteau, C. Berdin, S. Forest, A. Parrot, and C. Prioul, "Mechanical behavior and crack tip plasticity of a strain aging sensitive steel," *Materials Science and Engineering: A*, vol. 526, no. 1, pp. 156–165, 2009, ISSN: 0921-5093. DOI: https://doi.org/10.1016/j.msea.2009.07.013.

[109] A. De, S Vandeputte, and B. De Cooman, "Static strain aging behavior of ultra low carbon bake hardening steel," *Scripta Materialia*, vol. 41, no. 8, pp. 831–837, 1999, ISSN: 1359-6462. DOI: https://doi.org/10.1016/S1359-6462(99)00232-8. [Online]. Available: https://www.sciencedirect.com/science/article/pii/S1359646299002328.

[110] L. Samek, E. De Moor, J. Penning, J. G. Speer, and B. C. De Cooman, "Static strain aging of microstructural constituents in transformation-induced-plasticity steel," *Metallurgical and Materials Transactions A*, vol. 39, no. 11, pp. 2542–2554, 2008. DOI: 10.1007/s11661-008-9605-3. [Online]. Available: https://doi.org/10.1007/s11661-008-9605-3.

[111] B. Smith and A. Marder, "A metallurgical mechanism for corrosion-fatigue (circumferential) crack initiation and propagation in crmo boiler tube steels," *Materials Characterization*, vol. 33, no. 1, pp. 45–50, 1994, ISSN: 1044-5803. DOI: https://doi.org/10.1016/1044-5803(94)90057-4.

[112] Y. Murakami, *Metal Fatigue: Effects of Small Defects and Nonmetallic Inclusions*. 2019.

[113] N. Sanaei and A. Fatemi, "Defects in additive manufactured metals and their effect on fatigue performance: A state-of-the-art review," *Progress in Materials Science*, vol. 117, p. 100 724, 2021, ISSN: 0079-6425. DOI: https://doi.org/10.1016/j.pmatsci.2020.100724.

[114] N. Sanaei and A. Fatemi, "Analysis of the effect of internal defects on fatigue performance of additive manufactured metals," *Materials Science and Engineering: A*, vol. 785, p. 139 385, 2020, ISSN: 0921-5093. DOI: https://doi.org/10.1016/j.msea.2020.139385.

[115] G. Shi, H. Atkinson, C. Sellars, and C. Anderson, "Application of the generalized pareto distribution to the estimation of the size of the maximum inclusion in clean steels," *Acta Materialia*, vol. 47, no. 5, pp. 1455–1468, 1999, ISSN: 1359-6454. DOI: https://doi.org/10.1016/S1359-6454(99)00034-8.

[116] S. Ghosh and S. Resnick, "A discussion on mean excess plots," *Stochastic Processes and their Applications*, vol. 120, no. 8, pp. 1492–1517, 2010, ISSN: 0304-4149. DOI: https://doi.org/10.1016/j.spa.2010.04.002.

[117] Y. Murakami, "Analysis of stress intensity factors of modes i, ii and iii for inclined surface cracks of arbitrary shape," *Engineering Fracture Mechanics*, vol. 22, no. 1, pp. 101–114, 1985, ISSN: 0013-7944. DOI: https://doi.org/10.1016/0013-7944(85)90163-8.

[118] B. Bhattacharya and B. Ellingwood, "Continuum damage mechanics analysis of fatigue crack initiation," *International Journal of Fatigue*, vol. 20, no. 9, pp. 631–639, 1998, ISSN: 0142-1123. DOI: https://doi.org/10.1016/S0142-1123(98)00032-2.

[119] S. Dordrecht, *Continuum Damage Mechanics*, 1st ed. Springer Dordrecht, 2012.

[120] B. Gee, M. Parchei-Esfahani, and R. Gracie, "Xfem simulation of a mixed-mode fracture experiment in pmma," *Engineering Fracture Mechanics*, vol. 229, p. 106 945, 2020, ISSN: 0013-7944. DOI: https://doi.org/10.1016/j.engfracmech.2020.106945.

[121] A. Solob, A. Grbović, Ž. Božić, and S. Sedmak, "Xfem based analysis of fatigue crack growth in damaged wing-fuselage attachment lug," *Engineering Failure Analysis*, vol. 112, p. 104 516, 2020, ISSN: 1350-6307. DOI: https://doi.org/10.1016/j.engfailanal.2020.104516.

[122] G. Gibert, B. Prabel, A. Gravouil, and C. Jacquemoud, "A 3d automatic mesh refinement x-fem approach for fatigue crack propagation," *Finite Elements in Analysis and Design*, vol. 157, pp. 21–37, 2019, ISSN: 0168-874X. DOI: https://doi.org/10.1016/j.finel.2019.01.008.

[123] T. B. T. Belytschko, "Elastic crack growth in finite elements with minimal remeshing," *Internation Journal of Numerical Methods in Engineering*, vol. 45, pp. 601–620, 1999.

[124] *Abaqus documentation dassault systemes 2020*.

[125] F. Teimouri, M. Heidari-Rarani, and F. Haji Aboutalebi, "An xfem-vcct coupled approach for modeling mode i fatigue delamination in composite laminates under high cycle loading," *Engineering Fracture Mechanics*, vol. 249, p. 107 760, 2021, ISSN: 0013-7944. DOI: https://doi.org/10.1016/j.engfracmech.2021.107760.

[126] J. Chaboche, "Constitutive equations for cyclic plasticity and cyclic viscoplasticity," *International Journal of Plasticity*, vol. 5, no. 3, pp. 247–302, 1989, ISSN: 0749-6419. DOI: https://doi.org/10.1016/0749-6419(89)90015-6.

[127] L. J. C. J., *Mechanics of Solid Materials*. Cambridge University Press, 1990.

[128] J. Lemaitre, "A Continuous Damage Mechanics Model for Ductile Fracture," *Journal of Engineering Materials and Technology*, vol. 107, no. 1, pp. 83–89, Jan. 1985, ISSN: 0094-4289. DOI: 10.1115/1.3225775. eprint: https://asmedigitalcollection.asme.org/materialstechnology/article-pdf/107/1/83/5788781/83_1.pdf.

[129] W. Song *et al.*, "Low-cycle fatigue life prediction of 10crni3mov steel and undermatched welds by damage mechanics approach," *Frontiers in Materials*, vol. 8, 2021, ISSN: 2296-8016. DOI: 10.3389/fmats.2021.641145.

[130] R. Hormozi, F. Biglari, and K. Nikbin, "Taguchi sensitivity analysis of damage parameters for predicting the damage mechanism of 9cr steel under low-cycle fatigue test," *Fatigue & Fracture of Engineering Materials & Structures*, vol. 37, no. 11, pp. 1211–1222, 2014. DOI: https://doi.org/10.1111/ffe.12200.

[131] J. Melenk and I. Babuška, "The partition of unity finite element method: Basic theory and applications," *Computer Methods in Applied Mechanics and Engineering*, vol. 139, no. 1, pp. 289–314, 1996, ISSN: 0045-7825. DOI: https://doi.org/10.1016/S0045-7825(96)01087-0.

[132] S. Kumar, I. Singh, B. Mishra, and T. Rabczuk, "Modeling and simulation of kinked cracks by virtual node xfem," *Computer Methods in Applied Mechanics and Engineering*, vol. 283, pp. 1425–1466, 2015, ISSN: 0045-7825. DOI: https://doi.org/10.1016/j.cma.2014.10.019.

[133] G. Bhardwaj, S. Singh, I. Singh, B. Mishra, and T. Rabczuk, "Fatigue crack growth analysis of an interfacial crack in heterogeneous materials using homogenized xiga," *Theoretical and Applied Fracture Mechanics*, vol. 85, pp. 294–319, 2016, ISSN: 0167-8442. DOI: https://doi.org/10.1016/j.tafmec.2016.04.004.

[134] K. Palaniswamy and W. Knauss, "Propagation of a crack under general, in-plane tension," *International Journal of Fracture Mechanics*, vol. 8, no. 1, pp. 114 –117, 1972. DOI: 10.1007/BF00185207.

[135] F. Erdogan and G. C. Sih, "On the Crack Extension in Plates Under Plane Loading and Transverse Shear," *Journal of Basic Engineering*, vol. 85, no. 4, pp. 519–525, Dec. 1963, ISSN: 0021-9223. DOI: 10.1115/1.3656897.

[136] G. Sih, "Strain-energy-density factor applied to mixed mode crack problems," *International Journal of Fracture*, vol. 10, no. 3, pp. 305 –321, 1974. DOI: 10.1007/BF00035493.

Appendix A: Fatigue damage and crack propagation simulation

Below shows the detailed program for the model used in Chapter 5

```
*Heading
** Job name: Job-1 Model name: Model-1
** Generated by: Abaqus/CAE 2021
*Preprint, echo=NO, model=NO, history=NO, contact=NO
**
** PARTS
**
*Part, name="Lack of fusion slit"
*End Part
**
**
** ASSEMBLY
**
*Assembly, name=Assembly
**
*Instance, name="Lack of fusion slit", part="Lack of fusion slit"
*Node
      1,   12.5559149,   1.97000003,           0.
      2,           8.,           0.,           0.
      3,           8.,          -4.,           0.
      4,   12.5559149,  -5.96999979,           0.
      5,   12.5559149,  -3.10480404,    1.2350539
      6,   12.5559149,  -3.10480404,  -1.48909223
      7,   12.5559149,  -3.20695949,  -1.48909223
      8,   12.5559149,  -3.20695949,    1.2350539
      9,          -8.,           0.,           0.
     .
     .
     .
 241470,  -11.4580593,  -1.26649034,  -2.95347214
*Element, type=C3D10
     1,  12092,  12093,  12094,  12095,  32958,  32957,  32956,
32960,  32959,  32961
     2,  12092,  12096,  12097,  12098,  32964,  32963,  32962,
32966,  32965,  32967
     3,  12092,  12097,  12096,  12099,  32962,  32963,  32964,
32969,  32968,  32970
     4,  12092,  12100,  12101,  12098,  32973,  32972,  32971,
32966,  32974,  32975
     5,  12101,  12102,  12099,  12092,  32978,  32977,  32976,
32971,  32979,  32969
     6,  12094,  12103,  12097,  12104,  32982,  32981,  32980,
32984,  32983,  32985
     7,  12094,  12105,  12095,  12106,  32987,  32986,  32961,
32989,  32988,  32990
     8,  12094,  12104,  12107,  12103,  32984,  32992,  32991,
32982,  32983,  32993
     9,  12094,  12095,  12105,  12108,  32961,  32986,  32987,
32995,  32994,  32996
     .
```

```
     .
     .

  97590,  97678,  97679,  97780,  98472,  98475,  98754,  99033,
99277,  99805, 101389, 101873, 102293, 102423, 103165, 104046
 105599, 105818, 105822, 108492, 110604, 112211, 112214, 112728,
112731, 112990, 113773, 114541, 114574, 114664, 115021, 115023
 115839, 115997, 117376, 118106, 118609, 120090, 120093, 123035,
123625, 125987, 126405, 127363, 127373, 127909, 127995, 128546
 128547, 129765, 131110, 131917, 152626, 159060, 163078

*Surface, type=ELEMENT, name=s_Surf-2
_s_Surf-2_S3, S3
_s_Surf-2_S2, S2
_s_Surf-2_S4, S4
_s_Surf-2_S1, S1
** Constraint: Const
*Coupling, constraint name=Const, ref node=m_Set-15, surface=s_Surf-1
*Kinematic
** Constraint: Force
*Coupling, constraint name=Force, ref node=m_Set-16, surface=s_Surf-2
*Kinematic
*End Assembly
*Amplitude, name=Amp-1
             0.,              0.,              0.5.,              1.,
1.,              0.
**
** MATERIALS
**
*Material, name=Material-1
*Elastic
215000., 0.3
*Plastic, hardening=COMBINED, number backstresses=1
  371.62,         0.
 379.309, 0.00503042
 .
 .
 .
    520.,    0.14011
*Cyclic Hardening, parameters
 371.62,-85.,   2.49.
*damage initiation, criterion=hysteresis energy
        3143,-1.02
*damage evolution, type=hysteresis energy
        3.881406e-5,0.854
**
** BOUNDARY CONDITIONS
**
** Name: Cons Type: Symmetry/Antisymmetry/Encastre
*Boundary
```

```
Set-17, ENCASTRE
** ----------------------------------------------------------------
**
** STEP: Fatigue Loading
**
*Step, name="Fatigue Loading", nlgeom=NO, inc=100000
Fatigue Loading
*Direct Cyclic, continue=NO, fatigue, deltmx=10.
0.1, 1., 2e-05, 2.5, 30, 35, , 30
10, 100, 5000,
**
** BOUNDARY CONDITIONS
**
** Name: Load Type: Displacement/Rotation
*Boundary, amplitude=Amp-1
Set-18, 1, 1, -0.175
Set-18, 2, 2
Set-18, 3, 3
**
** OUTPUT REQUESTS
**
*Restart, write, frequency=0
**
** FIELD OUTPUT: F-Output-1
**
*Output, field
*Node Output
CF, RF, U
*Element Output, directions=YES
CYCLEINI, CYCLEINIXFEM, LE, S, SDEG
**
** HISTORY OUTPUT: H-Output-1
**
*Output, history, variable=PRESELECT
*End Step
```

```
*Heading
** Job name: Job-1 Model name: Model-1
** Generated by: Abaqus/CAE 2021
*Preprint, echo=NO, model=NO, history=NO, contact=NO
**
** PARTS
**
*Part, name=Boiler
*End Part
**
*Part, name=Crack
*End Part
**
**
** ASSEMBLY
**
*Assembly, name=Assembly
**
*Instance, name=Boiler-1, part=Boiler
*Node
      1,   -30.763298,   2.88968492,           0.
      .
      .
      .
*Element, type=C3D8R
    1,   375,   393,   399,   387,  1180,  1198,  1204,  1192
    2,   749,   382,   724,   404,  1554,  1187,  1529,  1209
    3,     5,     4,   404,   724,   810,   809,  1209,  1529
    4,     7,     8,   371,   367,   812,   813,  1176,  1172
    5,     7,   367,   376,   373,   812,  1172,  1181,  1178
    6,     7,   373,   380,   372,   812,  1178,  1185,  1177
    7,   383,   377,   366,   372,  1188,  1182,  1171,  1177
    8,   396,   421,   431,   596,  1201,  1226,  1236,  1401
    9,     1,     3,   385,   368,   806,   808,  1190,  1173
   10,   388,   385,   595,   395,  1193,  1190,  1400,  1200
   11,   389,   383,   372,   380,  1194,  1188,  1177,  1185
.
.
.
*Nset, nset=Set-1, generate
     1,  54740,      1
*Elset, elset=Set-1, generate
     1,  44421,      1
** Section: Section-1
*Solid Section, elset=Set-1, material=SA-192
,
*End Instance
**
*Instance, name=Crack-1, part=Crack
  -30.763299,     1.889685,         17.5
```

```
  -30.763299,     1.889685,         17.5, -30.1859487308104,
2.46703526918963, 18.0773502691896,         120.
*End Instance
**
*Nset, nset=Set-6, instance=Boiler-1
    11,    12,    13,    14,    15,    16,    17,    18,    19,    20,
21,    22,    23,    24,    25,    26
    27,    28,    29,    30,    31,    32,    33,    34,    35,    36,
37,    38,    39,    40,    41,    42

*Enrichment, name=Crack-1, type=PROPAGATION CRACK, elset=_PickedSet72,
interaction=IntProp-1
*End Assembly
*Amplitude, name=Amp-1
             0.,              0.,              0.5.,              1.,
1.,              0.
**
** MATERIALS
**
*Material, name=SA-192
*Conductivity
 44.01,
*Density
 7.75e-06,
*Elastic
215000., 0.33
*Expansion
 1.17394e-05,   26.85
 1.17604e-05,   28.85
 1.18621e-05,   38.85
 1.19598e-05,   48.85
 1.20552e-05,   58.85
 1.20926e-05, 61.0043
 1.21685e-05,   68.85
 1.21693e-05, 71.5467
 1.21805e-05,   72.85
 1.21976e-05,   74.85
 1.22147e-05,   76.85
 1.22988e-05,   86.85
 1.23817e-05,   96.85
 1.24639e-05,  106.85
 1.25456e-05,  116.85
 1.26272e-05,  126.85
 1.27087e-05,  136.85
 1.33269e-05, 139.101
 1.34439e-05,  146.85
 1.36011e-05,  156.85
 1.37655e-05,  166.85
 1.39374e-05,  176.85
  1.4117e-05,  186.85
```

```
1.43043e-05,  196.85
1.44991e-05,  206.85
1.47013e-05,  216.85
1.49102e-05,  226.85
1.51253e-05,  236.85
1.53457e-05,  246.85
1.55703e-05,  256.85
1.57978e-05,  266.85
1.60265e-05,  276.85
1.62544e-05,  286.85
1.64789e-05,  296.85
1.66969e-05,  306.85
1.69046e-05,  316.85
1.69333e-05,  320.92
1.70597e-05,  326.85
1.71301e-05,  330.24
1.57541e-05,  336.85
1.63296e-05,  346.85
1.67161e-05,  356.85
1.70128e-05,  366.85
1.72599e-05,  376.85
1.74756e-05,  386.85
1.76492e-05, 395.773
1.80048e-05,  406.85
1.81531e-05,  416.85
1.82934e-05,  426.85
1.84251e-05,  436.85
1.85474e-05,  446.85
1.86597e-05,  456.85
1.87611e-05,  466.85
1.88509e-05,  476.85
1.56153e-05,  486.85
 1.5578e-05,  496.85
1.56334e-05,  506.85
1.56884e-05,  516.85
1.57427e-05,  526.85
1.57964e-05,  536.85
1.58494e-05,  546.85
1.59016e-05,  556.85
 1.5953e-05,  566.85
1.60035e-05,  576.85
1.60531e-05,  586.85
1.61016e-05,  596.85
 1.6149e-05,  606.85
1.61952e-05,  616.85
  1.624e-05,  626.85
1.62834e-05,  636.85
1.63253e-05,  646.85
1.63655e-05,  656.85
 1.6404e-05,  666.85
```

```
 1.64407e-05,  676.85
 1.64753e-05,  686.85
 1.65078e-05,  696.85
 1.65381e-05,  706.85
*Specific Heat
 0.45,
**
** INTERACTION PROPERTIES
**
*Surface Interaction, name=IntProp-1
1.,
*fracture criterion, type=fatigue, mixed mode behavior=BK
0.5,-1,1.67e-06,2.78,0.01,0.9,12,12
12,2
*Initial Conditions, type=ENRICHMENT
Boiler-1.359, 1,Crack-1, -0.184784, -0.267259
Boiler-1.359, 2,Crack-1, 0.427419, -0.154784
Boiler-1.359, 3,Crack-1, 0.338926, 0.429842
Boiler-1.359, 4,Crack-1, -0.420091, 0.558873
.
.
.
**
** BOUNDARY CONDITIONS
**
** Name: BC-1 Type: Symmetry/Antisymmetry/Encastre
*Boundary
Set-8, ENCASTRE
** Name: BC-2 Type: Symmetry/Antisymmetry/Encastre
*Boundary
Set-9, ENCASTRE
** Name: BC-3 Type: Displacement/Rotation
*Boundary
Set-10, 3, 3
** Name: BC-4 Type: Displacement/Rotation
*Boundary
Set-11, 3, 3
** ----------------------------------------------------------------
**
** STEP: Step-1
**
*Step, name=Step-1, nlgeom=NO, inc=1000
*Direct Cyclic, continue=NO, fatigue, deltmx=20.
2., 1., 1e-05, 2., , , , 30
, 1000, 10000,
**
** LOADS
**
** Name: Load-1   Type: Pressure
*Dsload, amplitude=Amp-1
```

```
Surf-1, P, 9.8.
**
** PREDEFINED FIELDS
**
** Name: Predefined Field-1   Type: Temperature
*Temperature, amplitude=Amp-1
Set-6, 300.
** Name: Predefined Field-2   Type: Temperature
*Temperature, amplitude=Amp-1
Set-7, 700.
**
** OUTPUT REQUESTS
**
*Restart, write, frequency=0
**
** FIELD OUTPUT: F-Output-1
**
*Output, field
*Node Output
CF, PHILSM, PSILSM, RF, U
*Element Output, directions=YES
CYCLEINIXFEM, LE, S, SDEG, STATUSXFEM, enrrtxfem
**
** HISTORY OUTPUT: H-Output-1
**
*Output, history, variable=PRESELECT
*End Step
```